ISAS - INTERNATIONAL SCHOOL FOR ADVANCED STUDIES

Formation Scenarios for Polar Ring Galaxies

Enrichetta Iodice
International School for Advanced Studies (SISSA-ISAS)
Via Beirut 2-4, 34014 Trieste, Italy

Supervisors:
Dr. M. Arnaboldi,
Prof. L.S. Sparke,
Prof. P. Salucci

Thesis submitted for the degree of "Doctor Philosophiæ"

October 2001

SISSA - SCUOLA
ITERNAZIONALE
SUPERIORE
STUDI AVANZATI
TRIESTE
Via Beirut 2-4

TRIESTE

Contents

Introduction

Gravitational interactions and mergers affect the morphologies and dynamics of galaxies. Both the Hubble Space Telescope (HST) and the Very Large Telescope (VLT) make it possible to observe the early universe and to show that these processes become even more common as redshift increases (Rothberg & Joseph 2001, ESO Press Realease 13/01, Driver et al. 1995). From this kind of studies, there are growing evidence that mergers play a major role in the formation of early-type galaxies (Ellipticals and S0s), both in the field and in clusters (Lutz 1991, Schweizer 1999; Hibbard & Yun 1999). These observational results support the scenario, firstly proposed by Toomre & Toomre in 1972, in which the merging of two disk galaxies produces an elliptical galaxy. Furthermore, detailed numerical simulations have shown that mergers between two spiral galaxies of comparable mass lead to form spheroidal merger remnants with physical characteristics, such as density profiles, mean velocity dispersion and surface brightness, that are quite comparable to those of observed ellipticals (Barnes & Hernquist 1992). If merger occurs between two unequal-mass spiral galaxies, named as "minor mergers", it does not completely destroy their disks. Numerical simulations for this kind of mergers are able to produce an early-type object with a morphology, structure and kinematics quite similar to those observed in S0 galaxies (Bekki 1998a). The disk-disk mergers is also able to form peculiar morphologies, such as disky/boxy shape, fine structures (loops, shells, X-structures) and counterrotating cores like those observed in the present day early-type galaxies (Bekki & Shioya 1997a, 1997b; Mihos et al. 1995; Barnes & Hernquist 1996).

If two gas-rich disk galaxies with unequal mass merge with each other under an high perpendicular relative inclination and with relative collisional velocity smaller than the escape velocity of the system, the merger remnant becomes a **Polar Ring Galaxy (PRG)** (Bekki 1998). This peculiar object is composed by a central spheroidal component, the *host galaxy*, surrounded by an outer *ring*, made up by gas, stars and dust, which orbits in a nearly perpendicular plane to the equatorial one of the central galaxy (Whitmore et

al. 1990). In the dissipative disk merging scenario for the formation of early-type galaxies, PRGs may be considered as an estreme samples of minor merger remnants: in fact, they form under very particular initial physical conditions related to the orbit configuration of galaxy merging and mass ratio of the two progenitors. However, the origin of PRGs is still an open field of study: the scenario proposed by Bekki (1998) is substantially different from the standard picture for the formation of PRGs, which, on the other hand, suggests that a prexisting early-type galaxy either accreted gas by a gas-rich dwarf galaxy or by stripping it from a nearby gas-rich object during a high speed encounter (e.g. Steiman-Cameron & Durisen 1982; Sparke 1986; Quin 1991; Rix & Katz 1991; Reshetnikov & Sotnikova 1997).

Constraints on the best scenario decribing the polar ring formation can be derived from a detailed study of the observational properties of PRGs, such as their morphologies, kinematics, HI and dust content, integrated colors.

According to ring morphology, PRGs are basically divided into two broad classes (Whitmore et al. 1991): (1)*narrow polar rings*, where ring is not extended in radius, and (2) *wide polar rings* which show a disk-like polar structure. Inside the class of PRGs are also observed peculiar ring morphologies, such as *helical rings* (e.g., the Helix galaxy, NGC 2685) and *double rings* (e.g. ESO 474-G26). Roughly two-thirds of PRGs show a warped ring whose shape looks like an "integral sign", with the two sides warped in opposite directions, or a "banana" where both sides bending in the same direction (Whitmore et al. 1991). In almost all PRGs the morphology of the host galaxy resembles that of an early-type object (Elliptical or S0 galaxy): kinematical studies on some PRGs has confirmed that this component is rapidly rotating (Schechter et al. 1984b; Whitmore et al. 1990). PRGs are characterized by a large amount of HI gas, which is in some cases comparable with the total mass of the host galaxy, and it is closely associated with the stellar component in the polar ring (Schechter et al. 1984a; Richter, Sackett & Sparke 1994; Arnaboldi et al. 1997; Galletta, Sage & Sparke 1997; van Driel et al. 2000). The integrated colors and gas-to-dust ratio, together with the large HI/L_B ratio, suggest that PRGs may be quite similar to the late-type spirals (Arnaboldi et al. 1995).

The main goals of this work are to deeper our knowledge about the observational properties of PRGs in order to compare them with the predictions from different formation scenarios for these peculiar systems. To these aims new Near-Infrared (NIR) data (J, H and Kn bands) for a sample of polar ring galaxies are collected and analyzed. The near-IR bands is necessary to reduce as much as possible the dust absorption that strongly affects the starlight distribution in the host galaxy and in the ring. The broad band optical images of

PRGs published in the Polar Ring Catalogue (Whitmore 1990) show that the dust obscuration for some objects is so strong that it is not even clear whether the outermost structures belong the the ring or to the central galaxy. Since the optical depth of dust decreases moving to longer wavelenghts, the study of PRGs in the NIR bands would help to solve the dust problem. With NIR images the inner structures of the host galaxy and ring can be easily identify. Moreover the study of optical and NIR integrated colors yield information about the age and metallicity of PRGs. The further advantage of the NIR observation is that it is more representative of the older stellar population that contains most of the mass. So, dynamical modeling of PRGs, aimed to derive the stellar mass distribution of the two components, will strongly improve by using NIR data rather than optical ones.

The main scenarios describing the formation of PRGs are presented in Chap.1. The new NIR observations, obtained for a selected sample of polar ring galaxies (from The Polar Ring Catalogue), are presented in Chap.2. Results by the detailed analysis of the morphology, light and color distribution are discussed in Chap.3. In Chap.4 and Chap.5 are extensively analyzed two peculiar objects, ESO 235-G58 and NGC 4650A respectively, for which are also available optical data in the B, V, I bands. In Chap.6 are presented the preliminary results of an ongoing study about dynamics of PRGs. In the conclusive discussions, the main observational properties for polar ring galaxies, derived in this work, are compared with the predictions from the formation scenarios for this class of objects.

Work is still in progress: new high resolution 21-cm observations were obtained by Arnaboldi and collaborators in 1996, at the Australia Telescope Compact Array, for all polar ring galaxies of the sample presented in this work. The HI distribution and the rotational velocity curve will be derived for each object to revisit the question of the dark halo shape around PRGs: this field of study takes new particular emphasis in the light of the new results presented in Chap.6. The new NIR photometry, presented in this work, give more details on the stellar distribution in the central host galaxy and ring, thus it will help to select the best mass-to-light ratio in the future dynamical models for PRGs.

Acknowledgements - I would like to thank my Supervisors, Dr. M. Arnaboldi, Prof. L. Sparke and Prof. P.Salucci for their help and support during the realization of this work. Special thanks are given to Linda Sparke, Prof. Jay Gallagher and his family for the assistance and friendship they offered

me while I was in Madison, Wisconsin USA. Moreover, I would like to thank Prof. Ron Buta (University of Alabama, USA) that kindly gave me the optical images for the polar ring galaxy ESO 235-G58; Prof. Ken Freeman (Mount Stromlo and Siding Spring Observatory, Canberra - Australia) that obtained the optical data for the polar ring galaxy ESO 416-G26. I am also grateful to Dr. K. Bekki (University of Tokyo) that kindly sent me the animation video of the simulated merger-driven polar-ring formation, and Dr. P. McGregor (Mount Stromlo and Siding Spring Observatory, Canberra - Australia) that provided me many useful informations about the CASPIR infrared camera. Furthermore, I am very grateful to Gabriella De Lucia (MPI, Garching) that help me to use the stellar population synthesis models in order to derive the age estimate in PRGs.

I would like to thank I.S.A.S for the financial support which gave me during last month of my pregnancy and when my baby was born and special thanks are given to the Astrophysics head-sector, Prof. Luigi Danese for his kindly interest to obtain it.

I would like to thank the head of the Observatory of Capodimonte in Naples, where part of this work has been realized.

I gratefully acknowledge the help and support of my friends and PhD students at I.S.A.S, Ilaria Cagnoni, Vanessa Mangano, Giuliano Taffoni, Pasquale Panuzzo and Marco Chiaberge, and at the Observatory of Capodimonte in Naples, Ilaria Musella, Emanuella Puddu, Nicola Napolitano, Gabriella De Lucia, Lino Grado.

I would like to end with very special thanks to my husband Giovanni Marcello, my family and my parents-in-law for their aid and moral support. This work is to my son Davide.

Chapter 1

Formation Scenarios for Polar Ring Galaxies

Polar Ring Galaxies are usually considered dynamically peculiar systems, since they show the coexistence of two luminous components (the central host galaxy and ring) in two nearly orthogonal plane (Schweizer, Whitmore and Rubin 1983; Whitmore et al. 1990). The presence of two almost perpendicular angular momentum vectors, of comparable size, cannot be explained through the collapse of a single protogalactic cloud. In the local universe, the frequency of early-type galaxies with polar rings are only about 0.5% (Whitmore et al. 1990): this suggests that a very particular mechanism is required to form PRGs. In the last years, a growing number of observational studies have been produced in order to provide even more informations about the origin of PRGs (Reshetnikov 1997; see also the review by Sparke and Cox 2000). The main results concern 1) the nature of the central host galaxy, focusing on the possible correlation of its properties with the characteristics of the surrounding polar ring (Reshetnikov et al. 1994, 1996); and 2) the ring component, to which the HI gas is associated to this structure (Schechter et al. 1984a; Galletta, Sage and Sparke 1997; Arnaboldi et al. 1997; van Driel et al. 2000). The "best scenario" to describe the PRGs formation should be able to predict most of the observed properties of polar ring systems (which are described in the Introduction to this work). In particular, it should explain

1. why the morphology of the host galaxy resemble that of an S0 galaxy;
2. why PRGs are rare objects;
3. why the ring component shows different morphologies (i.e. narrow or wide rings, helical or double rings);

4. why the rings are found close to the polar plane of the host galaxy;

5. the large amount of HI gas observed in the polar structure.

Possible scenarios for PRGs formation can be grouped into two main pictures:

1. **accretion of a gas-rich dwarf galaxy by an early-type system** or **gas stripped from a nearby gas-rich object**;

2. **a major dissipative merging of two disk galaxies.**

In the next sections each item of these last will be discussed in detail and we will test how well these models may succeed in reproducing polar rings around early-type galaxies and their main properties.

1.1 Accretion Scenario

In the standard scenario the formation of PRGs is the result of a *secondary event* involving a pre-existing S0 galaxy. In this context, the mechanisms which are able to create ring-like structures around early-type galaxies are the following: accretion of matter from a nearby system or capture and merging of a gas-rich companion; delayed inflow of a primordial intergalactic cloud; polar-ring formation from the return of tidal material during the merging of two gas rich spirals (Toomre 1977; Shane 1980; Schweizer et al. 1983; Sackett 1991; Sparke 1991; Hibbard & Mihos 1995). The accreted material would then form a ring (Quinn 1991, Hernquist & Weil 1993), which settles into one of the principal plane of the gravitational potential associated with the host galaxy (Heisler, Merritt and Schwarzschild, 1982; Bertola et al. 1991).

Since the accretion of material could occur in all type of galaxies and at any angles, why only near-polar disks around early-type galaxies survive for a long time? The final structure of the accreted gas depends on the relative amount of gas present in the main galaxy at the intersecting radii, so only in relative gas-free galaxies the resistance to form a tilted disk is minimum. The evolution of the accreted gas depends strongly on the gravitational field of the galaxy, on dissipation and its self-gravity. On the relative importance of each of these factors are based the different evolutionary models.

The *preferred orientation model* (Steiman-Cameron, 1991) is based on the hypothesis that the potential of the host galaxy is triaxial rather than axisymmetric. Thus, the accreted material could settle in one of the preferred

directions: the equatorial plane or the polar one, if the ring capture occurs respectively at small or high inclinations relative to the galaxy principal plane. The differential precession, caused by the quadrupole momentum of the potential, induces the migration of the ring forward the nearest of these two directions.

The *self-gravitating model* (Sparke 1986; Sackett & Sparke 1990; Arnaboldi & Sparke 1994) explain the polar structure as the result of the accretion of a massive ring captured at high inclination in an axisymmetric galaxy. If the mass of the ring exceeds a minimum value, the self gravity of the ring make it precess as a rigid body. The really massive PRGs are stable at whatever angle and evolve independently from the potential, while for intermediate values of the mass they are stable near either 90° or 0°.

Both these models require an high inclination angle for the accretion process and predict the formation of a stationary polar ring. On the contrary, in the *statistical selection model* (Schweizer et al. 1983) the polar rings are transient features and they are seen at these higher inclinations because the timescales on which the differential precession acts are long.

Smoothed-particle hydrodynamic simulations with strong dissipative cooling, by Katz & Rix (1992) and Christodoulou et al. (1992), were used to study the evolution of low mass, highly inclined ring. They showed that a narrow ring precesses very slowly in a quasi-equilibrium configuration if 1) their ratio $\Delta R/\bar{R}$ is between 10% and 30%, where ΔR is the radial extension of the ring and $\bar{R}$ the average radius, and 2) self-gravity is at work.

Recent observations of several interacting pairs of galaxies, of comparable luminosities, show forming ring-like structures (for instance, NGC 7464/65, Li & Seaquist 1994; NGC 3808A,B shown in Fig.1.1, and NGC 6285/86, Reshetnikov et al. 1996). These observations led Reshetnikov & Sotnikova (1997) to study in detail the gas stripping scenario for the formation of PRGs. They analyzed the different morphologies generated through a smoothed-particle hydrodynamic simulations (SPH) in high speed encounters between either an elliptical or an S0 galaxy, and a comparable-mass spiral. They presented a description of the full history of the gas stripping from the spiral galaxy outskirts and its consequent capture by a satellite during a parabolic encounter. The elements of the continuous gaseous medium are represented by 10000 particles. Two interacting galaxies, the *donor galaxy* and the *accreting galaxy*, are initially separated by a very large distance ($r \sim 75$ kpc) so that the tidal effects are strongly reduced. Following a parabolic trajectory, the accreting galaxy passes in a zero-inclination in the plane of the donor galaxy disk: the orbital parameters are set in such a way the orbit regarding the accreting galaxy is

polar, i.e. its equatorial plane is taken to be perpendicular to that of the orbital motion. In these condition, the gas stripped by the accreting galaxy from the outskirts of the donor galaxy is accreted and will form a polar ring. The total amount of the accreted gas is about 10% of all gas in the donor galaxy, i.e. $10^9 M_\odot$. The average timescale of the ring formation is about 10^8 years: this value becomes shorter for ring forming around bulge-dominated galaxies. On the contrary, it becomes larger (up to $\sim 9 \times 10^9$ years) when the accreting galaxy is disk-dominated. During the steady-state settling of the newly formed ring, the two interacting galaxies are distant enough (more than 120 kpc) and the polar ring galaxy appear as an isolated object. The interesting result of these simulations concerns the morphology of the ring: with the same impact parameters, rings formed around bulge-dominated galaxies are less extended (reach about 7 kpc in diameter) than rings formed around disk-dominated galaxies, which are 13 kpc wide, at most (see Fig.1.2).

A more complete model is also performed by Reshetnikov & Sotnikova (1997): it takes into account the presence of a dark matter halo around the accreting galaxy. They assumed that the halo mass distribution is a spherical isothermal sphere. They assumed a Mass-to-Light ratio $M/L = 2$ inside a radius of 15 kpc. The geometry of the encounter is unchanged, whereas the number of gas particles increases to 20000. The timescale of the ring formation is larger than in the process involving haloless systems, and it reaches up to few Giga years. On the other hand, the mass of the ring structure, obtained in the two kind of models, are comparable and are about $2.2 \times 10^9 M_\odot$. The size of the ring changes significantly: the estimated diameter of this structure is about 30 kpc.

1.2 Merging Scenario

A quite different approach to the formation of polar ring galaxies was recently proposed by Bekki (1998). In this scenario the polar ring results from a "polar" merger of two disk galaxies with unequal mass. The "intruder", on a polar orbit with respect to the "victim" disk, passes through it near its center: it is slowed down, and pulled back toward the victim, by strong dissipation which is caused by the interaction with the victim gaseous disk (see Fig.1.3). The two galaxies have the same density profiles for the disk and rotational curve profile, whereas they have different initial gas mass fraction, which is zero

Figure 1.1: Reproduction of NGC3808 from the Atlas of Peculiar Galaxies by Arp (1966); North is at the top, East to the Left.

for the intruder and 0.2 for the victim[1]. The adopted value of 0.2 is usually observed in gas-rich spiral galaxies (e.g., Roberts & Haynes 1994). The nature of the interstellar medium (ISM) is considered to be collisional and dissipative: it was modeled with sticky-particle method (Schwarz 1981). The total number of particles involved in the simulations and relative to the victim galaxy are 10,000 for the halo component, 10,000 for the stellar disk component and 20,000 for the gas component. The total number of particles relative to the intruder are linearly proportional to the ratio between the two galaxy masses. In this scenario, a rather simplified star formation model is also taken into

[1]The different gas content of the intruder and victim is not essential for the final morphology of the merger remnant, as the strong dissipation would produce a gas free central component anyway.

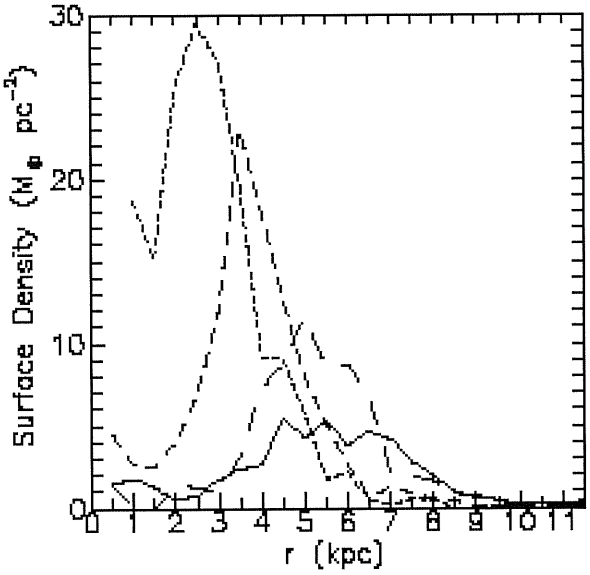

Figure 1.2: Surface density profiles of the rings, predicted by the accretion models (by Reshetnikov & Sotnikova, 1997). The short, medium and long dashed lines refer to the Bulge-to-Disk ratio B/D=2.0, 1.0, and 0.5, respectively. The solid line is for B/D=0.2 .

account: only the gas-to-star conversion is considered and important effects from feedback by Type II supernova were not included.

The orbit of the two interacting galaxies is set to be in the $x-z$ plane (see Fig.1.3) and two types of trajectories are considered: 1) the *polar collision*, where the two objects move along the x-axis, and 2) *parabolic collision*. The initial spin axis of the victim is set to be in the $x-z$ plane, and several angles between its direction and z-axis are considered (from 30^o to 90^o); the initial spin axis of the intruder is fixed to be parallel to the x-axis. In this encounter, the two galaxies, whose initial separation is about 40 kpc, must have a small relative velocity (V_{rel}), so that the intruder is brought to rest at the center of the victim's disk. The values for the relative velocity varies in the range $32.6 \leq V_{rel} \leq 326$ km s^{-1}. The most important parameter, which varies from model to model, is the initial mass ratio of the two progenitors: it controls the final morphology of the merger remnant. This ratio varies from 2.0 to 0.1 . All the above mentioned parameters are summarized in Table 1 of Bekki's 1998 paper.

Which is the mechanism of polar ring formation?

While the intruder is piercing the victim, its initially thin stellar disk becomes thicker and thicker: this is due to the strong dynamical heating during such violent gravitational interaction. Then the intruder is pulled again back through the victim and, at the same time, its stellar disk suffers violent relaxation. At this time ($t \sim 1.12 \times 10^9$ yrs), the intruder's morphology is very similar to that of an S0-like system. The density profile of this component deviates from the initially exponential behavior and it is more concentrated toward the center (see Fig.1.4 left panel), furthermore the intruder shows an appreciably larger amount of global rotation even after galaxy merging (see Fig.1.4 right panel). The polar ring, surrounding this central spheroid, is formed by the victim disk: the central part of the victim tends to be pushed out as the intruder goes through it, and, simultaneously, propagating density wave are excited in the outer regions. The violent relaxation of the galaxy merging yields the stellar component in the victim disk to become dynamically relaxed and to form a diffuse spheroidal component. The density waves generates a cloud-cloud collision in the gas medium, which tends to form compressed layers with higher density: as consequence, star formation and further dissipation start in correspondence of such layers. These last phenomena transform the victim disk into a polar ring made by gas and new stars. The typical timescale for the S0-like host galaxy and polar ring to form is about 3×10^9 yrs.

Bekki's scenario successfully reproduces many of the observed morphologies for polar ring galaxies, such as the existence of both wide and narrow rings, helical rings and double rings (Whitmore 1991). Narrow polar ring are formed through the merging of two disk galaxies, colliding on a polar orbit, when 1) the relative velocities are small ($V_{rel} \sim 33$ km s^{-1}) and 2) the intruder disk is more massive than the victim one (mass ratio comes from 1.7 to 2.0). The only different initial condition, from the previous ones, which let to the formation of wide polar rings is the mass ratio of the two merging galaxies: the victim disk must be 10 times more massive than the intruder one (mass ratio ~ 0.1). When wide polar rings are produced they are more similar to a disk-like structure, rather than a polar annulus, which are characterized by a hole in the center. Both wide and narrow polar ring galaxies have the following properties: 1) mass distributions in the central component and ring become more centrally concentrated after the encounter; an $R^{1/4}$ profile can develop if the "intruder" disk is much more massive than the "victim"; 2) the central component is nearly gas-free, similar to an S0-like system, while the density wave triggered by the intruder into the victim disk causes rapid star formation, within $\simeq 10^9$ yr, so that the polar structure is characterized by a very young stellar population.

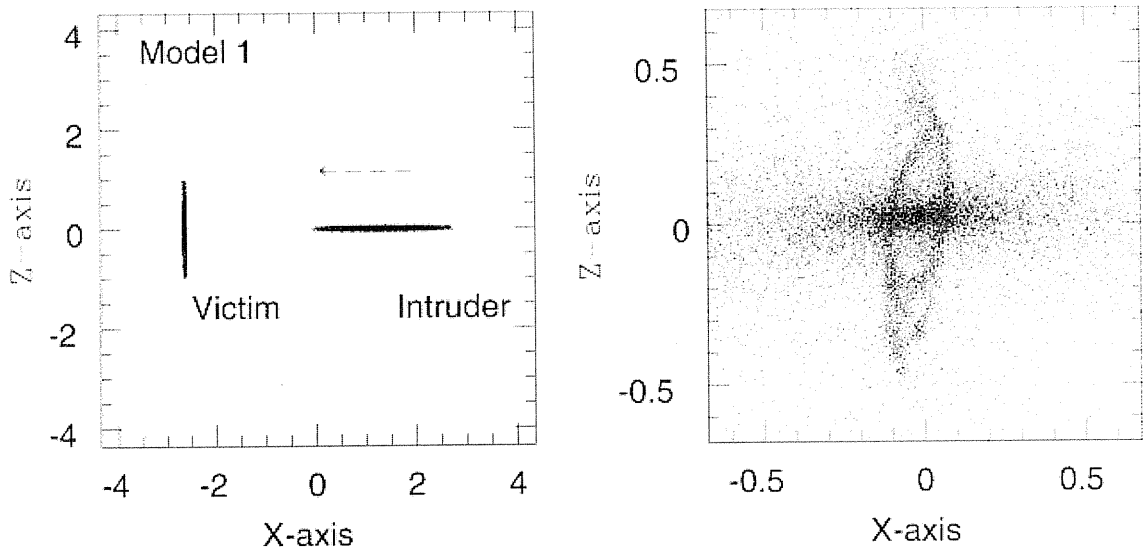

Figure 1.3: Initial mass distribution of the two progenitor disks in a galaxy merger (left panel) and final mass distribution of the merger remnant at the epoch of about 2 Gyrs (right panel) (by Bekki 1998). This result refers to one of several investigated models (see text). The arrow indicates the direction of the initial relative velocity of the two galaxies. In order to show clearer the formed polar structure, in the right panel are plotted the gas component of the victim and the stellar component of the intruder. The halo component is not plotted in these two panels.

One uncertainty related to the Bekki scenario is whether the polar rings formed in this way are stable, i.e. for how long time these objects can preserve the polar morphology after the merger remnant reaches virial equilibrium.

1.3 Discussion

How well does the two formation scenarios for PRGs, summarized here, predict most of the observed properties of polar ring systems? Both scenarios explain why PRGs are rare: they are formed in particular initial conditions for the encounter. Furthermore, they explain why the central host galaxy resemble an S0. Moreover, the orbital parameters, considered in both of them are able to explain why the rings are found close to the polar plane of the host galaxy. The accretion scenario fails in reproducing massive disk-like polar structures, and it may account for the narrow polar annuli only. Moreover, the total amount

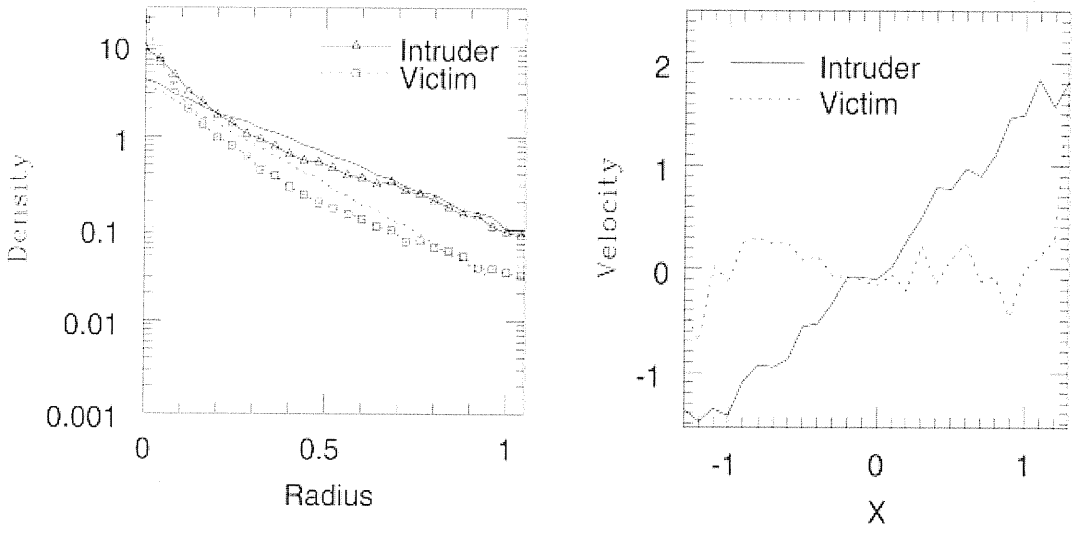

Figure 1.4: Left panel - Radial mass distribution of the intruder (solid line with open triangles) and the victim (dotted line with open squares) projected onto the x-y plane. In this panel, the initial exponential mass distribution of the victim projected onto the y-z plane (solid line) and that of the intruder projected onto the x-y plane (dotted line) are also indicated. Note that both the mass distribution of the intruder and that of the victim show deviation from the initial exponential mass distribution. Right panel - Projected velocity profile along the x-axis for the intruder (solid line) and the victim (dotted one). Both panels refers to the model where the intruder is 2 times massive than the victim and to the of $\sim 3 \times 10^9$ yr (Bekki 1998).

of accreted gas can be of the order of $10^9 M_\odot$ at most, which is the typical amount of HI in a gas-rich dwarf (Carignan 1999).

On the other hand, the merging scenario, proposed by Bekki (1998), would also explain the presence of wide and massive polar disks as well as other observed peculiar morphologies in the class of Polar Ring Galaxies. When extended polar structures are formed (depending on the intruder/victim mass ratio) they may be characterized by an high content of HI gas (up to $10^{10} M_\odot$), which originally lied in the victim disk: this is a comparable value for the HI observed in late-type spirals (Matthews & Gallagher, 1997).

Chapter 2

Polar Ring Galaxies in the Near-Infrared

Here we present the Near-Infrared (NIR) observations and main steps of the data reductions for a sample of polar ring galaxies, all selected from the Polar Ring Catalogue (Whitmore et al. 1990) but ESO 235-G58, listed in Tab.2.1. We performed a detail morphological study for the host galaxy and ring in all PRGs in our sample and the color distributions are derived for both components. The polar ring galaxies ESO 235-G58 and NGC4650A are analysed in more detail in Cap.4 and Cap.5, respectively.

2.1 Observations and data reduction

2.1.1 NIR data

The near-infrared J, H and Kn images were obtained during several observing runs at the 2.3 m telescope of the Mt. Stromlo and Siding Spring Observatory, with the CASPIR infrared camera (McGregor 1994), which is described in Appendix A. The angular resolution of this camera is 0.5 arcsec/pixel and it has a field of view of $2.0' \times 2.0'$. The observing log for these data is summarized in Tab. 2.2.

Images were acquired in the offsetting mode: a cycle was defined containing 5 images on target, interspersed with 5 sky frames; each object frame was taken with a small offset from the galaxy center and the sky frames were taken before and after each galaxy frame. Dark frames were were acquired at the beginning and of the end of each cycle, bias frames at the beginning and end of each set of cycles. In the Kn band there are more cycles than in the J and H band,

Table 2.1: The Polar Ring Galaxy sample studied in this PhD thesis. In the second column is reported the the object identification as given in the Polar Ring Catalogue, PRC, (Whitmore et al. 1990); the Heliocentric velocities, total photographic magnitudes and galaxy extension are reported in the fifth column, sixth and seventh column respectively. These last informations are derived by NED database.

Object name	PRC name	α (J2000)	δ (J2000)	V_0 (km/s)	m_B	diameters (arcmin)
A0136-0801	A-01	01h38m55.2s	-07d45m56s	5500	16.9	0.41 x 0.3
ESO 415-G26	A-02	02h28m20.1s	-31d52m51s	4604	14.81	1.3 x 0.6
NGC 4650A	A-05	12h44m48.8s	-40d42m50s	2861	13.9	1.6 x 0.8
ARP 230	B-01	00h46m24.2s	-13d26m32s	1742	13.75	1.3 x 1.2
AM 2020-504	B-19	20h23m54.8s	-50d39m05s	4963	14.5	
ESO 603-G21	B-21	22h51m22.0s	-20d14m51s	3124	15.31	1.1 x 0.6
ESO 235-G58		21h06m28.3s	-48d07m15s	4265	15.14	2.4 x 1.6

in order to have a better estimate of the background level. Unfortunately, for A0136-0801, due to the clouds at the end of the third night, only the H band observations are available.

The data reduction is carried out by using the CASPIR package in IRAF[1] (*Image Reduction and Analysis Facility*) enviroment. The main strategy adopted for each dataset is the following:

- linearization;
- flatfielding correction;
- sky subtraction;
- rejection of bad pixels;
- registering and co-addition of all frames into the final scientific frame.

[1]IRAF is distributed by the National Optical Astronomy Observatories, which is operated by the Associated Universities for Research in Astronomy, Inc. under cooperative agreement with the National Science Foundation.

Several standard stars, from Carter & Meadows (1995), were observed at the beginning, middle and at the end of each observing night, in order to transform strumental magnitudes into the standard J, H and Kn band systems.

All the objects of the sample except NGC4650A are small: they subtend a diameter of about $\sim 1'$ on the sky and therefore lie well inside the detector field, so they allow for a suitable estimate of the sky background. For NGC4650A it was necessary to make a mosaic of two frames.

The calibrated images of each object are shown in Appendix B.

2.1.2 Optical data

The B band images for the polar ring galaxies ESO 603-G21, AM 2020-504 and ARP 230 (Fig.2.1), used in the present work were obtained by Arnaboldi and collaborators (Arnaboldi et al. 1995), either to study the dust distribution and photometric properties of these objects (Arnaboldi et al. 1995).

For ESO 415-G26 new B band data were recently acquired, by K.C. Freeman, at the Mt. Stromlo and Siding Spring Observatory (SSO) 2.3 m telescope. The imager at the SSO 2.3 m telescope has a field of view of 10'x 10' and an angular resolution of 0.59 arcsec/pixel. The dataset included 3 BIAS frames, 3 different images of the twilight sky (to derive the flatfield image) and 5 object frames taken with the offsetting mode. Moreover, standard stars in the E2-region (Graham, 1982) were observed in B and V bands in order to establish the photometric zero point for the B band system. To obtain the final B band image for ESO 415-G26 (Fig.2.1, top left panel), the data reduction is similar to that described for the NIR images (see Sec.2.1). The CCDRED package in IRAF was used to linearise, flatfield and combine these B band images. The observing log for all B band data is given in Tab.2.3.

2.2 Host galaxy and polar ring morphology

The NIR images of all objects in the sample show that most of the NIR light comes from the host galaxy and its morphology resembles that of flattened ellipsoid, most likely a Lenticular S0 galaxy (see Fig.B.1 to Fig.B.8). All the objects but NGC4650A and A0136-0801 have an additional faint feature in their light distribution, a *ring*, whose radius is whithin the outer isophote of the central galaxy and it has thin width. In NGC4650A (Fig.B.8) and A0136-0801 (Fig.2.2, left panel) the polar ring is more extended in radius than the host galaxy, it has a considerable width and it hosts several star formation regions, as the suggested by the irregular light distribution.

Table 2.2: NIR data for the selected sample of polar ring galaxies.

Object	Filter	Tot. int. (s)	FWHM (arcsec)	Date
A0136-0801	H	180	3.7	20/08/1995
ESO 415-G26	J	120	3.1	20/08/1995
	H	120	1.9	19/08/1995
	H	120	2.3	20/08/1995
	Kn	180	1.4	18/08/1995
	Kn	60	1.3	19/08/1995
ARP 230	J	180	1.5	19/08/1995
	H	180	1.6	19/08/1995
	Kn	480	1.6	18/08/1995
AM 2020-504	J	240	2.2	18/08/1995
	H	240	1.4	18/08/1995
	Kn	180	1.8	19/08/1995
	Kn	240	2.0	20/08/1995
ESO 603-G21	J	180	1.5	19/08/1995
	H	240	1.6	19/08/1995
	Kn	360	1.5	20/08/1995
ESO 235-G58	J	240	1.6	19/08/1995
	H	240	1.5	19/08/1995
	H	120	1.6	20/08/1995
	Kn	480	1.5	18/08/1995
	Kn	120	1.4	20/08/1995

Table 2.3: Optical B band data for the selected sample of polar ring galaxies. Data for ARP 230, AM 2020-504 and ESO 603-G21 are from Arnaboldi et al., 1995.

Object	Telescope	Tot. int. (s)	FWHM (arcsec)	Date
ESO 415-G26	2.3m MSSO	1200	3.3	28/01/2001
ARP 230	2.3m MSSO	1800	1.4	23/08/1995
AM 2020-504	40" MSSO	1500	2.9	21/09/1992
ESO 603-G21	2.2m ESO	2400	1.6	03/08/1992

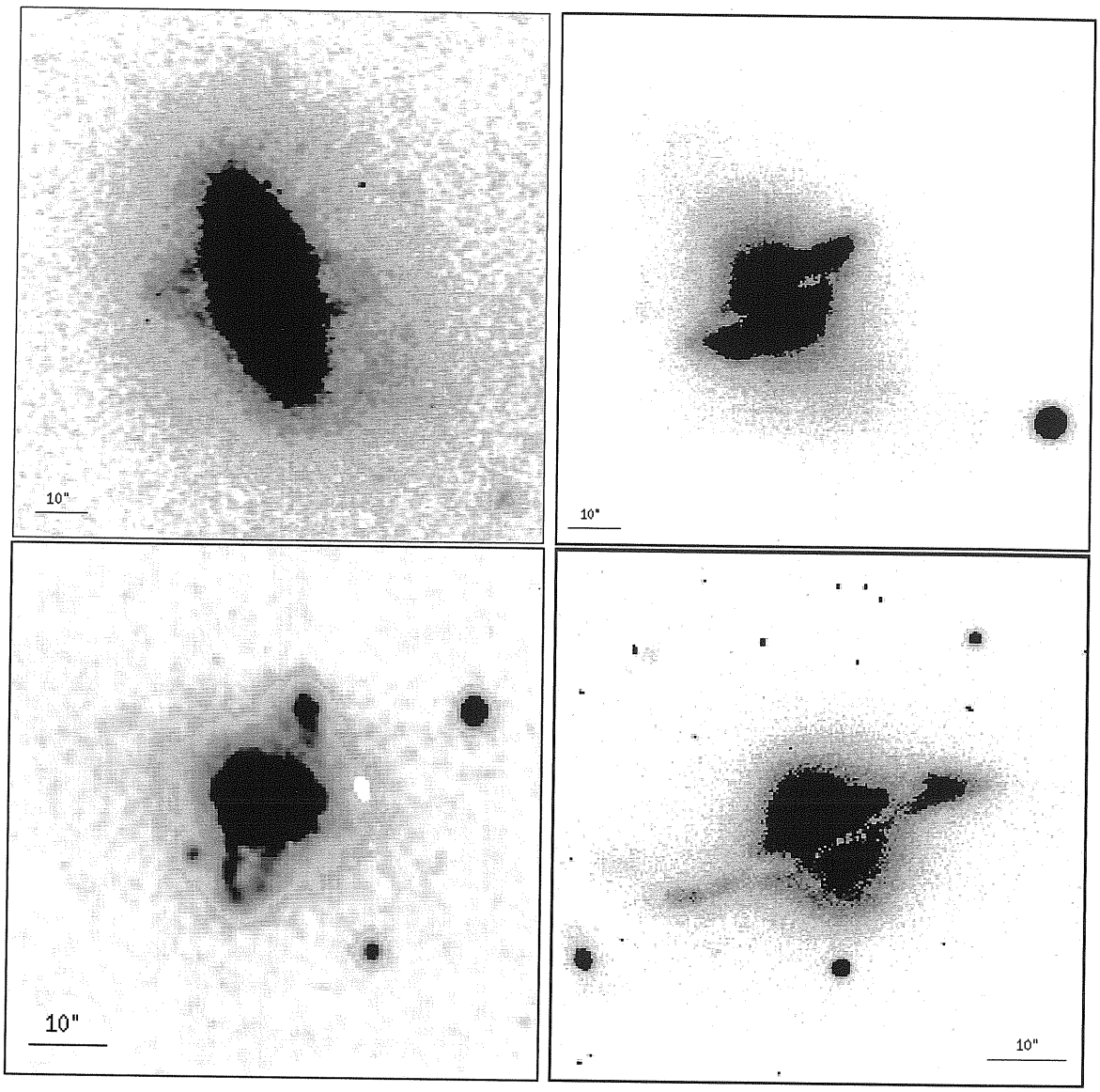

Figure 2.1: B band images for ESO 415-G26 (top left panel), ARP 230 (top right panel), AM 2020-504 (bottom left panel) and ESO 603-G21 (bottom right panel). Units are intensity; North is up and East is to the left.

We wish to identify the high frequency residuals with respect to the homogeneous light distribution. To this aim, we produce a median filtered image where each original pixel value is replaced with the median value in a sliding rectangular window. The window size (7×7 pixels) was chosen to provide the optimum enhancement of the S0 inner structures. The un-sharp masked images are obtained as ratios between the final galaxy frame and its median filtered image (computed with the FMEDIAN package in IRAF) : this ratio represents the "high-frequency residual image" and it is produced for all NIR bands (see Fig.2.2 and Fig.2.3 for the H band and from Fig.B.1 to Fig.B.8 for J and Kn bands).

The most important result obtained from this analysis is the identification of a disk-like structure along the major axis of the host galaxy for all objects but AM2020-504 (Fig.2.2 and Fig.2.3). Furthermore the high-frequency residual images reveal (in ESO603-G21 and ARP230) additional fainter structures in the inner regions of the host galaxy, which are probably related to the polar ring (Fig.2.2 and Fig.2.3, bottom panels). All these luminous components become even more evident in the H and Kn bands, as the pertubations due to dust absorption decreases in these bands. In Sec.3.5, the high-frequency residual images for all objects and in all bands are discussed in detail.

2.3 Photometry: light and color distribution

The J, H and Kn luminosity profiles were derived along the major axis of the host galaxy in each object and they are shown in the left panels of Fig.2.4 and Fig.2.5. To map the whole polar ring extension, the surface brightness profiles for this component are the results of an average of several profiles extracted in a cone, centered on the host galaxy and several degrees wide around the Position Angle (P.A.) of the ring major axis (right panels of Fig.2.4 and Fig.2.5). The width of the cone depends on the inclination respect to the line-of-sight and the radial extension of the ring.

The J-H and H-K color maps, derived for ESO 415-G26, ARP 230, AM 2020-504 and ESO 603-G21, are shown in Fig.2.6 and Fig.2.7 respectively: in all PRGs but AM2020-504, there is a redder region which corresponds to the disk-like component already identified in the high-frequency images (Sec.2.2). The characteristics of the light and color distributions in each object will be discussed in detail in Sec.3.5.

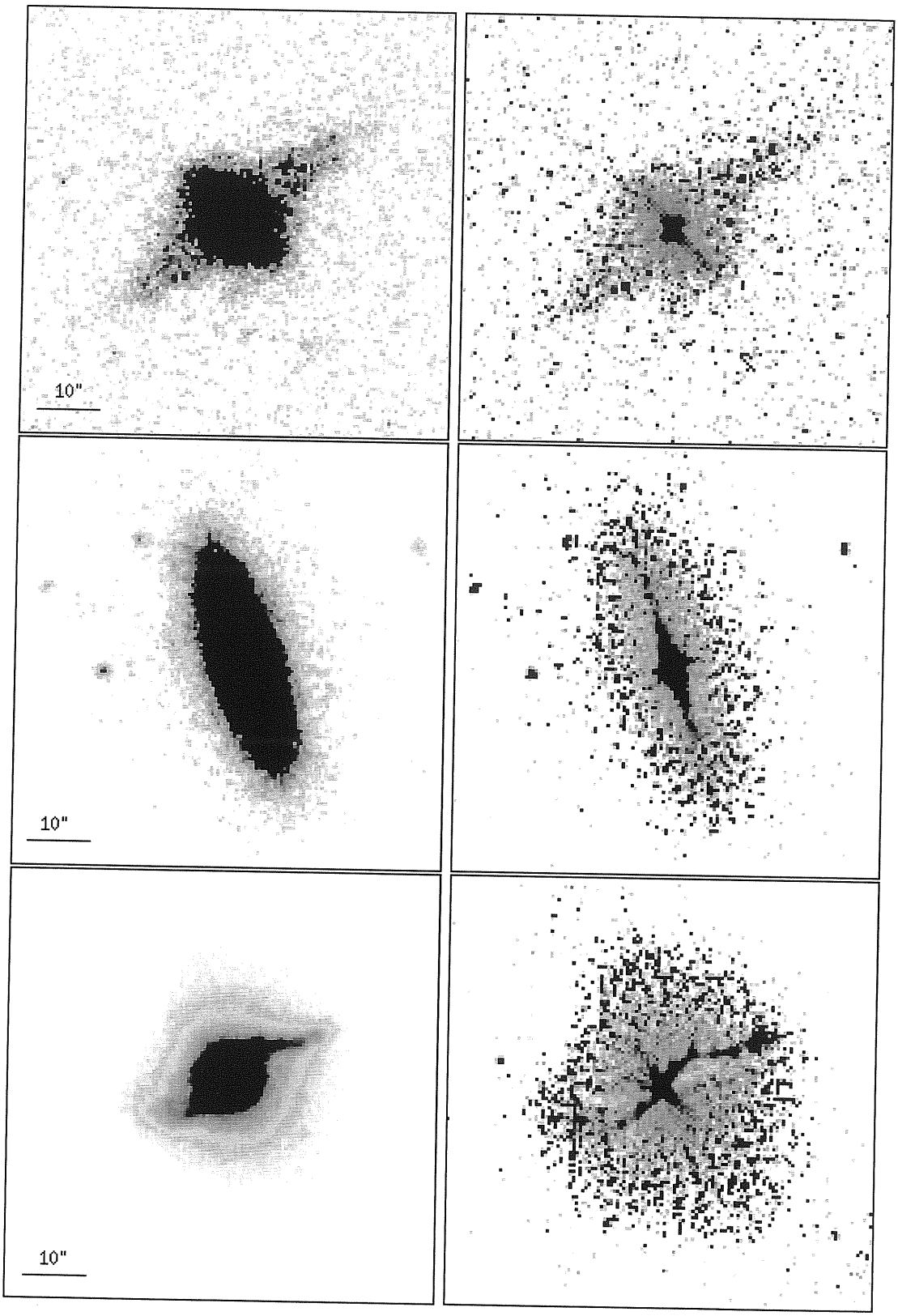

Figure 2.2: H band images (left panels) and relative high-frequency residual images (right panels) for A0136-0801 (top panels), ESO415-G26 (middle panels) and ARP230 (bottom panels). Darker colors correspond to brighter features. Units are intensity; North is up and East is to the left.

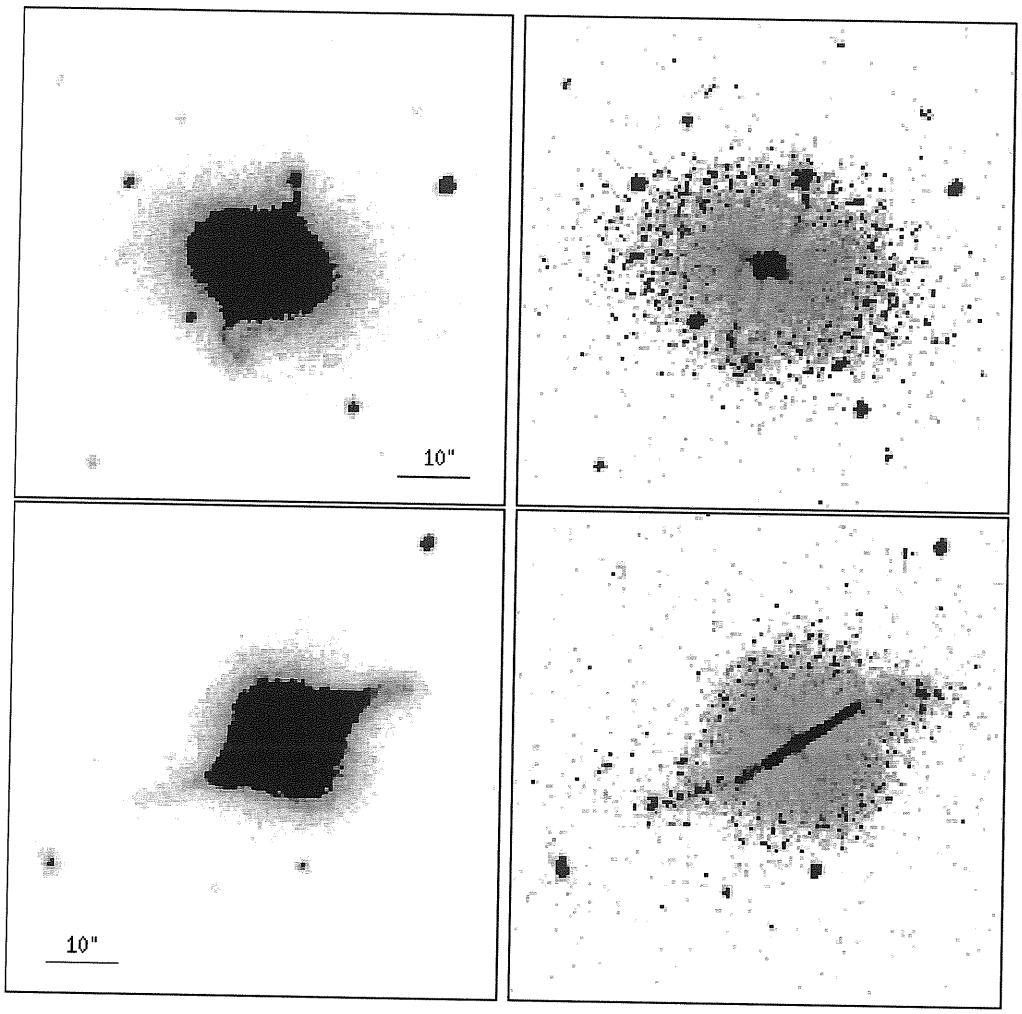

Figure 2.3: H band images (left panels) and relative high-frequency residual images (right panels) for AM2020-504 (top panels), and ESO603-G21 (bottom panels). Darker colors correspond to brighter features. Units are intensity; North is up and East is to the left.

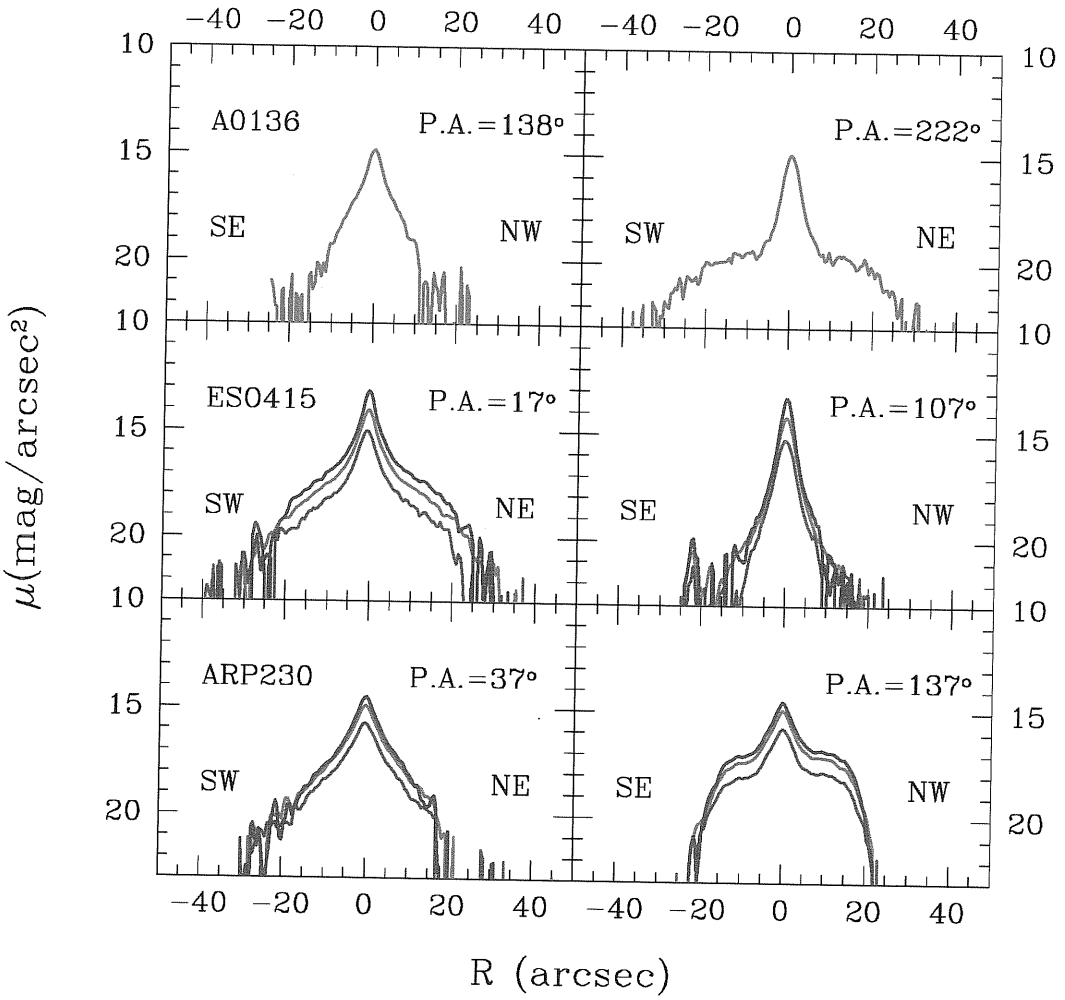

Figure 2.4: J (blue), H (light blue) and Kn (red) light profiles along the host galaxy major axis (left panels) and along polar ring major axis (right panels) for A0136-0801, ESO 415-G26 and ARP 230.

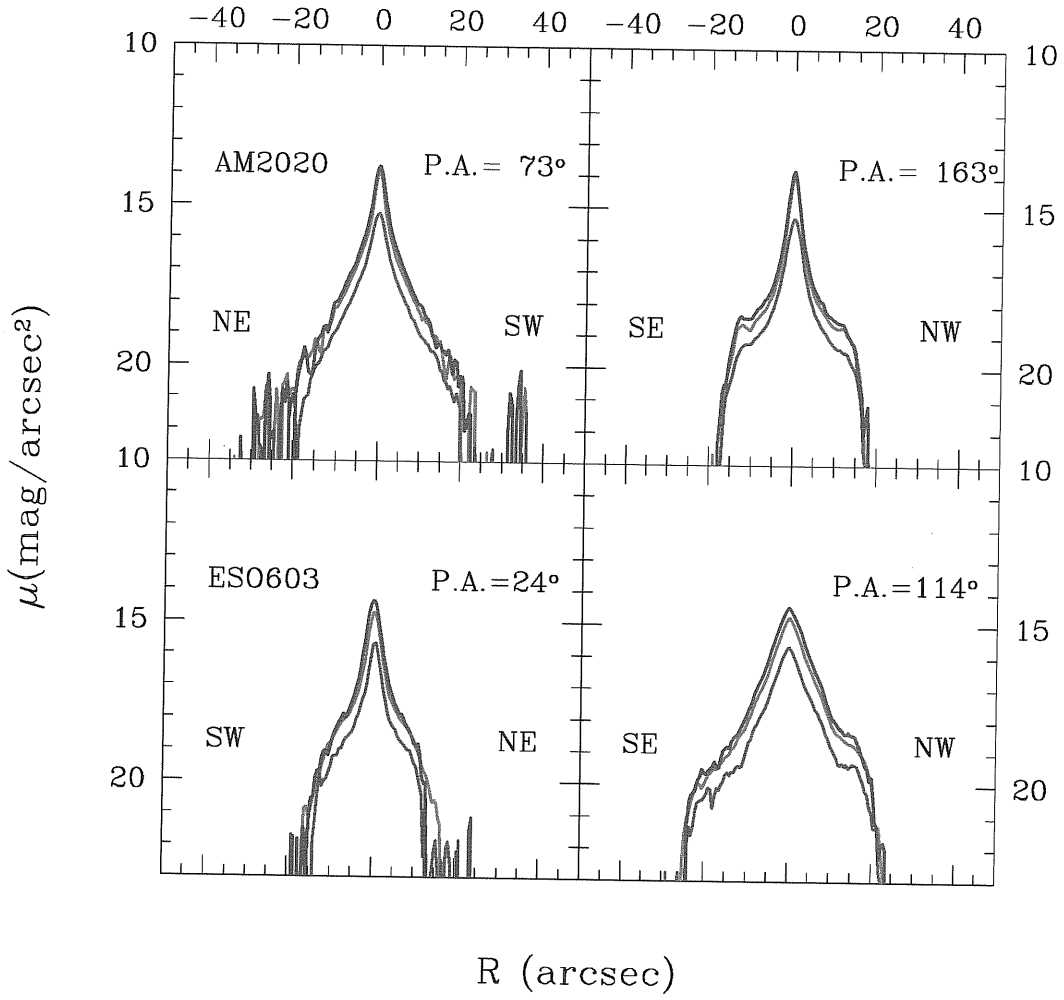

Figure 2.5: J (blue), H (light blue) and Kn (red) light profiles along the host galaxy major axis (left panels) and along polar ring major axis (right panels) for AM 2020-504 and ESO 603-G21.

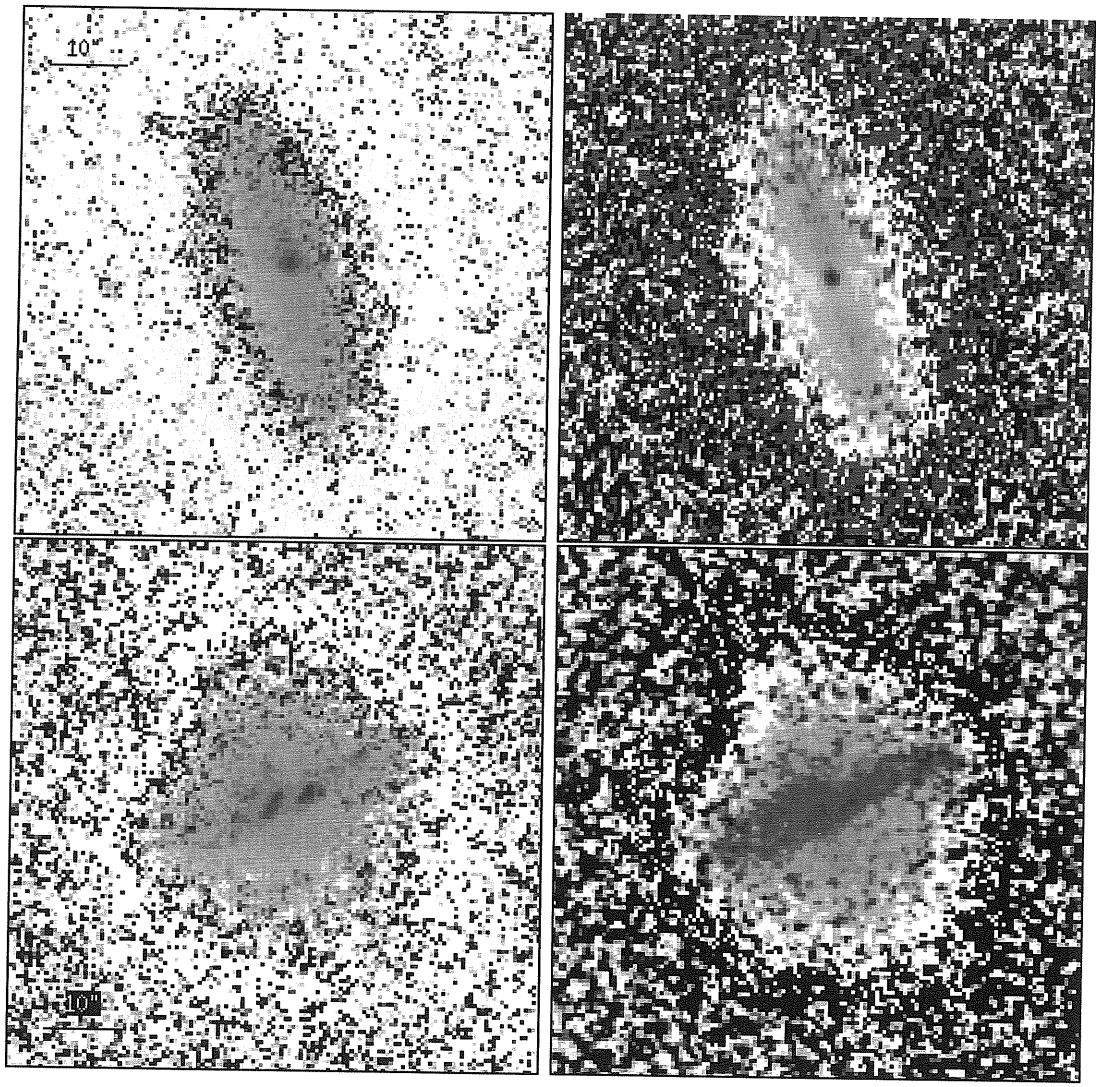

Figure 2.6: J-H (left panels) and H-K (right panels) color maps for ESO415-G26 (top panels) and ARP230 (bottom panels). Color code in each map is: darker regions correspond to redder colors, and lighter regions correspond to bluer colors. North is up and East is to the left.

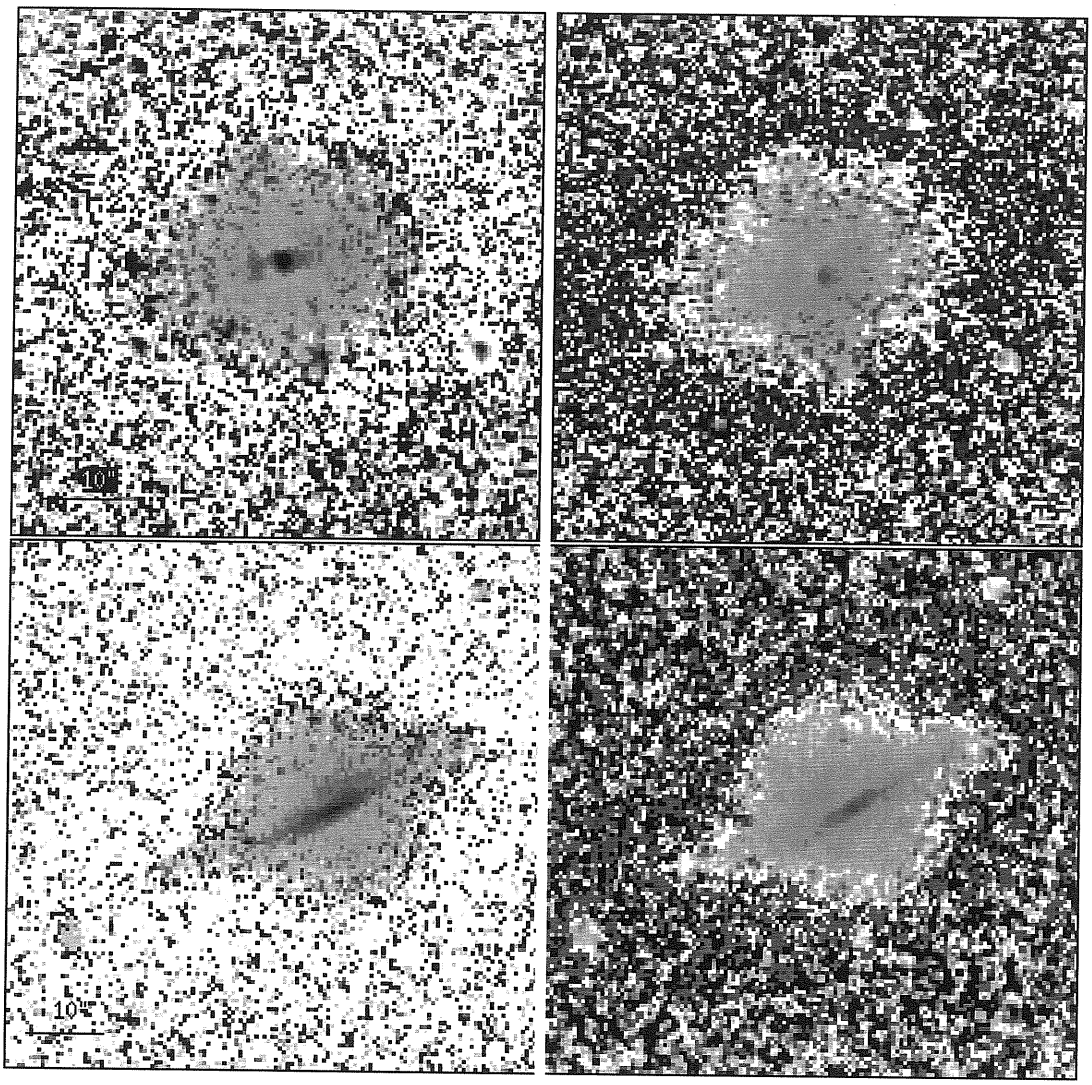

Figure 2.7: J-H (left panels) and H-K (right panels) color maps for AM2020-504 (top panels) and ESO603-G21 (bottom panels). Color code in each map is: darker regions correspond to redder colors, and lighter regions correspond to bluer colors. North is up and East is to the left.

Table 2.4: Absorption coefficients for the Galactic exctinction.

Object	A_B (mag)	A_J (mag)	A_H(mag)	A_{Kn}(mag)
A0136-0801	0.115	0.024	0.015	0.01
ESO 415-G26	0.073	0.015	0.01	0.006
ARP 230	0.083	0.017	0.011	0.007
AM 2020-504	0.185	0.039	0.025	0.016
ESO 603-G21	0.144	0.030	0.019	0.012

2.4 Integrated magnitudes and colors

The integrated magnitudes are computed in the optical, B band, and in the NIR, J, H and Kn bands, for each PRG in five different areas. These five areas are chosen as follows: one is coincident with the nucleus; two areas are placed within the host galaxy stellar component (outside the nucleus, in regions unperturbed by the polar ring), and two areas for the polar ring. In Fig.2.8 are shown these regions for each object of the sample. The polygons contours limiting these areas are determined in the J image and the same are used for H and Kn bands, after the images where registered to the J image. Polygons are marked by using the IRAF task POLYMARK and the integrated magnitude inside each of them is evaluated using the IRAF task POLYPHOT. A detailed discussion about the photometric errors is given in the next section. The integrated magnitudes and colors derived in each area, for all PRGs, have been corrected for the extinction within the Milky Way, by using the values for the absorption coefficient in the B band (A_B) and the color excess $E(B-V)$ derived from Schlegel et al. (1998). The absorption coefficients for the J, H and Kn bands (A_J, A_H, A_{Kn}) are derived by adopting $R_V = A_V/E(B-V) = 3.1$, from Cardelli et al. (1989). The values of the absorption coefficients A_λ adopted for each object are listed in Tab.2.4. The corrected integrated magnitudes and colors are listed in Tab.2.5.

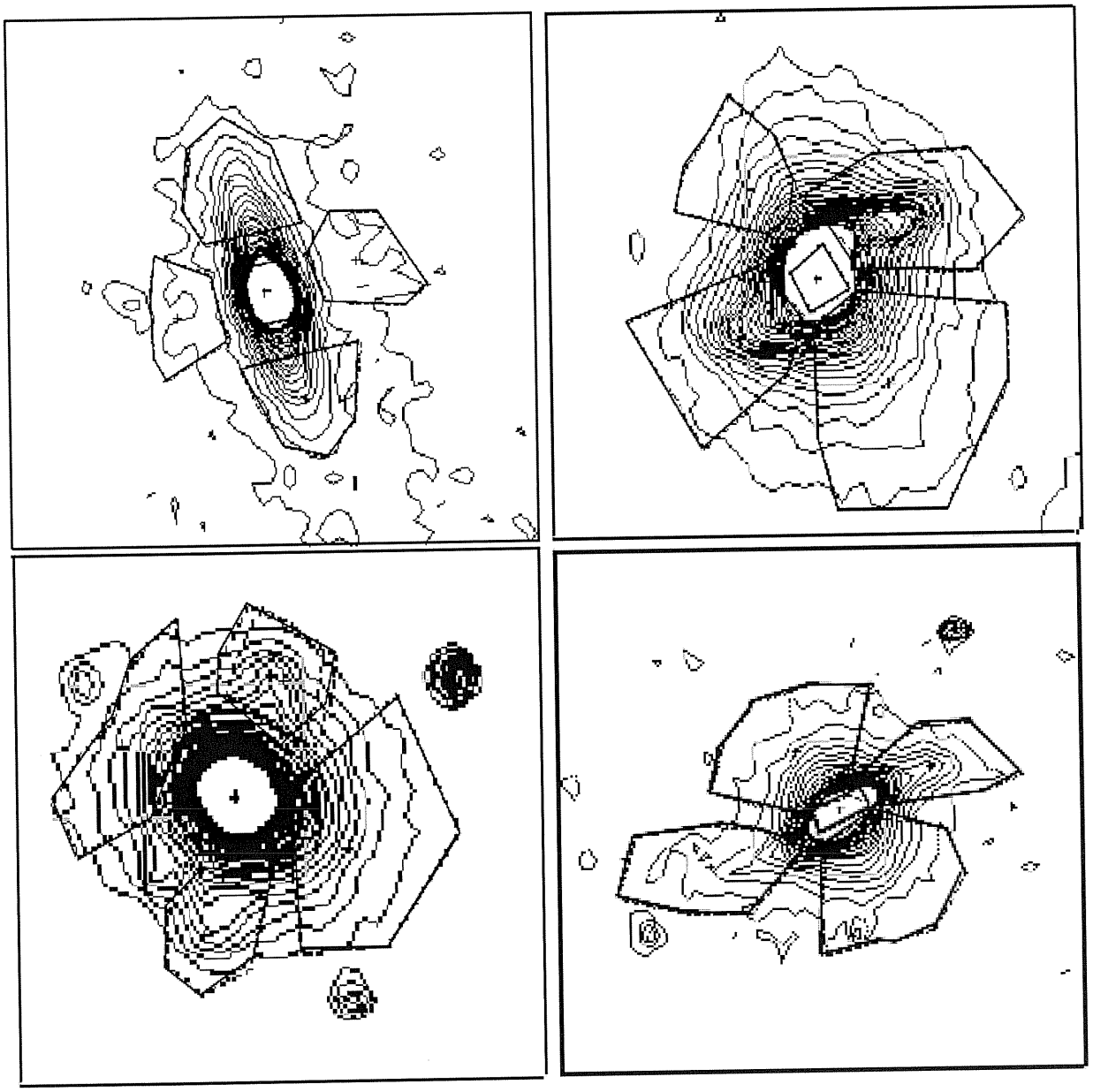

Figure 2.8: Intensity contour plot in the J band plus the five polygons limiting the different areas where the integrated magnitudes are computed (heavier lines) for ESO415-G26 (top right panels), ARP230 (top left panels), AM2020-504 (bottom right panels) and ESO603-G21 (bottom left panels). North is up and East is to the left.

Table 2.5: Integrated magnitudes and colors of different regions of host galaxy and polar ring.

Object	component	region	m_B (mag)	m_J (mag)	B-H	J-H	H-K	J-K
ESO 415-G26	PR	SE	17.97	16.25	2.10	0.38	0.35	0.74
	PR	NW	17.22	15.90	2.06	0.24	0.41	0.66
	HG	SW	17.16	14.96	2.20	0.63	0.45	1.08
	HG	NE	16.78	14.87	1.92	0.71	0.51	1.22
	HG	center	15.80	13.42	3.18	0.80	0.53	1.33
ARP 230	PR	SE	15.96	14.24	2.29	0.57	0.29	0.85
	PR	NW	16.24	14.81	1.94	0.51	0.29	0.81
	HG	SW	15.71	13.89	2.3	0.48	0.20	0.67
	HG	NE	16.25	15.02	1.81	0.57	0.19	0.76
	HG	center	16.42	13.97	3.21	0.75	0.32	1.08
AM 2020-504	PR	NW	18.10	15.96	2.54	0.57	0.27	0.86
	PR	SE	17.96	16.07	2.32	0.60	0.19	0.81
	HG	SW	18.03	15.03	3.40	0.60	0.17	0.79
	HG	NE	18.19	15.43	3.22	0.63	0.21	0.85
	HG	center	16.63	13.50	3.73	0.77	0.25	1.04
ESO 603-G21	PR	SE	17.71	15.92	1.90	0.46	0.45	0.91
	PR	NW	17.68	14.95	2.07	0.58	0.37	0.96
	HG	SW	17.29	14.83	3.03	0.57	0.37	0.94
	HG	NE	17.24	14.83	3.00	0.59	0.33	0.92
	HG	center	18.96	14.19	5.71	0.94	0.40	1.34

2.5 Tests on the background noise distribution and error estimate

The uncertainties which affect the integrated magnitudes, derived for each object of the sample, are strictly related to the noise in the image background level. The *background noise* is made up by the residual random fluctuations in the data, which appear after the background level was subtracted to the image. Usually, a Poisson distribution is assumed to describe these fluctuations. A non correct flatfield correction may introduce further fluctuations in the background, which may strogly influenced the uncertainties on magnitudes. Thus, the error estimate, must take into account both the *background noise*

and *flatfield errors.*

In order to check and see if the background noise, in the NIR images, is well described by the Poisson distribution, we sampled the sky background around the edge of the image, in each band and for each image, and we have performed the following test: in our summed, sky-subtracted images, we considered boxes on the sky, whose areas increse from 25 $pixels^2$ to even larger areas[2]. For each size, we examined 6 different boxes, in which are derived the mean value. We computed the average of the mean values and derived the relative standard deviation (SD_m). In Fig.2.9 (right panel) is plotted the SD_m vs area, and the SD_m vs $1/\sqrt{area}$ (left panel), derived for the Kn band image of NGC 4650A. The sloping line corresponds to Poisson noise, if the count in each pixel has unit standard deviation. This plot suggests that SD_m decreases as the area increases, but it has larger values than those predicted from a Poissonian statistics. The SD_m tends to a constant[3] value (about 0.04).

So, we found that there is more noise within moderate sky regions than predicted by a pure counting model. The error estimate must take into account this "extra noise".

We estimated the total error in a given area (A), which includes both the Poissonian error and that by the extra-noise, by the standard deviation of the mean counts per pixel multiplied by the area: $SD_m \times A$.

Furthermore, one should take into account the error due to a bad flatfield correction. We can derive an estimate of this quantity by this second test: we derived the statistics in many (30) sky boxes (20x20 pixels), in which we tried to avoid stars, for the J, H and Kn images. We derived, for each band, the average of the mean values and the standard deviation (SD_m). These SD_m values give an estimate for the flatfield error in each band.

The *total error*, relative to each pixel value, includes both of these two contributions. We derived the errors on magnitudes and colors for each bands in the following way: the integrated magnitudes (listed in Tab.2.5) are given by $m = ms + q + k - A_\lambda$, with ms is the instrumental magnitude, q is the zero point, k and A_λ are the correction coefficients for the atmospheric and galactic extinction. The uncertainties on these two last parameters are negligible and we consider only the errors relative to ms and q. These are independent quantities, so the error in our derived magnitude is given by

$$\sigma_m = \sqrt{err_{ms}^2 + err_q^2} \tag{2.1}$$

[2]The largest area depends on how extended the galaxy is on detector field.

[3]The last two points deviate because on larger areas are inevitably included bright sources.

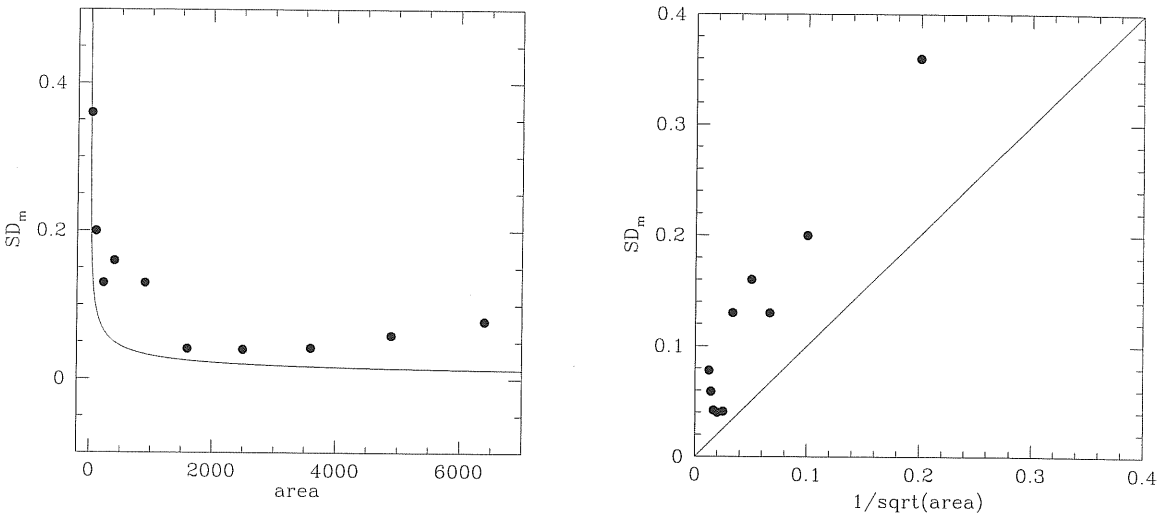

Figure 2.9: Plot of the SD_m vs area (right panel), and the SD_m vs $1/\sqrt{area}$ (left panel). The sloping line corresponds to Poisson noise, if the count in each pixel has unit standard deviation.

with $err_ms = 1.0857 * (SD_m \times A)/flux(A)$ and $flux(A)$ is the total flux in the area A. The average errors on integrated magnitudes are about 0.3%, then we obtained an average error of about 13% on NIR colors.

There is no easily explanation for the no longer Poissonian distribution in the background noise. It is known that in the NIR images the background level is very high, respect to the optical ones, so more care is needed when subtracting it from the images. Thus it could be reasonable to suppose that the extra noise may be related just to the sky-subtraction step in the data reduction.

Chapter 3

Global Properties of Polar Ring Galaxies

Here we discuss the integrated colors and light distribution properties derived for the host galaxy and ring in all PRGs of our sample (Tab.2.1), except for ESO 235-G58 and NGC4650A, whose photometric properties will be analyzed in Cap.4 and Cap.5, respectively. The aims of this study are:

1. to compare the integrated colors of the main components (host galaxy and polar ring) with those of standard morphological galaxy types and whether differences in colors are related to dust absorption or to real differences in stellar populations;

2. to estimate the stellar population ages in PRGs;

3. to understand whether the host galaxy is really a standard early-type system as its morphology suggests, by analyzing its structural parameters.

In this Chapter and then in the next ones, we adopted the color code listed in Tab.3.1 to identify each PRG of our sample.

3.1 NIR colors

The J-H vs. H-K integrated colors, derived for the host galaxy and ring, listed in Tab.2.5, are compared with those of (1) standard early-type galaxies in the Fornax and Virgo clusters (Persson et al., 1979), (2) spirals (Giovanardi & Hunt, 1996; Frogel, 1985; de Jong & van der Kruit, 1994), (3) dwarf ellipticals

Table 3.1: Color code used to identify each PRG of our sample.

Object	Color
A0136-0801	yellow
ESO 415-G26	purple
ARP 230	light blue
AM 2020-504	red
ESO 603-G21	green

(Thuan, 1985), (4) low surface brightness galaxies, LSB, (Bergvall et al. 1999), and with the inner regions of Seyfert 1 and 2 (Glass and Moorwood, 1985) (see Fig.3.1). The host galaxy in all PRGs of the sample, except for AM2020, has on average bluer colors than the typical values for early-type galaxies, and they are more similar to the colors of spiral and dwarf galaxies. Furthermore, this component is characterized by a strong color gradient, toward bluer colors in the J-H index, from central regions to the outer ones, which have, on the other hand, similar H-K colors. By assuming a screen model approximation to describe the dust distribution inside the galaxy and using $A_V = 0.3$ as in the Milky Way (Gordon, Calzetti & Witt 1997), the reddening vector is computed and it is shown in (Fig.3.1). It suggests that the dust reddening in these bands is small, but, taking into account the average uncertainties on the colors estimate, it may explain the observed color gradient in most objects, between nucleus and stellar component in the host galaxy, with the exception of ESO 603-G21. The central regions of this galaxy seems to have colors typical of a Seyfert, the same result was obtained by Arnaboldi et al. in 1995, by studying this object in B,R and K bands. ESO 415-G26 looks pretty strange, as well. But the central parts may have heavy dust extinction and this would move points toward the Seyfert region.

The polar structure has on average bluer colors than the host galaxy. The two regions of the polar ring component, in almost all PRGs, seems to have different H-K colors. Such difference may be caused by two combined effects: the dust absorption and light scattering. In these conditions, the screen model is inadequate to describe the color distributions.

A detailed discussion about the NIR colors for each PRG is presented in Sec.3.5.

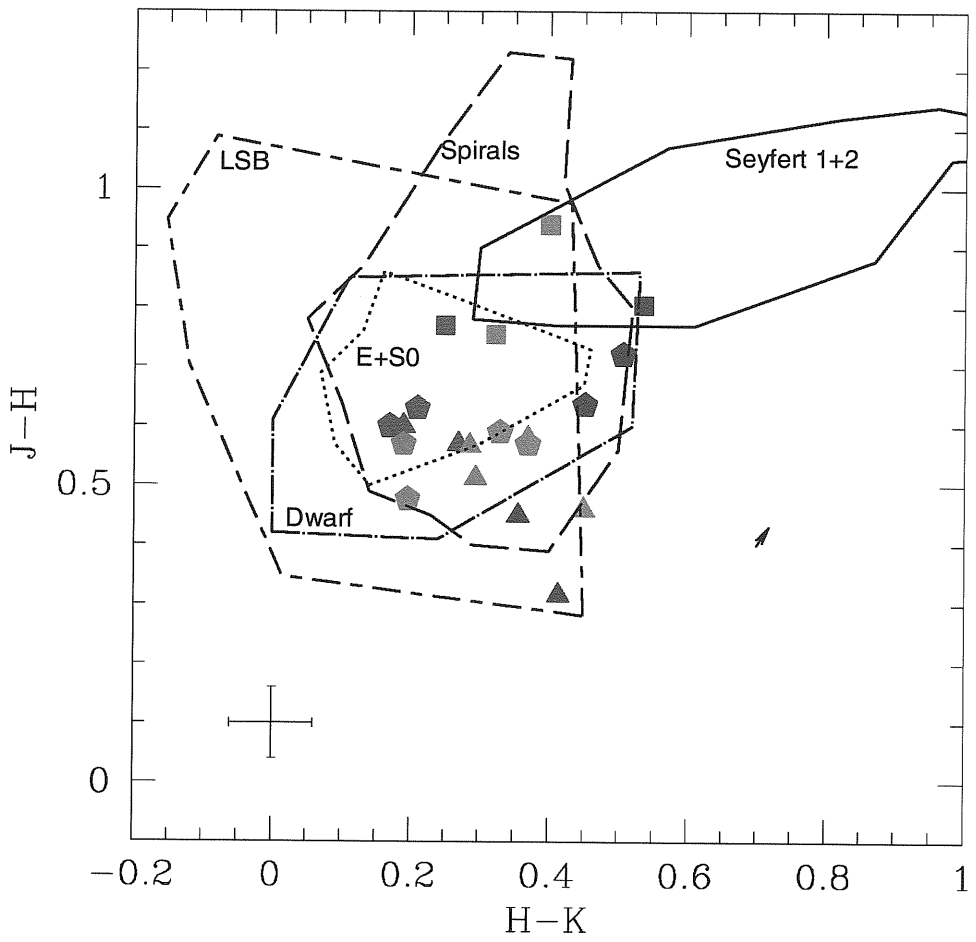

Figure 3.1: J-H vs. H-K color diagram for the five areas in each PRG of the sample, color code is listed in Tab.3.1. Filled square indicates the central region of the host galaxy; filled pentagons indicate the stellar component outside the central region; filled triangles indicate the polar ring regions. The dotted contour limits the region where the integrated colors of Es and S0s are found; the long-dashed contour limits the integrated colors of spirals; the dashed-dotted contour identifies the integrated colors of the dwarf elliptical galaxies; the long dashed - short dashed contour identifies the integrated colors of LSB galaxies, and the continuous line limits the integrated colors of the nuclear regions of Seyfert 1 and 2 galaxies. In the lower left corner are shown the average uncertainties which affect colors. The arrow, in the lower right corner, indicates the reddening vector direction for galactic dust and the screen model approximation, quoted in Sec.3.1.

3.2 Using colors to date the stellar populations in PRGs

The stellar population synthesis model developed by Bruzual & Charlot (1993), GISSEL (*Galaxies Isochrone Synthesis Spectral Evolution Library*) was used to reproduce the integrated colors of different regions (see Sec.2.4) in each polar ring galaxy of the sample. The goal is to derive an estimate of the stellar population ages in the central spheroid and in the polar structure. The starting point is to select a set of models which were able to reproduce, on average, the integrated colors of galaxies, with different morphological types, in the local Universe. These models were then optimized to reproduce the observed colors for the two main components of each PRG. Here we have decided to use the B-H vs. J-K integrated colors as they are used to break the age-metallicity degeneracy, as suggested by Bothun et al. (1984). As stated by Bothun, the J-K color gives a good estimate of the metallicity and it is quite insensitive to the presence of a young stellar population. This effect is also supported by the observed monotonic increase of the mean J-K color in globular clusters with increasing metallicity (Aaronson et al. 1978, Frogel et al. 1983). In addition, the population synthesis models by Bothun (1982) show that J-K is decreased only by 0.05 mag as a result of a star burst, while the B luminosity is increased by 1 mag by the same star burst. The B-H color is sensitive to the combined effect of the Star Formation Rate (SFR), metallicity and age (Bothun et al. 1984).

Fig.3.2 shows that in the B-H color, the host galaxy in all PRGs of the sample, but AM2020, has overall bluer colors than the average values for early-type galaxies (Bothun, 1990), and, on average, they are very similar to those of spirals (by Bothun, 1984). So, for the central component of PRGs, one could expect a younger age than those predicted for early-type systems. In this diagram it is evident that, in almost all objects, one side of the host galaxy is bluer than the other side: this is most likely caused by the presence of the polar ring, which perturbs the regions where it passes in front of the galaxy with respect to the observer line of sight.

As was already found in the NIR colors (Sec.3.1), there is a strong color gradient between the central region of the host galaxy and its outer parts, for all PRGs of the sample. The very red B-H colors of nuclear regions may be due to the dust absorption: in ARP 230 (Fig.2.1, top right panel), as extreme examples, most of light in the nucleus is completely obscured by dust in the optical band. The reddening vector, shown on Fig.3.2, is also computed for these color indices, by assuming a screen model approximation to describe the

dust distribution inside the galaxy and using $A_V = 0.3$ as in the Milky Way (Gordon, Calzetti & Witt 1997). The absorption due to the dust may account for the color gradient in the host galaxy of all PRGs but ESO603-G21.

3.2.1 Evolutionary models and age estimate

To derive the age estimate for the polar structure and host galaxy, for all PRG in the sample, two different evolutionary models are adopted for these two components. The key input parameters, which distinguishes among different models, are the Star Formation Rate (SFR), the metallicity values and the Initial Mass Function (IMF). When the SFR and IMF are fixed, the evolutionary tracks, for each model, were derived for the following metallicity values: $Z = 0.0004$, $Z = 0.008$, $Z = 0.02$, $Z = 0.05$, $Z = 0.1$; they are assumed constant with age. In every model it has been assumed that stars form according to the Salpeter (1955) IMF, in the range from 0.1 to $125 M_{\odot}$.

Two different SFR are adopted to derive the age estimate for the host galaxy and polar ring component. A star formation history with an exponentially decreasing rate was adopted for the central host galaxy. It has the following analytical expression: $SFR(t) = \frac{1}{\tau} \exp(-t/\tau)$. The τ parameter quantifies the "time scale" when the star formation was most efficient. This expression for the SFR is usually adopted to reproduce the photometric properties of the elliptical galaxies: it is derived from the assumption that the rate with stars form is proportional to the available gas quantity (Kennicutt, 1983). In order to obtain the largest range for the age estimate, the following two values were adopted for the time scale parameter: $\tau = 1$ Gyr and $\tau = 7$ Gyr, and the correspondent evolutionary tracks were derived for each metallicity. These models are plotted in Fig. 3.3: the photometric properties of early-type galaxies are well reproduced by adopting a SFR with $\tau = 1$ Gyr. The lines of constant age were derived from the evolutionary tracks, and they are plotted in Fig. 3.3. The model with $\tau = 1$ Gyr predicts an age of about 10 Gyr for the sample of early-type galaxies by Bothun (1984); younger ages, between 1 to 3 Gyr, are predicted for the host galaxy (nucleus and outer stellar component) in all PRGs of the sample, except for AM2020, which seems to be as old as standard early-type galaxies. The model with $\tau = 7$ Gyr implies, for the sample of early-type galaxies and for the polar ring galaxy AM2020, an age older than 10 Gyr, whereas for the other PRGs of the sample even an age between 1 to 3 Gyr (Fig. 3.3).

The polar structure has, on average, bluer colors than the host galaxy (Fig.3.2) which suggests an even younger age for this component. Observations

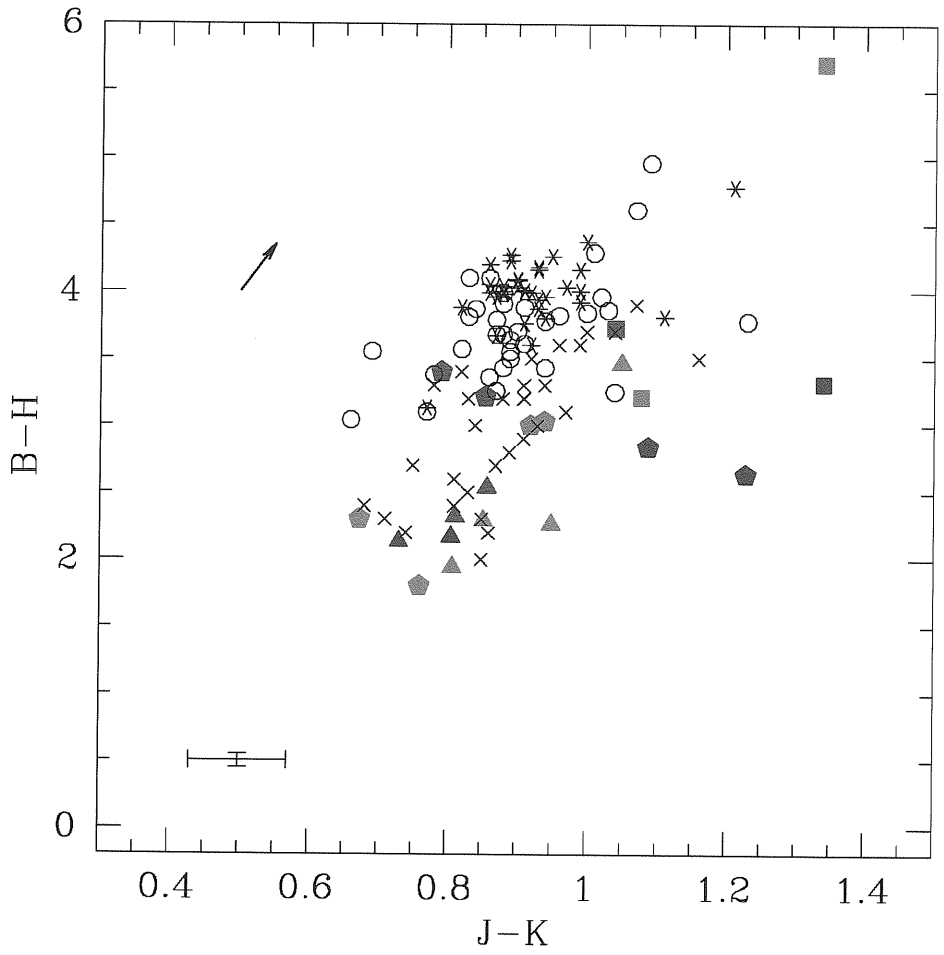

Figure 3.2: B-H vs. J-K color diagram for the five areas in each PRG of the sample, the color code for symbols is listed in Tab.3.1. Filled square indicates the central region of the host galaxy; filled pentagons indicate the stellar component outside the central region; filled triangles indicate the polar ring regions. Open circles and asterisks correspond to bulges and disks in S0 galaxies of the sample studied by Bothun (1990); crosses correspond to spiral galaxies in the sample studied by Bothun (1984). The arrow (in the top left corner) indicates the reddening vector direction for galactic dust and the screen model approximation, quoted in Sec.2.4. The average errors are shown in the bottom left corner.

suggest that could be an active star formation in polar rings, so a constant star formation model, $SFR(t) = K$ with $K \sim 10^{-10}\ M_{\odot}/yr$, (with metallicities $Z = 0.0004$, $Z = 0.008$, $Z = 0.02$, $Z = 0.05$, $Z = 0.1$) was adopted for the polar structure. For each metallicity, the correspondent evolutionary tracks were obtained, from which the lines of constant age are derived. These models, shown in Fig. 3.3, well reproduce the mean colors for a sample of spiral galaxies (Bothun et al., 1984) and implies an average age of about 5 Gyr for these objects. The integrated colors of the polar structure in all PRGs of this sample are very similar to the bluer and younger spiral galaxies, they are also clustered in the same range of metallicity, which is between $Z = 0.02$ and $Z = 0.05$, and age, which is very close to 1 Gyr.

The colors derived for both components are all upper limits, since they were not corrected for the absorption caused by the dust in the polar structure, then the true colors of the central stellar component might be even bluer. Furthermore, the age estimates for the host galaxy and the polar structure are uncertain because independent information on the star formation law and metallicity of the stellar population in the two components are not available. The intrinsic uncertainties of the synthesis population models must also be considered, particularly for the age of the host galaxy. By comparing three recent synthesis codes, Charlot, Worthey and Bressan (1996) found that the colors predicted for old populations with an age > 1 Gyr, plus same input age and metallicity, are affected by discrepancies, which are primarily due to the different prescriptions adopted for the stellar evolution theory. Thus, the age estimates given here are only indicative of the relative ages between the central host galaxy and polar structure.

3.3 Study of the host galaxy light distribution

One of the still open issues in the study of Polar Ring Galaxies is the nature of the host galaxy. A qualitative morphological inspection suggests that this component is similar to an early-type galaxy, most often an S0 (Sec.2.2). However, the NIR integrated colors, derived for the host galaxy in this work (Sec.3.1) and in previous ones (Arnaboldi et al. 1995), are on average bluer than the typical values for early-type galaxies.

The study of the surface brightness light distribution in the host galaxy may represent an "independent tool" to check whether this component is really an S0 galaxy or not, by investigating how the structural parameters compare with those of standard early-type galaxies.

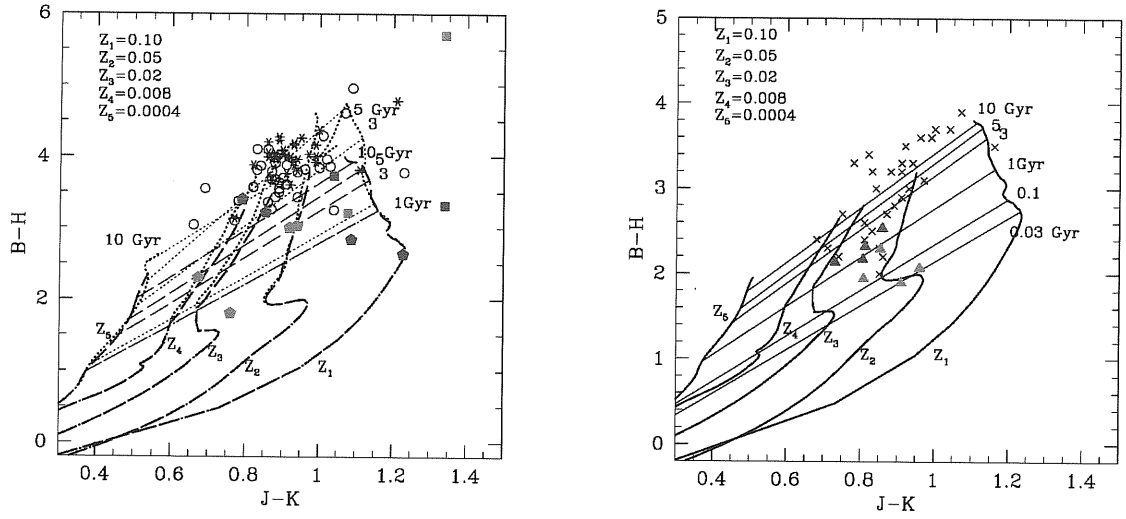

Figure 3.3: B-H vs. J-K color diagram of the evolutionary tracks for the stellar synthesis models optimized for the host galaxy (left panel) and polar ring (right panel), for each PRG of the sample, the color code for symbols is listed in Tab.3.1. Symbols are the same adopted in Fig.3.2. Left panel: the heavier dotted lines correspond to models with a characteristic timescale $\tau = 1Gyr$ and heavier dashed lines for models with $\tau = 7Gyr$. Models are computed for different metallicities as shown on this figure. Light dotted and light dashed lines indicate loci of constant age for the different models; different ages are reported on the plot. open circles and asterisks correspond to bulges and disks from a sample of S0 galaxies (Bothun, 1990). Right panel: heavier lines indicate models with constant SFR, computed for different metallicities (reported on the plot).Light lines are loci of constant age; different ages are quoted on the plot. Filled triangles indicate the polar ring regions and crosses are for a sample of spiral galaxies (Bothun et al., 1984).

The luminosity distribution of ellipticals and bulges of S0 galaxies were modeled for a long time using the $r^{1/4}$ formula (de Vaucouleurs 1948), which is characterized by two scale parameters: the effective radius r_e and the effective surface brightness μ_e of the isophote encircling half of the total light. More recently, Caon et al. (1993) showed that a generalized de Vaucouleurs formula, $r^{1/n}$, obtained by adding a free exponent n (Sersic, 1968), not only gives a better fit to the light profiles (which is expected in view of the larger number of parameters), but it also provides an interesting correlation between shape (n) and total luminosity (estimated by $L \sim I_e r_e^2$), which in turn suggests that the family of elliptical galaxies is not homologous. The main criticism of this result could be that the observed trend of n with r_e may be due to the presence of hidden disks embedded in elliptical galaxies: the larger the disk is, the smaller the value of n is found. Caon et al. (1993) had obtained their result by fitting the light profiles along the major and minor axis using just the $r^{1/n}$ law. In view of the above criticism, Iodice et al. (1997, 1999) decided to pinpoint the question by adopting a 2-Dimensional (2D) fitting procedure which allows for the presence of a disk. The study in 2D is needed in order to couple and exploit the different projection properties of the disk and bulge components, which are expected to have quite different intrinsic thickness (Kent 1985). A number of simulations on artificial galaxy models were performed in order to test the tool and to unveil the systematic effects that influence the model parameters (Iodice et al. 1997). Particular attention was given to the seeing effect: to avoid biased results caused by seeing, we have masked out the central regions[1] of the galaxy, before performing the fit. Each galaxy point in the fitting algorithm is weighted on its luminosity: brighter points are affected by smaller errors. This fitting technique is adopted here to derive the host galaxy structural parameters (Sec.3.3.1 and Sec.3.3.2), in order to compare them with those obtained for a sample of early-type galaxies (Sec.3.3.3-Sec.3.3.5).

3.3.1 Model description

The 2D fitting model is based on the super-position of up to two components, each one characterized by concentric and co-axial elliptical isophotes with constant flattening. One such component may be thought as the projection of a spheroid with finite intrinsic thickness, thus mimicking a bulge. The other component is thought to be a disk. The projected surface brightness distribution of the spheroidal component follows the generalized de Vaucouleurs

[1]The dimension of the masked area is as large as the measured PSF in that image.

law:

$$\mu_b(x,y) = \mu_e + k\left[\left(\frac{r_b}{r_e}\right)^{1/n} - 1\right] \tag{3.1}$$

with $k = 2.17n - 0.355$ and $r_b = [x^2 + y^2/q_b^2]^{1/2}$; q_b, μ_e and r_e are the *apparent axial ratio*, the *effective surface brightness* and the *effective radius* respectively. The total luminosity of this component is then $L_B = K(n)I_e r_e^2$ (Caon et al. 1993), with $K(n)$ is a function[2] of the n parameter and $I_e = 10^{-0.4\mu_e}$.

The projected surface brightness distribution of the disk is supposed to follow an exponential behavior, as described by Freeman's exponential law (1970):

$$\mu_d(x,y) = \mu_0 + 1.086\left(\frac{r_d}{r_h}\right) \tag{3.2}$$

with $r_d = [x^2 + y^2/q_d^2]^{1/2}$; q_d μ_0 and r_h are the *apparent axial ratio*, *the central surface brightness* and the *scalelength* of the disk, respectively. The central surface brightness corrected for the inclination of the disk with respect to the line of sight is given by $\mu_0^c = \mu_0 - 2.5\log(q_d)$, and the total luminosity for this component is $L_D = 2\pi I_0 r_h^2$, with $I_0 = 10^{-0.4\mu_0^c}$ (Freeman, 1970).

The total *Bulge to Disk ratio (B/D)* is given by the ratio between the total luminosities of the bulge and disk components ($B/D = L_B/L_D$)

3.3.2 Results of the 2D modeling

For all PRGs of the sample, the 2D model of the host galaxy light distribution is performed in the Kn band, because the dust absorption is weaker in this band. For the polar ring galaxy A0136-0801 only the H band data were available, so the study of the light distribution for this object is only done in this band. For all PRGs of the sample but AM2020-504, the adopted model for the host galaxy light distribution is made by the super-position of a bulge and disk component, as described in Sec.3.3.1. Since the host galaxy morphology in AM2020-504 seems to be more similar to that of an elliptical rather than an S0 galaxy (see Sec.2.2), its light distribution was fitted with a one-component model, given by the generalized de Vaucouleurs law. The regions affected by foreground stars and by the polar ring light are accurately masked before performing the fit to the light distribution. Then the models for the host galaxy in the J and H bands are simply scaled versions of the Kn band model, based on the average colors of this component (see Sec.2.3). The structural parameters derived for

[2] $\log[K(n)] = 0.03[\log(n)]^2 + 0.441\log(n) + 1.079$

each object (Sec.3.3.1), and the relative error estimated by the fit algorithm, are listed in Tab. 3.2. In the last line of Tab. 3.2 we reported the $\tilde{\chi}^2$ for each fit: values for $\tilde{\chi}^2 \leq 2$ represent good fits (as described by Schombert & Bothun 1987).

In ESO 603-G21 and ARP 230 the ring radius is not enough extended to be well distinguishable from of the host galaxy, so the light from the two component is mixed (see Fig.2.2 and Fig.2.3, bottom left panels): this is the reason why the structural parameters, in particular the apparent axial ratios, in the model for these two objects, are affected by larger errors than for the other polar ring galaxy in the sample. Fig. 3.4 and Fig. 3.5 show the comparison between the observed surface brightness profiles and those derived by the fit, along the principal axis of the host galaxy, in each PRGs. In the regions where the galaxy light dominates ($R \leq 20$ arcsec), the modeled surface brightness distribution differs from the observed one by about 0.2 magnitude at least, and by about 0.5 magnitude in the outer regions.

Fig. 3.6 and Fig. 3.7 show the ratio between the whole galaxy image and the host galaxy model, which is computed in the H band[3], for each PRG. The regions perturbed by dust absorption, due to the ring component, are characterized by values less than 1. Furthermore, in these images the polar ring structure stands out very well and also some peculiar luminous features related to the galaxy, like the outer shells in ARP 230 (Fig. 3.6 bottom panels).

In the following Sections, we wish to discuss the structural parameters, which characterized the light distribution of the host galaxy in each polar ring galaxy of the sample, and compare them with the typical values for early-type galaxies.

3.3.3 Bulge effective parameters: μ_e - $\log r_e$ plane

Fig. 3.8 plots the location of bulges of PRGs in the plane of effective parameters μ_e and r_e. The sample of early-type galaxies, chosen for the comparison, has been studied by Bothun and Gregg (in 1990). The structural parameters for these objects where obtained, in the B band, by fitting the light distribution with the super-position of a de Vaucouleurs' law ($n = 4$) and an exponential disk, for the bulge and disk component respectively. The surface brightness parameters in the K band are derived by taking into account the average B-K color of these objects (Bothun and Gregg, 1990).

[3]This ratio is showed in the H band, instead of Kn band, in order to easily compare the residuals derived by the 2D fit of the host galaxy light distribution with those that stand out by the unsharp-mask (Sec.2.2).

Table 3.2: Structural parameters for the host galaxy in five PRGs of the sample. The effective surface brightness μ_e and the central surface brightness μ_0 are in $mag/arcsec^2$; μ_0^c is the central surface brightness corrected for the inclination; r_e and r_h are respectively the effective radius and disk scalelength derived in arcsec, the corresponding values expressed in kpc are derived by using $H_0 = 70$km s^{-1} Mpc^{-1}.

Parameter	A0136-0801	ESO 415-G26	ARP 230	AM 2020-504	ESO 603-G21
μ_e	16.26 ± 0.04	14.72 ± 0.11	16.3 ± 0.2	16.61 ± 0.08	15.50 ± 0.09
r_e (arcsec)	1.27 ± 0.02	1.68 ± 0.07	1.7 ± 0.2	4.8 ± 0.2	1.35 ± 0.08
r_e (kpc)	0.49 ± 0.01	0.54 ± 0.02	0.20 ± 0.02	1.66 ± 0.07	0.29 ± 0.02
q_b	0.899 ± 0.005	0.80 ± 0.012	0.7 ± 0.5	0.75 ± 0.01	0.8 ± 0.4
n	0.59 ± 0.03	0.72 ± 0.06	0.6 ± 0.2	2.36 ± 0.15	0.53 ± 0.14
μ_0	15.34 ± 0.03	15.08 ± 0.02	15.06 ± 0.11		15.67 ± 0.15
μ_0^c	15.82 ± 0.04	16.30 ± 0.03	15.6 ± 0.9		15.9 ± 0.9
r_h (arcsec)	2.56 ± 0.03	5.41 ± 0.04	3.7 ± 0.2		3.1 ± 0.2
r_h (kpc)	0.98 ± 0.01	1.73 ± 0.01	0.45 ± 0.02		0.67 ± 0.04
q_d	0.64 ± 0.007	0.32 ± 0.003	0.6 ± 0.4		0.7 ± 0.5
B/D	0.25 ± 0.01	0.7 ± 0.4	0.15 ± 0.14		0.4 ± 0.2
$\tilde{\chi^2}$	1.4	1.3	1.5	1.1	1.6

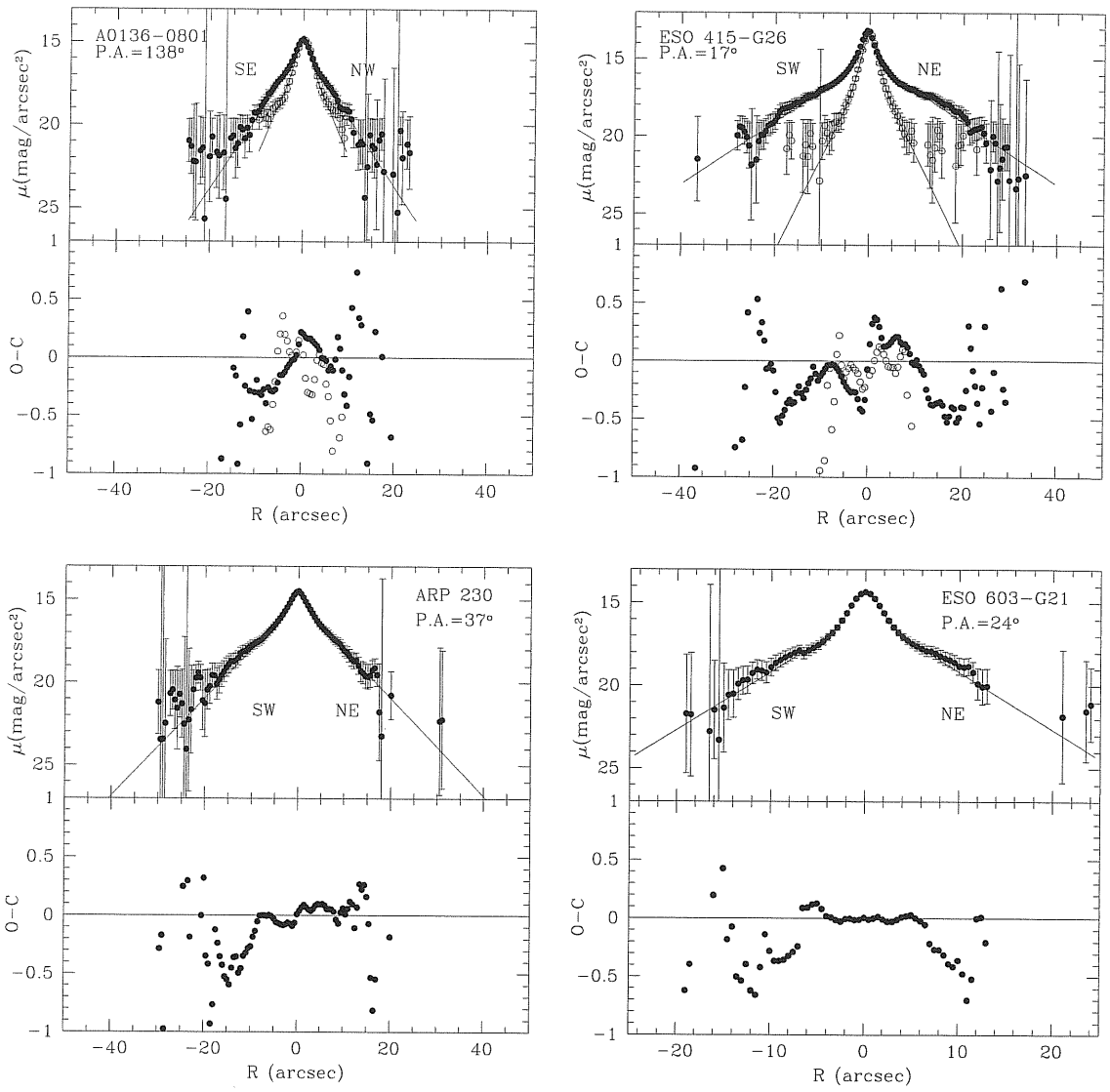

Figure 3.4: 2D fit of the host galaxy light distribution by adopting the two-component model (bulge+disk), described in Sec.3.3.2. The observed light profiles along the major (filled dots) and minor axis (open dots) are compared with those derived by the fit (continuous line), which are performed in the Kn bands for ESO 415-G26, ARP 230, ESO 603-G21 and in the H band for A0136-0801. For ARP 230 and ESO 603-G21 the luminosity profile is that along the direction orthogonal to the polar ring. The orientation and P.A., reported on each panels, refer to the major axis.

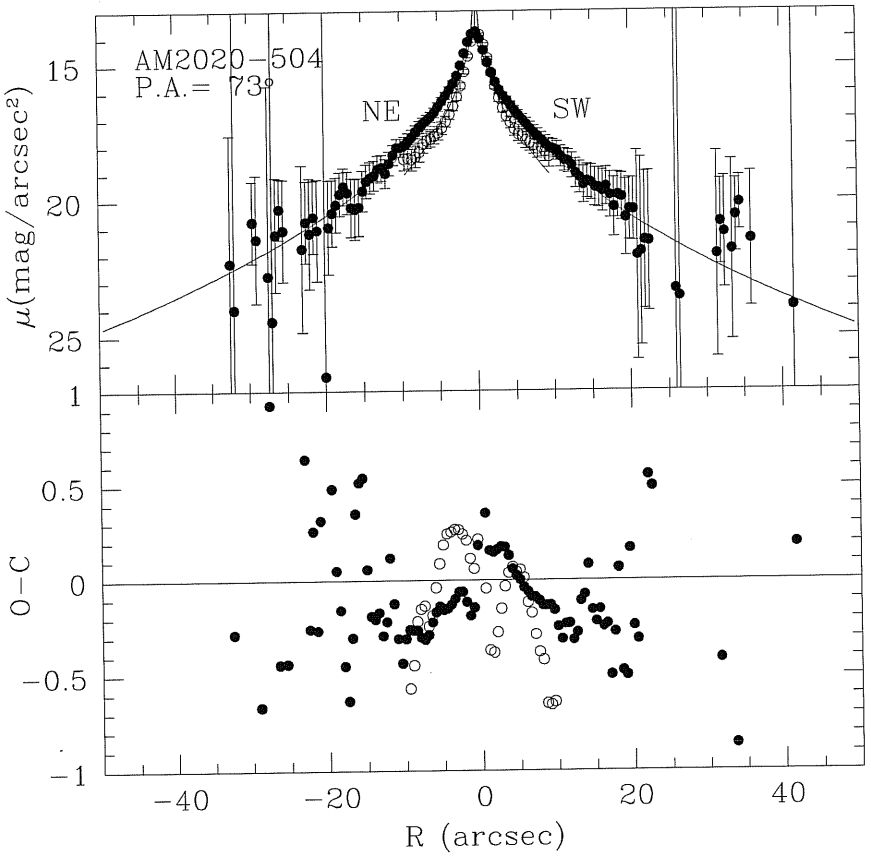

Figure 3.5: 2D fit of the host galaxy light distribution for the polar ring galaxy AM 2020-504. For this object a one-component model, as described in Sec.3.3.2, was adopted. The observed light profiles along the major (filled dots) and minor axis (open dots), in the Kn band, are compared with those derived by the fit. The orientation and P.A., reported on figure, refer to the major axis.

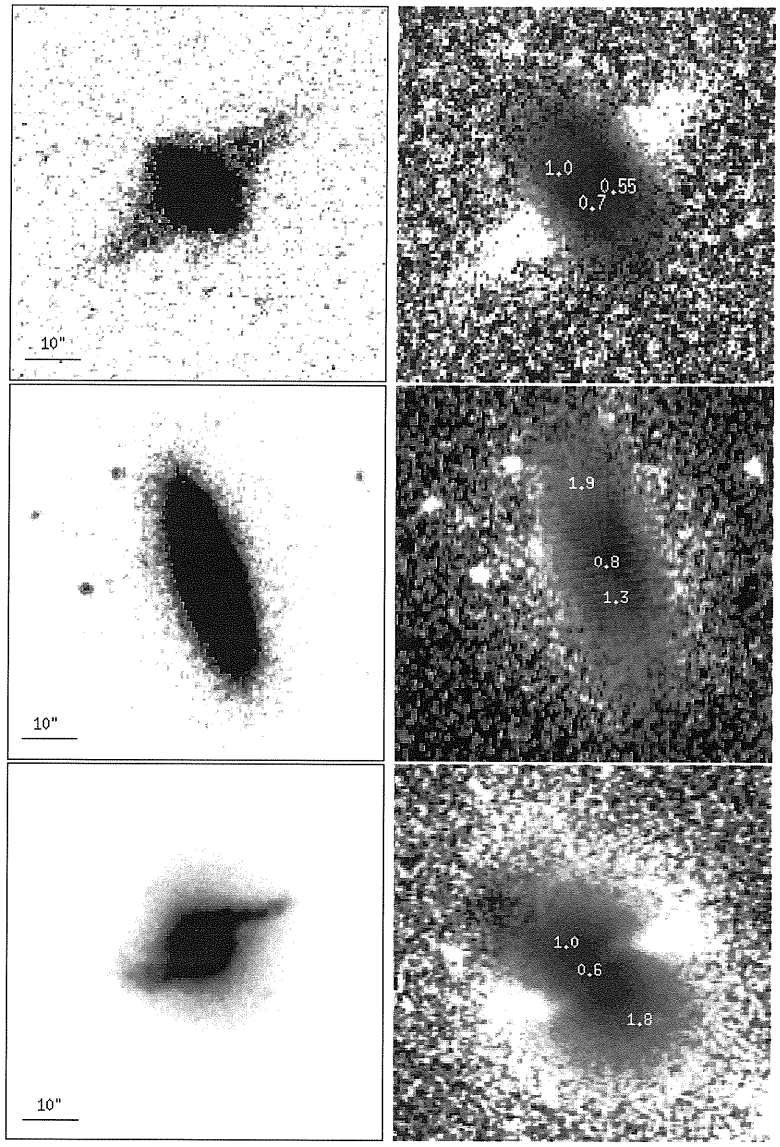

Figure 3.6: H band images (left panels) and image ratio between the whole galaxy image and the host galaxy model, in this band, (right panels) for A0136-0801 (top panels), ESO415-G26 (middle panels) and ARP230 (bottom panels). Numbers on the left panels indicate the value of the ratio in that isophote. Lighter points correspond to those regions where the galaxy is brighter than model. Units are intensity; North is up and East is to the left.

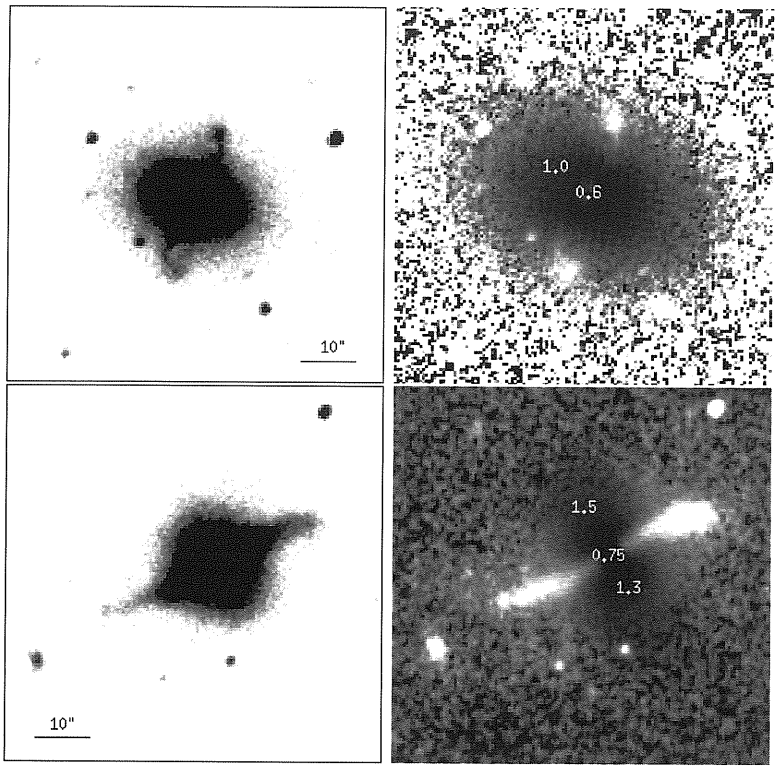

Figure 3.7: H band images (left panels) and image ratio between the whole galaxy image and the host galaxy model, in this band, (right panels) for AM2020-504 (top panels), and ESO603-G21 (bottom panels). Numbers on the left panels indicate the value of the image-to-model ratio in that isophote. Lighter points correspond to those regions where the galaxy is brighter than model. Units are intensity; North is up and East is to the left.

The host galaxy seems to be characterized by a more "compact" bulge respect to normal early-type galaxies, in all PRGs of the sample but AM 2020-504 which has larger values of μ_e and r_e. In 1994 Reshetnikov et al. found a similar behavior for the bulges of same polar ring galaxies in the B band: they suggested that this displacement could be due to a possible under-estimation of the luminosities and sizes of bulges by the projection of the polar ring on the central regions of the galaxy. Therefore, they concluded that, on average, the PRGs bulges have the same characteristics of normal early-type galaxies, in the μ_e - $\log r_e$ plane. The 2D bulge-disk decomposition adopted here (Sec.3.3.1) let us to minimize the perturbations due to the ring and to conclude that, in the μ_e - $\log r_e$ plane, the bulge component of the host galaxy in PRGs resembles the smallest early-type galaxies with the higher surface brightness.

3.3.4 Bulge scale parameters: $\log n$ - $\log r_e$ plane

The optical light distribution in the host galaxy central regions has a quasi-exponential behavior, as suggested by the small values of the n exponent (close to 1), in all PRGs of the sample, except for AM2020-504 (Tab. 3.2). These values, however, must be considered as lower limits: we have found that the light in PRG bulges is very concentrated toward the center, so the convolution of such light distribution with the PSF may have caused a smoothing of the light profiles toward the center, leading to a spuriously smaller value for the n exponent. By the light of these new results, a new 2D fitting technique, which takes into account the deconvolution algorithm, needs to be developed to study the PRGs light distribution. Fig. 3.9 shows the comparison of the scale parameters, n and r_e, for the bulge component in PRGs, for a sample of early-type galaxies in the Virgo cluster (Caon et al., 1993) and for a sample of early type galaxies of low surface brightness galaxies[4] in Fornax cluster (Davies et al., 1988). In this plane PRGs occupy the region where lower values for both parameters are found. In this region, where the dwarf galaxies are also found, they seem to "follow" the relation between the n exponent and the effective radius, found by Caon et al. (1993), for which n increases steadily with r_e. The polar ring galaxy AM2020-504 is the only object of the sample which falls in the same regions occupied by "ordinary family"[5] of early-type galaxies.

[4]Davies et al. (1988) fitted the B band light profiles by adopted the generalized de Vaucouleurs law in the form $I(r) = I_0 exp[-(r/A)^N]$, so we have calculated the effective radius r_e and the exponent n from the scalelenght radius A and the exponent N.

[5]According to Capaccioli et al. (1992), the early-type galaxies could be divided into two groups, which are characterized by different properties: the *ordinary* family (with $r_e < 3$

3.3.5 Disk structural parameters: μ_0 - $\log r_h$ plane

The average value of the central surface brightness (corrected for the inclination, Sec.3.3.1), for this sample of PRGs, is $< \mu_0^c >= 15.9 \pm 0.3\ mag/arcsec^2$. This value is significantly brighter than the average value[6], for the sample of S0 galaxies studied by Bothun and Gregg (1990), which is about $< \mu_0^c >= 17.97$ mag arcsec^{-2}. The average scalelength of the disks in the host galaxy is $< r_h >= 1.0 \pm 0.6$ kpc, whereas the average value for this sample of S0 galaxies is about $< r_h >= 2.1$ kpc. Disks in the host galaxy of PRGs are brighter and smaller than the disks in S0 galaxies: this stands out clearly in Fig. 3.10, which plots the location of the PRGs and S0 disks parameters (Sec.3.3.1) in the μ_0^c - $\log r_h$ plane. The *Bulge-to-Disk ratio (B/D)* for the host galaxy in PRGs of our sample falls in the range of values typical for disk-dominated S0 galaxies, as shown in Fig. 3.11.

3.4 Study of the light distribution in the polar structure

An important quantity related to the size of the polar ring is the moment of its radial distribution

$$(\Delta R)^2 = \frac{\int_{r_{min}}^{\infty} (r - \bar{R})^2 \mu(r) dr}{\int_{r_{min}}^{\infty} \mu(r) dr} \tag{3.3}$$

where $\bar{R}$ is the average radius, weighted by the surface brightness distribution, given by

$$\bar{R} = \frac{\int_{r_{min}}^{\infty} r \mu(r) dr}{\int_{r_{min}}^{\infty} \mu(r) dr} \tag{3.4}$$

r_{min} is equal to 3 times the effective radius of the central component.

For a pure exponential disk, the $\Delta R/\bar{R}$ ratio tends to unity when r tends to infinity. For a real object, this value is expected to be less than 1, because of its finite extension. This is confirmed by the $\Delta R/\bar{R}$ values derived for a sample of spiral galaxies (de Jong 1996) in the B band: this quantity varies from 45% to 75% and the average value is $\Delta R/\bar{R} \sim 65\%$.

kpc) and *bright* family (with $r_e > 3$ kpc).

[6]This value, relative to the K band, has been derived by that obtained in the B band, taking into account the average B-K colors (Bothun and Gregg, 1990) for these galaxies.

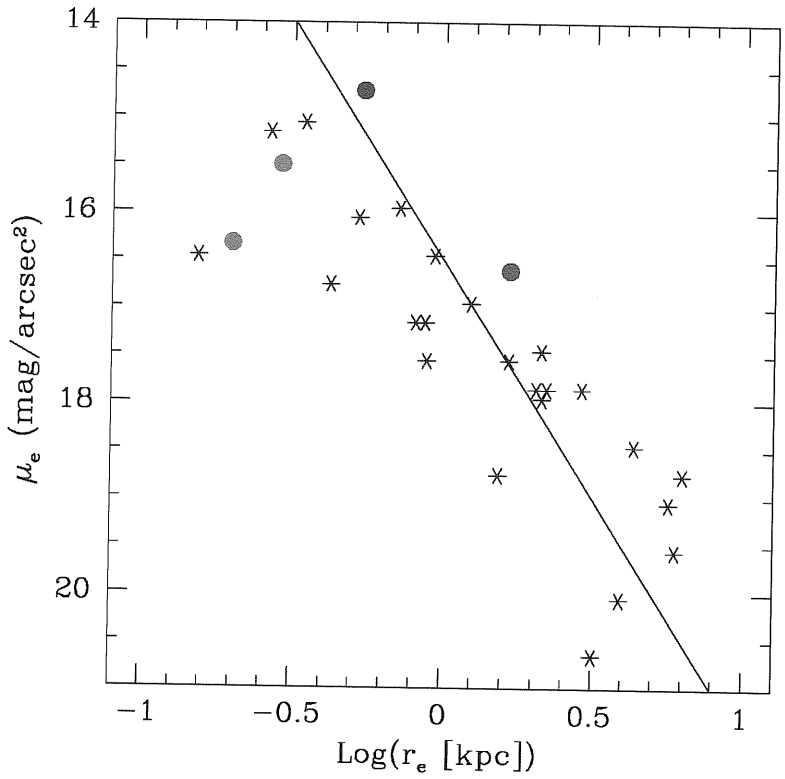

Figure 3.8: Relation between the bulge effective parameters (Sec.3.3.1) for the PRGs of the sample: AM2020-504 (red point), ESO 603-G21 (green point), ARP230 (light blue point), ESO 415-G26 (pink point) and A0136-0801 (yellow point). They are compared with the typical values for early-type galaxies (Bothun and Gregg, 1990). The solid line is a line of constant bulge luminosity derived for $\mu_e = 18\ mag/arcsec^2$, $r_e = 2$ kpc and $n = 4$.

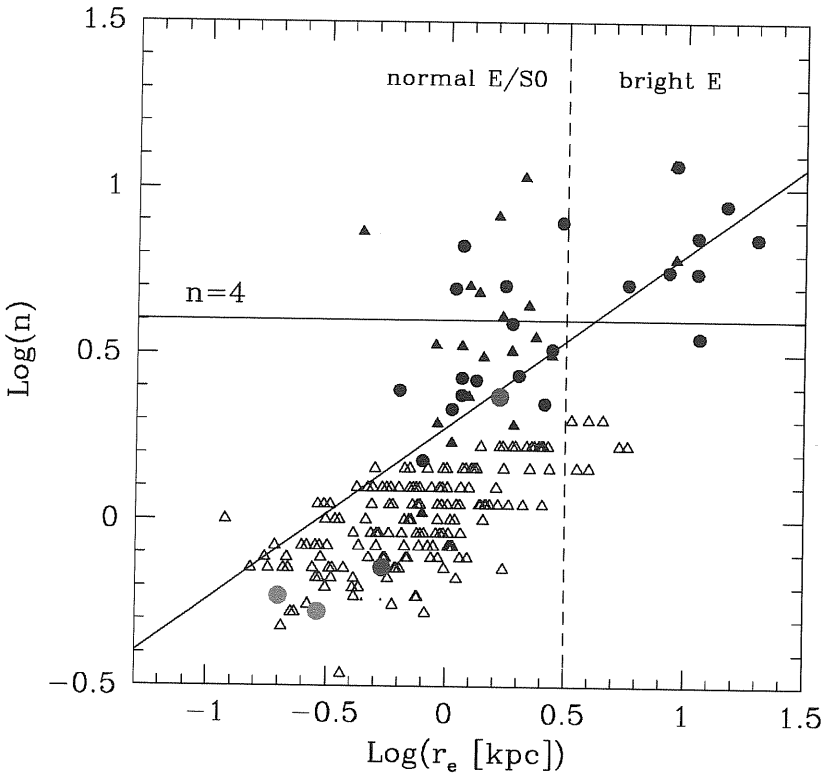

Figure 3.9: Relation between the effective radius r_e and the n exponent of the generalized de Vaucouleurs' law (Sec.3.3.1), for the bulge component in the PRGs of the sample: AM2020-504 (red point), ESO 603-G21 (green point), ARP230 (light blue point), ESO 415-G26 (pink point) and A0136-0801 (yellow point). They are compared with the typical values for 1) early-type galaxies, Ellipticals (black circles) and S0s (black triangles), by Caon et al. (1993); and for 2) LSB galaxies (open triangles), by Davies et al. (1988). The plotted n exponents values for the early-type galaxies are those derived by Caon et al. (1993) along the minor axis of the system, in order to exclude the contribution from a possible disk component. The solid line is the relation between n and r_e derived by Caon et al. (1993): $\log n = 0.28 + 0.52 \log r_e$.

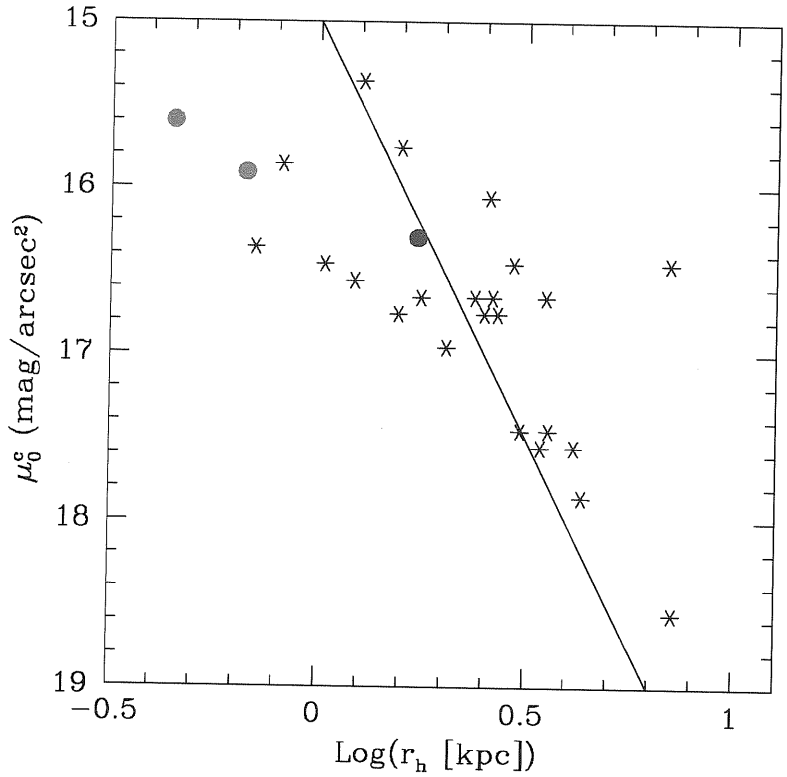

Figure 3.10: Relation between the central surface brightness, corrected for the inclination, and the scalelength of the disk component in the host galaxy (Sec.3.3.1) for the PRGs of the sample: ESO 603-G21 (green point), ARP230 (light blue point), ESO 415-G26 (pink point) and A0136-0801 (yellow point). They are compared with the typical values for early-type galaxies (by Bothun and Gregg, 1990). The solid line is a line of constant disk luminosity, derived for $\mu_0^c = 18\ mag/arcsec^2$ and $r_h = 1.6$ kpc.

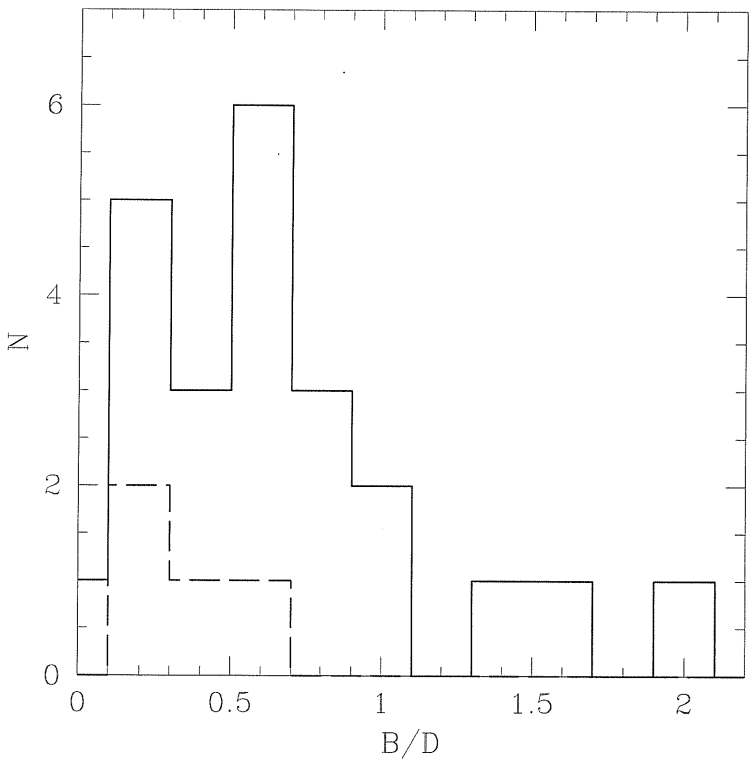

Figure 3.11: B/D distribution for the PRGs of the sample (dashed line) and for early-type galaxies, by Bothun and Gregg (1990), (solid line).

Table 3.3: $\Delta R/\bar{R}$ ratio for polar ring galaxies of the sample.

Object	$\Delta R/\bar{R}$ %
A0136-0801	45
ESO 415-G26	47
ARP 230	35
AM 2020-504	16
ESO 603-G21	39

The $\Delta R/\bar{R}$ is a key parameter in the studies about polar ring stability (Sec.1.1). In order to derive this quantity for every polar ring galaxy in the sample, a folded light profile was computed in the K band, for each object, from the surface brightness profiles extracted along the ring major axis (Fig. 2.4 and Fig. 2.5). For the polar ring galaxy ESO415-G26 the average ring profile has been obtained in the B band, where this component is significantly brighter than in the K band (see Fig.2.1, top left panel). In Fig. 3.12 and in Fig. 3.13 the average ring light profiles are plotted for each object. Tab.3.3 lists the $\Delta R/\bar{R}$ ratio derived for each polar ring galaxy in the sample: this value could be considered as a lower limit, since the polar ring light coming from regions closer to the host galaxy were not included in the computation. In Fig. 3.14 these values are compared with the typical $\Delta R/\bar{R}$ ratio for annuli in a quasi-equilibrium configuration, derived by Katz and Rix (1992) from hydrodynamical simulations to study polar ring stability (see Sec.1.1): all PRGs in this sample, but AM2020-504, seems to be outside this range, with larger $\Delta R/\bar{R}$ ratio.

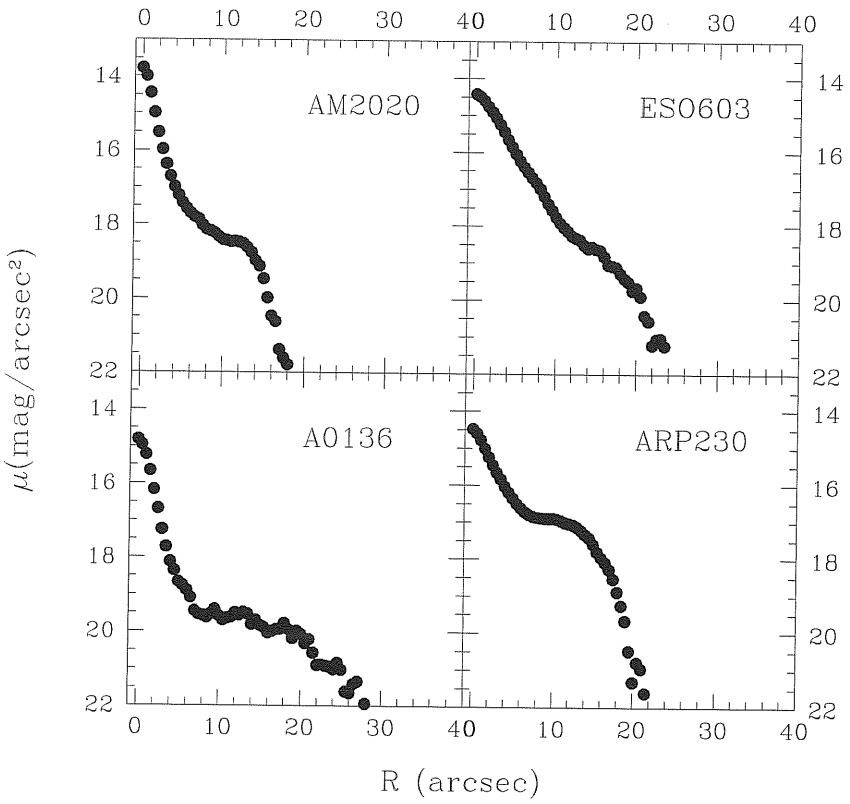

Figure 3.12: Average surface brightness profiles for the polar ring in AM2020-504, ESO 603-G21 and ARP 230 in the Kn band, and in A0136-0801 in the H band.

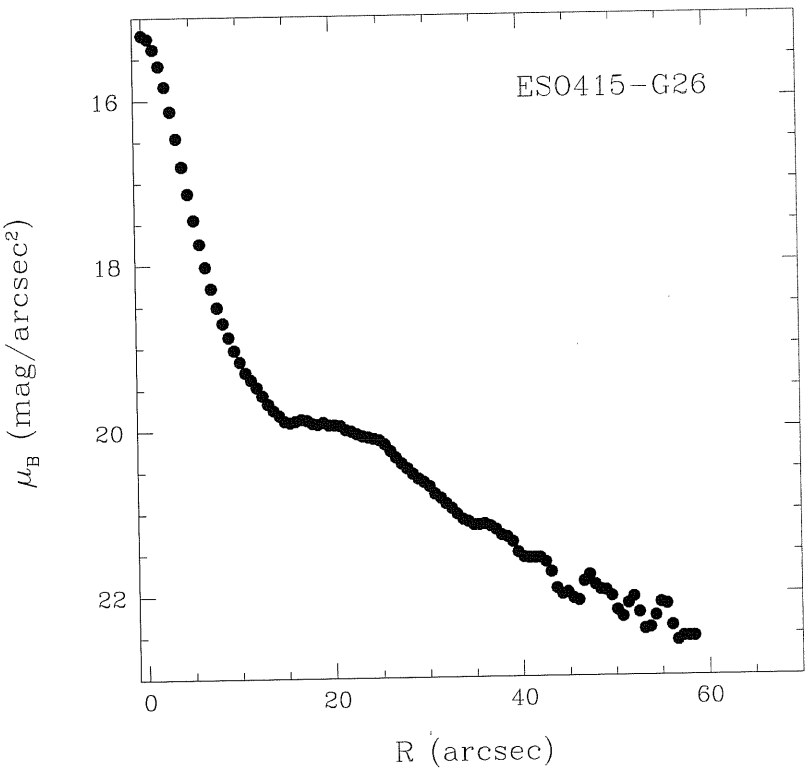

Figure 3.13: Average surface brightness profiles for the polar ring in ESO 415-G26 in the B band.

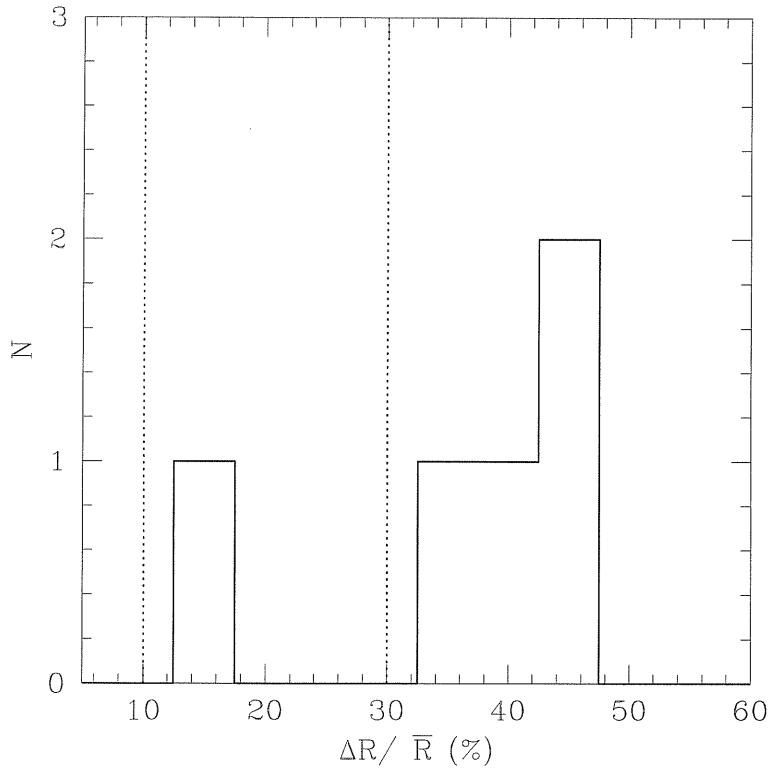

Figure 3.14: Distribution of the $\Delta R/\bar{R}$ ratio derived for each polar ring galaxy in the sample. The dotted lines limit the range of $\Delta R/\bar{R}$ ratio for annuli in a quasi-equilibrium configuration, formed in the accretion/merging scenario (Sec.1.1).

3.5 Description and discussion of each galaxy

Here we give a detailed description on the main properties of each selected polar ring galaxy presented in this Chapter. In particular, we discuss in detail about the relevant features which characterized the light and color distribution for each object.

A0136-0801 - This is one of the best known case of kinematically confirmed polar ring galaxy (Schweizer et al. 1983; Whitmore et al. 1990, PRC): it is characterized by a wide polar structure, which is three times more extended than the equatorial radius of the central host galaxy. The surface brightness profile in the H band (see Fig.2.4) along ring major axis looks like two exponential segments with different slopes: the light inside $10''$ from the center is associated to the host galaxy, whereas the ring component is extended out $40''$. Both the H band image and luminosity profiles (Fig.2.2 and Fig.2.4, top panels) show that the polar ring is less luminous than the central galaxy, and the bulk of H band light is concentrated at smaller radii. The high-frequency residual image (Fig.2.2), in the H band, shows the presence of a nearly edge-on disk in the central host galaxy. This object was mapped in HI with the *Very Large Array (VLA)* by Cox et al. (1995) and van Gorkom et al. (1987): all HI emission is found to be associated with the polar ring, whose outer HI contours appear to warp away from the poles. The total HI mass estimated for this object is about $1.6 \times 10^9 M_\odot$ (Cox et al. 1995). The regular HI distribution and optical appearance, an apparent lack of HII regions and other signs of recent star-formation activity (Mould et al. 1982) suggest that the polar structure is quite old and possibly dynamically stable.

ESO 415-G26 - This is a well-known and long-studied polar ring galaxy, also known as MCG-5-7-1. Unlike A0136-0801, the polar ring is less extended than the central host galaxy, in the optical band (see Fig.2.1, top left panel). Deeper exposures show extensive debris at a position angle intermediate between those of the host galaxy and ring, and also show shells and loops in the outer regions (Whitmore et al. 1987). In the NIR bands (Fig.2.2, middle panels, and Fig.B.1) the polar ring is so faint that it is almost undetectable. The central host galaxy is the dominant luminous component, in these bands: morphological inspection and the analysis of the light distribution show that this is a nearly edge-on S0 galaxy with an exponential bulge. Among the PRGs presented in this Chapter, ESO 415-G26 is characterized by the higher B/D ratio (see Tab.3.2). The NIR color maps (Fig.2.6, top panels) and J-H vs. H-K colors in different regions of host galaxy and ring (see Sec.2.4 and Fig.3.1)

show that the nucleus of the system is characterized by the reddest color and that the polar ring is much bluer than the central host galaxy. HI map for this object were obtained, with the VLA, by van Gorkom et al. in 1987 and by van Gorkom & Schiminovich in 1997. They noted that the neutral hydrogen lies along the major axis of the polar ring, with some degrees of correlation between the HI and the outer shells (van Gorkom & Schiminovich 1997). The most accurate estimate of the total HI mass is about $5.6 \times 10^9 M_\odot$ (Schiminovich et al. 1997). This object is characterized by a considerable amount of molecular hydrogen: Galletta, Sage and Sparke (1997) have estimated the total H_2 mass of about $2.4 \times 10^9 M_\odot$.

ARP 230 - This object, also known as IC 51, was studied by Wilkinson et al. (1987) as a well example of *shell elliptical* galaxies: in the NE and SW directions, outer shells are clearly visible (Hernquist and Quinn 1988), which are more luminous in the B band (Fig.2.1, top right panel) than in the NIR ones (Fig.2.2, bottom panels and Fig.B.2). It is also classified as a PRG because it has a fast rotating disk-like structure, made up by gas, stars and dust, perpendicular to the apparent major axis of the central galaxy, $P.A. = 37°$, (Mollenhoff et al. 1992). Both B band (Fig.2.1, top right panel) and NIR images (Fig.2.2, bottom panels and Fig.B.2) of this polar ring galaxy show that the ring-like component, along SE and NW directions, has about the size of the inner galaxy, and it has a very well-defined outer edge, where dust absorption is present. The high-frequency residual images (Fig.2.2 and Fig.B.2, right panels), show a very distorted structure for the ring component: to about $10''$ from the center it seems strongly warped, to which absorption features are associated. An elongated structure, which is nearly orthogonal to the ring, suggests that the central host galaxy seems to be more similar to a disk galaxy, an S0, than an elliptical galaxy. However, since the polar ring and host galaxy have the same size, it is very difficult to distinguish the morphology of the central component. The 2D model of the light distribution for this component also suggests that it may be an S0 galaxy with an exponential bulge (Tab.3.2), but the peculiar ring structure produce a very uncertain estimate of all structural parameters, in particular the apparent axial ratios are also influenced by the presence of the outer shells. In the image ratio between the whole galaxy and the 2D model of the central component the bright edges of the ring (in the NW and SE directions) and outer shells stand out very clear as luminous residual structures (Fig.3.6, lower left panel). The central host galaxy shows similar J-H colors to the polar ring component, and bluer H-K colors (Fig.3.1). The very red colors of the nucleus of the system are reasonably

due to dust absorption in the ring, which pass just in front it. This object was mapped in HI with VLA by Schiminovich et al. (1997), they found that the neutral hydrogen is all associated to the ring and it shows global rotation along this component. They estimated a total HI mass of about $2.3 \times 10^9 M_\odot$. This PRG was mapped by Cox (1996) in the radio continuum, at 20 cm and 6 cm, with the VLA: she found an extended emission aligned with the ring structure and additional filaments which are extended well above the plane of the ring. By comparing the radio continuum and the far-infrared (FIR) emission, detected for this object at $60\mu m$ and $100\mu m$ (Moshir et al. 1990, the IRAS Faint-Source Catalog), Cox (1996) deduced that this PRG falls on the radio/FIR correlation for star-forming galaxies.

AM 2020-504 - Previous photometric and spectroscopic observations have shown that the central host galaxy in this object is very similar to an elliptical galaxy, which is characterized by a decoupled rapidly rotating core, inside about 3″ from the center, (Whitmore et al. 1987; Arnaboldi et al. 1993a, 1995). The rotation curve of the gas in the polar ring has a constant gradient in the inner regions, inside 10″ from the center, and beyond this distance it becomes flat or slightly rising (Arnaboldi et al. 1993a). The UV spectrum of this object is very similar to that of a starburst galaxy (Arnaboldi et al. 1993b). The narrow polar ring, which is observed along the host galaxy minor axis, is brighter in the B band (Fig.2.1, bottom left panel) than in the NIR images (Fig.B.3). In all bands, the light distribution of this component reaches a maximum between 10″ and 15″ (see Fig.2.5). As pointed out in the previous Sections, this is the only object of the sample which shows different properties respect to the other polar ring galaxies studied here. In high-frequency residual images (Fig.2.3, top right panel, and Fig.B.3, left panels) there is no trace of any disk-like structure associated with the host galaxy major axis, which is observed, on the contrary, in all polar ring galaxies studied here. This is the only polar ring system in our sample whose J-H and H-K colors do fall inside the area occupied by the early-type galaxies (Fig.3.1). Moreover, respect to the other PRGs of our sample, in AM 2020-504 the stellar population of the host galaxy is older, while the ring component seems to be as old as the other polar rings in this sample. The absence of disk in the host galaxy suggested us to use a generalized de Vaucouleurs' law only (Eq.3.1) for the 2D fit of the light distribution in this component: we found that, among all PRGs of our sample, the structural parameters for the host galaxy in AM 2020-504 fall in the same range of values where normal elliptical galaxies are found. All these results suggest that AM 2020-504 may be the only polar ring system in our

sample where the inner component is more likely an elliptical rather than an S0 galaxy.

ESO 603-G21 - The prominent structure which appears in the B band image of this object (Fig.2.1, bottom right panel) is the apparently warped dusty ring (in the SE and NW directions) which surrounds a bright round stellar system (Whitmore et al. 1990). This central component is much fainter in the NIR images (Fig.2.3 and Fig.B.4, left panels) and it is embedded in a very luminous disk-like structure. The high-frequency residual images (Fig.2.3 and Fig.B.4, right panels) reveal that this disk is nearly edge-on and warped in the outer regions. A further fainter "filamentary" structure is visible perpendicular to this disk, which is aligned with the apparent major axis of the central spheroid ($P.A. = 24^o$) and its radius is less than $10''$. Arnaboldi et al. (1995), when detected this feature, suggested that it may indicate the presence of the "true" polar ring. The surface brightness profiles along the bright edge-on disk have an exponential behavior (see Fig.2.5, bottom right panel) and the comparison with the surface brightness profiles along the orthogonal direction shows that this disk is the dominant luminous component in the NIR bands. The reddest regions in the NIR color maps (Fig.2.6) correspond to this disk component, while the central spheroid is bluer. In the J-H vs. H-K color diagram, ESO 603-G21 is the polar ring galaxy with the reddest colors for the nuclear regions, which are similar to the typical colors of Seyfert galaxies. The spectroscopic data for this object are a puzzle and also quite uncertain (Arnaboldi et al. 1995): they seems to show rotation of the stellar component along the two axis corresponding to $P.A. = 24^o$ and $P.A. = 114^o$, which may suggests that the underlying central spheroid is triaxial. The rotation curve derived by the strong $H\alpha$ emission seen in the ring spectrum shows a constant velocity gradient along this component (Arnaboldi et al. 1995). Radio data for this object shows CO emission corresponding to $1.1 \times 10^9 M_\odot$ of molecular hydrogen (Galletta, Sage and Sparke 1997) and $6.2 \times 10^9 M_\odot$ in HI (van Driel et al. 2000). Radio continuum emission was detected for this object by Cox (1996) in the central regions of the candidate polar ring (i.e. along $P.A. = 114^o$, as in the PRC). FIR emission, at $60\mu m$ and $100\mu m$, was detected for this PRG (Moshir et al. 1990, the IRAS Faint-Source Catalog), and as ARP 230, also this object falls on the radio/FIR correlation for star-forming galaxies rather than for an AGN (Cox 1996).

3.6 Summary

Here we summarize the main observational properties found for the PRGs studied in this Chapter. The analysis of the light and color distribution for the host galaxy and polar structure have shown that:

1. in all PRGs except for AM 2020-504, the **host galaxy** differs from a "standard" S0 galaxy, it is bluer and younger than normal early-type galaxies, and, respect to S0 galaxies, it is characterized by a more "compact", nearly exponential, bulge and by a brighter and smaller disk;

2. the **polar structure**, in all PRGs, is bluer than the host galaxy and has colors similar to those of dwarfs and spiral galaxies;

3. in all PRGs except for AM 2020-504, the ratio between the radial extension (ΔR) of the polar structure and its mean radius ($\bar{R}$) varies from 35% to 50%.

4. AM 2020-504 seems to be the only polar ring system in our sample where the host galaxy is very similar to an elliptical galaxy, and where the polar structure is characterized by the smaller $\Delta R/\bar{R}$ ($\sim 10\%$) ratio;

5. almost all PRGs studied here are characterized by a large amount of HI gas, always associated to the polar structure, larger than the typical gas content in early-type galaxies;

6. in all PRGs, except for AM 2020-504, the total baryonic mass (gas plus stars) in the polar structure is higher than the total luminous mass in the host galaxy (see Tab.3.4).

Table 3.4: Mass of the stellar component in the host galaxy (second column) and the total baryonic mass in the polar structure (third column), which includes the mass of the stellar component and the mass of the gas in the form of neutral (HI) and molecular hydrogen (H2).

Object	M_{star} (HG) $10^9 M_\odot$	$M_{gas} + M_{star}$ (PR) $10^9 M_\odot$
ESO 415-G26	9	10
ARP 230	2	5
AM 2020-504	6	5
ESO 603-G21	2	10

Chapter 4

ESO 235-G58: barred galaxy or polar ring?

The southern galaxy ESO 235-G58 was classified as a late-type barred spiral on the ESO/SRC-J Sky Survey. It is characterized by a particular elongated bar-like structure, for which the total extension is about 40″ and the P.A. of its major axis is 106°. It is encircled by a weak outer pseudoring and two faint outer arms, which reach a distance of about 1′ from the center (Fig.4.1). By fitting the inner isophotes of the central galaxy and the outer ones, relative to the ring, Buta & Crocker (1993) estimated the inclination angle between the major axis of the two components to be about 40°. The object is part of a group of nine galaxies (Maia et al. 1989), whose mean radial velocity is 4662 km s^{-2} (by Buta & Crocker, 1993). Using $H_0 = 70$ km s^{-1} Mpc^{-1}, we derive a distance of about 67 Mpc. Two prominent spiral galaxies (classified as Sbc) lie near to ESO 235-G58: the large edge-on spiral ESO 235-G57 (see bottom of Fig.4.1) and the large face-on spiral ESO 235-G55. ESO 235-G58 is among the faintest member of the group ($M_B = -19.1$) and it seems the only peculiar system.

Closer inspection by Buta, during production of the *Catalogue of Southern Ringed Galaxies* (Buta, 1991), led to the suspicion that the apparent bar is really an edge-on disk. This suspicion was confirmed by Buta and Crocker (1993) with new optical data of the galaxy: ESO 235-G58 is probably not a ringed barred spiral of late Hubble type, but it appears to be an interacting galaxy related to the class of inclined disks and polar rings, as it shows a straight dust-lane which splits in two the apparent bar-like structure (Fig.4.2). The analysis of these optical data (Buta and Crocker, 1993) suggests that ESO 235-G58 is a low luminosity edge-on disk, with an equatorial dust-lane,

surrounded by a very large, elongated ring. Thus, ESO 235-G58 may be a good candidate polar ring galaxy. The very low inclination angle between the central galaxy and ring (40^o), which is unusual in PRGs, where these two components are inclined of about 90^o (Whitmore et al. 1990), may suggest that the interaction involved is very recent and the ring may not have reached a stable configuration.

Thus, if ESO 235-G58 really belongs to the class of polar ring galaxies it may provide very useful hints on the formation of this objects. In order to shed light on which kind of object ESO 235-G58 is, the main photometric properties for this galaxy are derived and compared with those for polar ring galaxies, described in Chapter 3. New NIR (in J, H and Kn bands) and optical BVI data for ESO 235-G58 are presented and analysed in the following sections.

4.1 Observations

ESO 235-G58 is a member of the selected sample of Polar Ring Galaxies observed in the NIR J, H and Kn bands, with CASPIR infrared camera (see AppendixA), at the Mt. Stromlo and Siding Spring Observatory 2.3 m telescope. The observations of the whole sample, including ESO 235-G58, (see Tab.2.2) and data reduction has been presented in Sec.2.1.

The optical data were obtained by Buta (in 1992) with a TEK 1024 CCD array (which scale is 0.43 arcsec/pixel) attached to the 1.5 m telescope of Cerro Tololo Inter-American Observatory, and Prof. Buta very kindly gave us these observations to develop the present study. The images were acquired in the Johnson BV and Cousin I filters, with total exposures of 1500s in B, 600s in V and 300s in I band. The reduction and analysis of these data were published by Buta and Crocker in 1993. The images in each bands are shown in Appendix B, Fig.B.6 and Fig.B.7.

4.2 Morphology in the NIR and optical bands

The H band image of ESO 235-G58 is shown in Fig.4.3: the appearance of the galaxy in this band is completely different from what is observed in the B band (Fig.4.1 and Fig.4.2). The NIR morphology of ESO 235-G58 resembles that of an early-type disk galaxy, like an Sa, while the ring and spiral arms, observed in the optical images, are not detected. The only NIR flux associated with this component is an asymmetric elongation, in the NW direction, of the central Sa disk (Fig.4.3). This structure may be debris in the outer ring

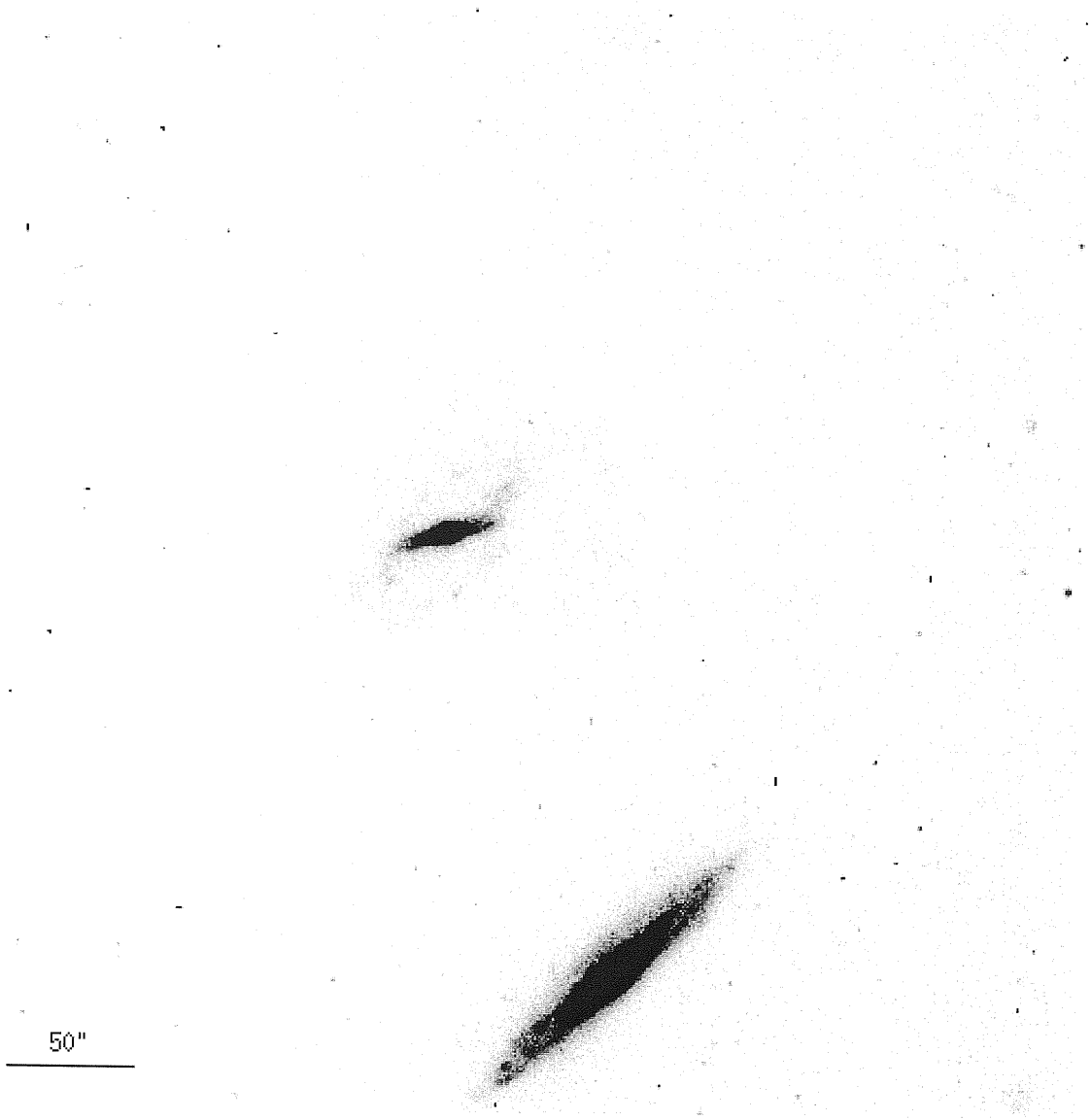

Figure 4.1: B-band image, by Buta and Crocker (1993), covering a $7.3' \times 7.3'$ area including ESO 235-G58 (top middle) and the edge-on spiral ESO 235-G57 (bottom middle). North is at the top and East is to the left. Units are intensity.

Figure 4.2: B-band image of ESO 235-G58. Note that the inner regions are strongly perturbed by a dust lane, which splitting the galaxy along the major axis of the galaxy. North is at the top and East is to the left. Units are intensity.

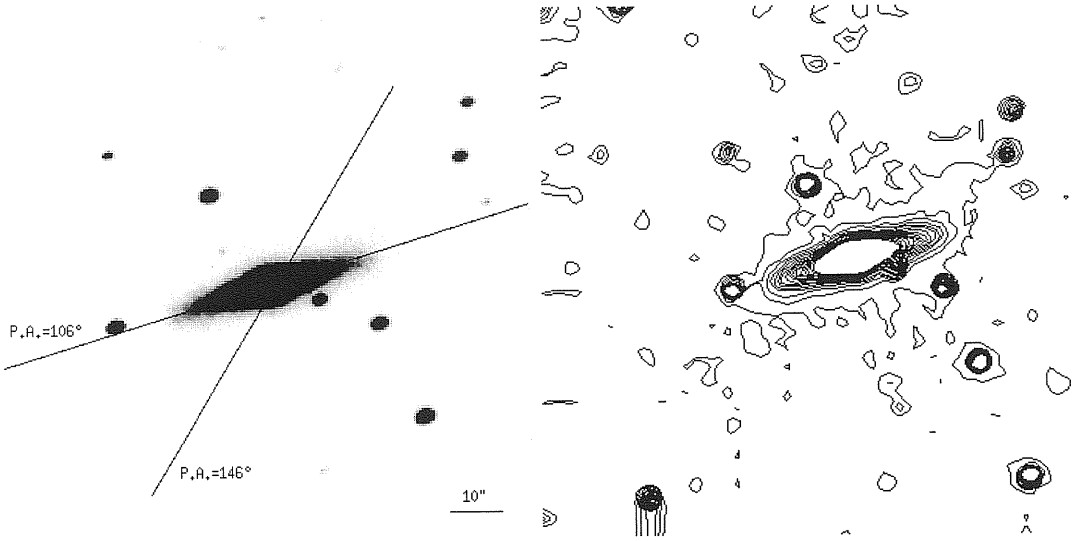

Figure 4.3: H-band image of ESO 235-G58 (left panel) and the relative contour plot (right panel). The lines at $P.A. = 106^o$ and $P.A. = 146^o$ show apparent major axes of the central galaxy and the outer ring respectively. The image size is $2' \times 2'$. North is at the top and East is to the left.

features, which, on the other hand, stands out very clear in the B (Fig.4.1) and V bands (Fig.B.6). This means that the ring structure is much bluer than the central object. The un-sharp masked images are produced for all NIR bands and also for the optical images (Fig.B.6 and Fig.B.7) scaled to the NIR ones, as described in Sec.2.2. This ratio, identified as the "high-frequency residual image", in the NIR bands confirms that the central component in ESO 235-G58 is an edge-on disk galaxy[1]. The unsharp masks of bars often show the squared-off ends (e.g. Erwin and Sparke 1999), which are characteristic of bars in early-type galaxies (Athanassoula et al. 1990). Along the major axis of the galaxy, in the H band high-frequency residual image (left panel of Fig.4.4) a luminous nearly edge-on structure is clearly identified. This feature, on the other hand, is in absorption in the B band high-frequency residual image (right panel of Fig.4.4), but it confirms that the disk is not completely edge-on because the dust lane does not split the bulge equally in two.

[1]Tests was performed on artificial galaxies, characterized by different apparent axial ratio of the bulge and disk components, to checks the reliability of the information given by the un-sharp mask analysis.

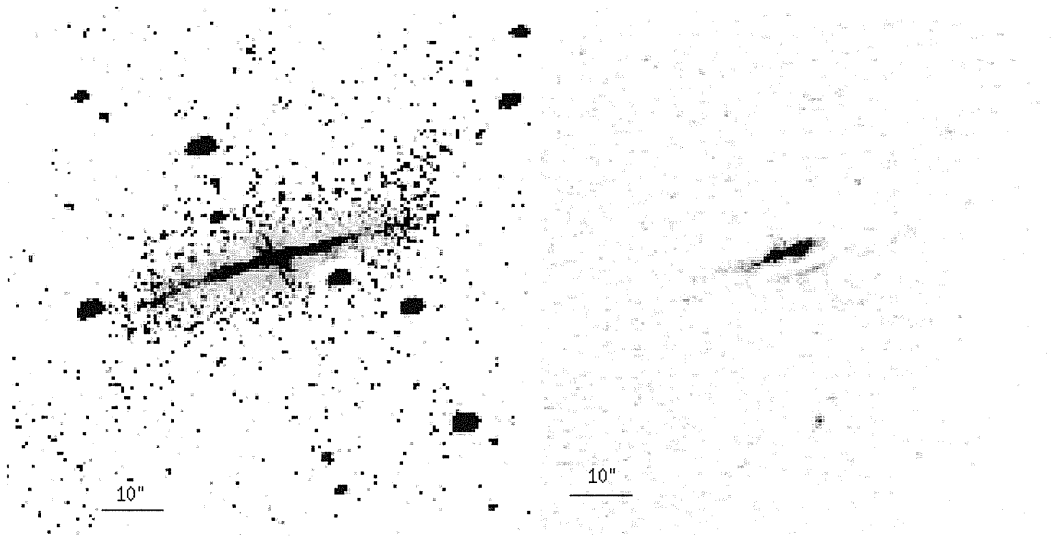

Figure 4.4: High frequency residual image for ESO 235-G58 in the H-band (left panel) and in the B band (right panel). The darker regions are characterized by a value greater than 1, and lighter regions by a value less than 1. North is at the top and East is to the left.

4.3 Photometry: light and color distribution

The surface brightness profiles were derived along the major ($P.A. = 106^o$) and minor axis of the central galaxy, in the NIR and optical bands, and they are shown in Fig.4.5. The dust lane strongly perturbs the optical minor axis profiles, making them slightly asymmetric; it is still significant enough to perturb also the J band profile. The H and Kn band light profiles, in contrast are not strongly influenced by the dust absorption. The analysis of the NIR light profiles, along the minor axis, shows that the bulge component extends out to $10''$, at most; at large distances from the center, the additional light along this axis is related to the ring, which is brighter in B and V bands.

From B to J bands, the light distribution along the NW direction, in the range $5'' < R < 20''$, is more luminous than the corresponding regions along the SE direction: this excess is more likely due to the NW regions of the ring, identified also in the NIR bands as bright elongation of the central galaxy disk in this direction (Sec.4.2 and Fig.4.3). The change in slope, observed at $R \sim 20''$ from the center, in both directions and in all bands, can not be due to the dust absorption, just because it is clearly observed also in H and Kn bands, where this perturbations is reduced to the minimum. The major

axis light profile resembles what is observed in galaxies with a lens component (Kormendy 1979) or with a Type II exponential disk (Freeman 1970).

The surface brightness profiles for the ring structure, shown in Fig.4.6, are obtained in the optical bands only , since this component is almost undetectable in the NIR bands, as stressed in Sec.4.2. In order to cover the whole ring extension, including the spiral arms, the surface brightness profiles for this component are the results of an average of 40 profiles extracted in a cone, centered on the host galaxy and 10 degrees wide from position angle of the ring major axis ($P.A. = 146^o$, by Buta and Crocker, 1993). On average, the ring light distribution seems to have an exponential light profiles; the several bumps, which strongly perturb the B and V profiles, are due to the presence of star formation regions and dust in the ring structure (Fig.B.6).

The J-H, H-K color maps (Fig.4.7) show that the nuclear regions of the galaxy, inside $10''$ from the center, are redder than the outer ones: they correspond to the bulge component, whose extension has been previously estimated to be about $10''$. The B-K color map (Fig.4.8) shows even more details of the structure of ESO 235-G58: it appears again the very red bulge, and the dust lane along the central object major axis, which is much redder than its surroundings. The very blue regions, all around the central galaxy, correspond to the ring structures, which appear more face-on respect to the central object.

4.4 Integrated magnitudes and colors

The integrated magnitudes are computed in the optical and NIR bands, for the whole system, in different areas. The polygons enclosing each area are defined by using the IRAF task POLYMARK, and the integrated magnitudes inside each polygon are evaluated by using the IRAF task POLYPHOT. The photometric errors take into account both photon statistic and background fluctuations (as discussed in Sec.2.5); in the optical bands they are about 3%, whereas in the NIR they are about 10%. The integrated magnitudes and colors derived in each area have been corrected for the galactic extinction within the Milky Way, by using the values for the absorption coefficient in the B band (A_B) and the color excess $E(B-V)$ derived from Schlegel et al. (1998). The absorption coefficients A_λ are derived for each band, by adopting $R_V = A_V/E(B-V) = 3.1$ from Cardelli et al. (1989); the corresponding values are listed in Tab.4.1.

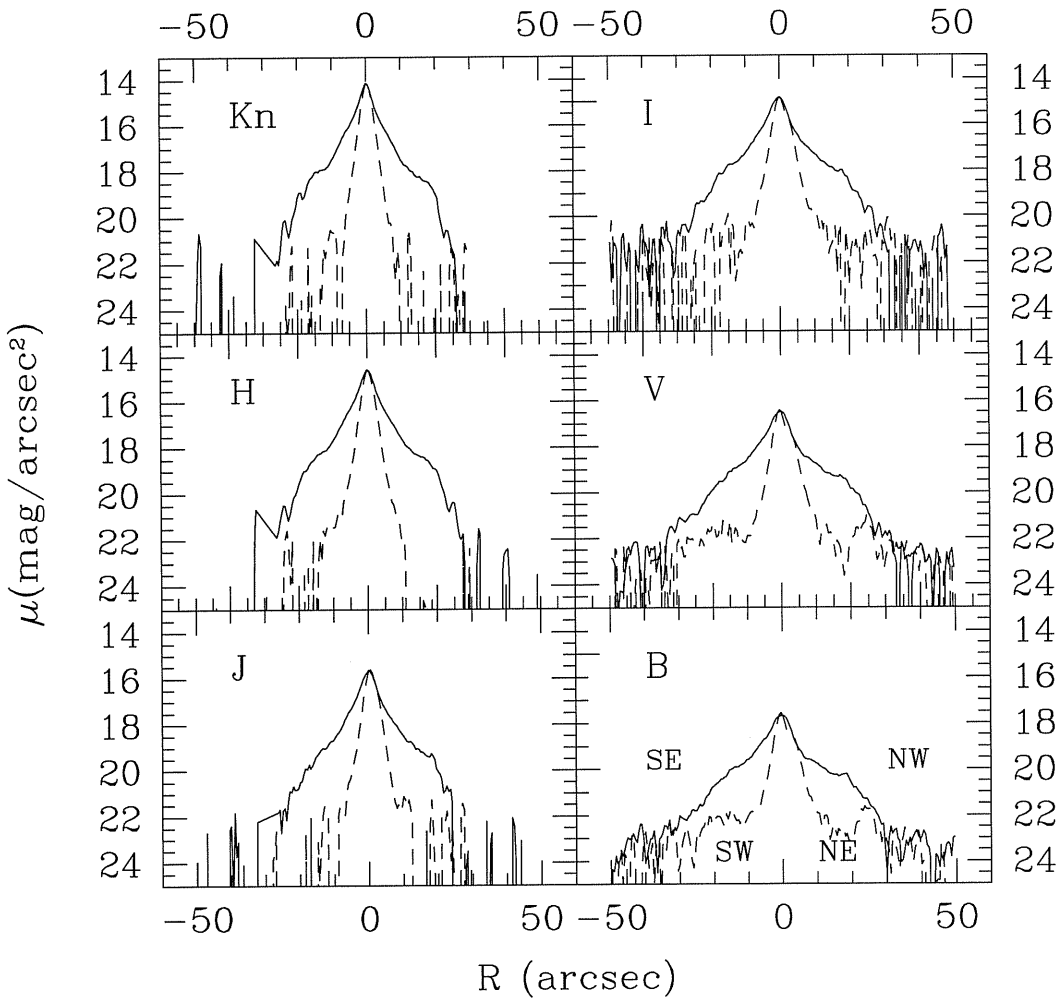

Figure 4.5: NIR (left panels) and optical (right profiles) surface brightness profiles along the major, $P.A. = 106^o$, (continuous line) and minor axis (dashed line) of the central galaxy.

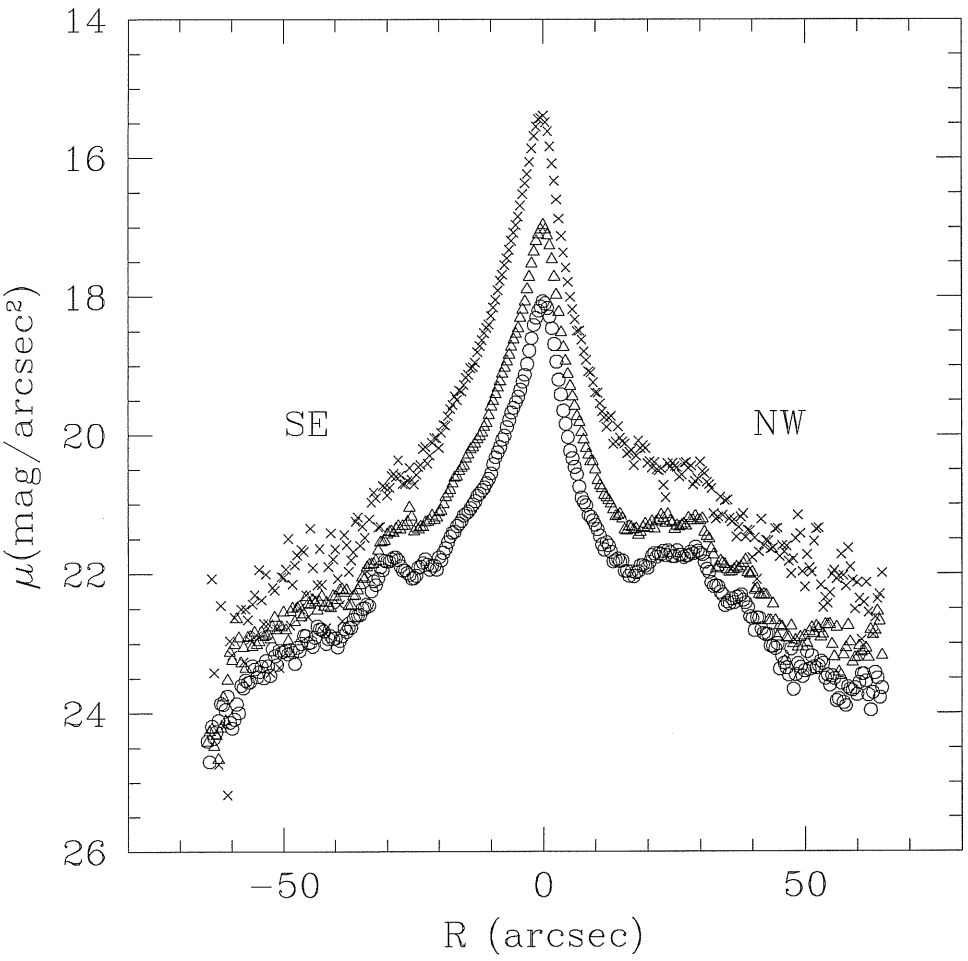

Figure 4.6: Surface brightness profiles along the ring major axis, $P.A. = 146^o$, in B (open circles), V (open triangles) and I bands (crosses).

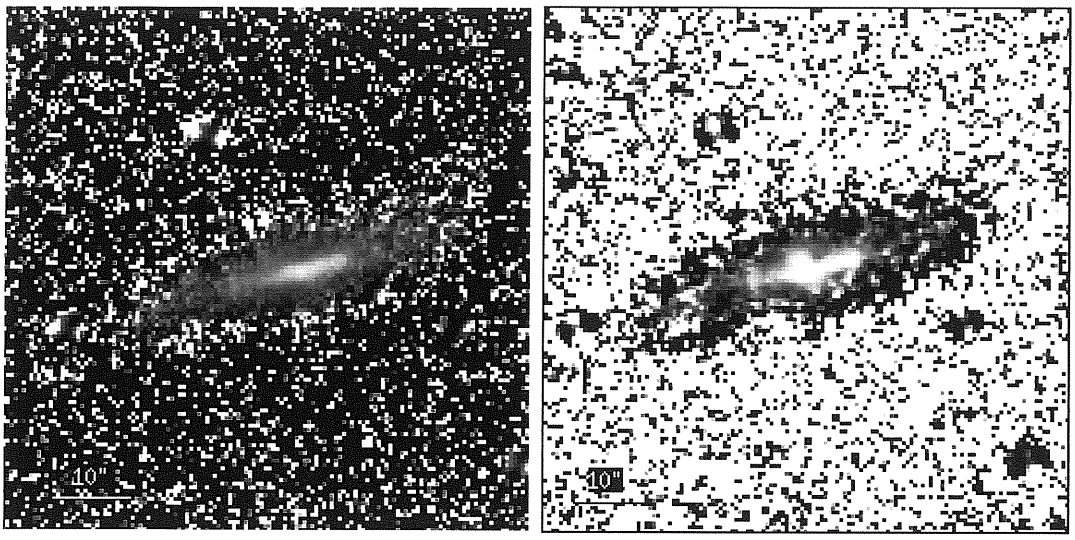

Figure 4.7: J-H (left panel) and H-K (right panel) color map for ESO 235-G58. Darker regions correspond to bluer colors and lighter regions correspond to redder colors. North is at the top and East is to the left.

4.4.1 Optical colors

In B,V,I bands, the areas, where the integrated magnitudes are computed, are chosen as follows: one is coincident with the central galaxy, and two areas are for the ring structure, along SE and NW directions, see Fig.4.9. The polygons are determined in B band, where the ring component is more luminous and extended, and they are used for V and I images, previously registered to the B image. The integrated magnitudes and colors, derived for each area, are listed in Tab.4.2. The B-V vs. V-I colors for the central galaxy and ring (Fig.4.10) are compared with those of (1) standard early-type galaxies (Michard & Poulain 2000), (2) spiral galaxies (de Jong & van der Kruit, 1994), (3) dwarf galaxies (Makarova 1999), (4) LSB galaxies (O' Neil et al. 1997; Bell et al. 2000), and (5) barred galaxy with outer ring (Buta & Crocker, 1992). The colors of the central galaxy, which are redder than those derived by Buta & Crocker (1993), appear very similar to those of late-type Hubble types, like spirals and LSB.

The outer ring is much bluer than the central galaxy; we find colors consistent with the values derived by Buta & Crocker (1993), and similar to those of dwarf galaxies. The strong color gradient between the central galaxy and ring cannot be due to the dust reddening only, since the reddening vector cannot account for the whole color difference. Therefore it implies a difference in stel-

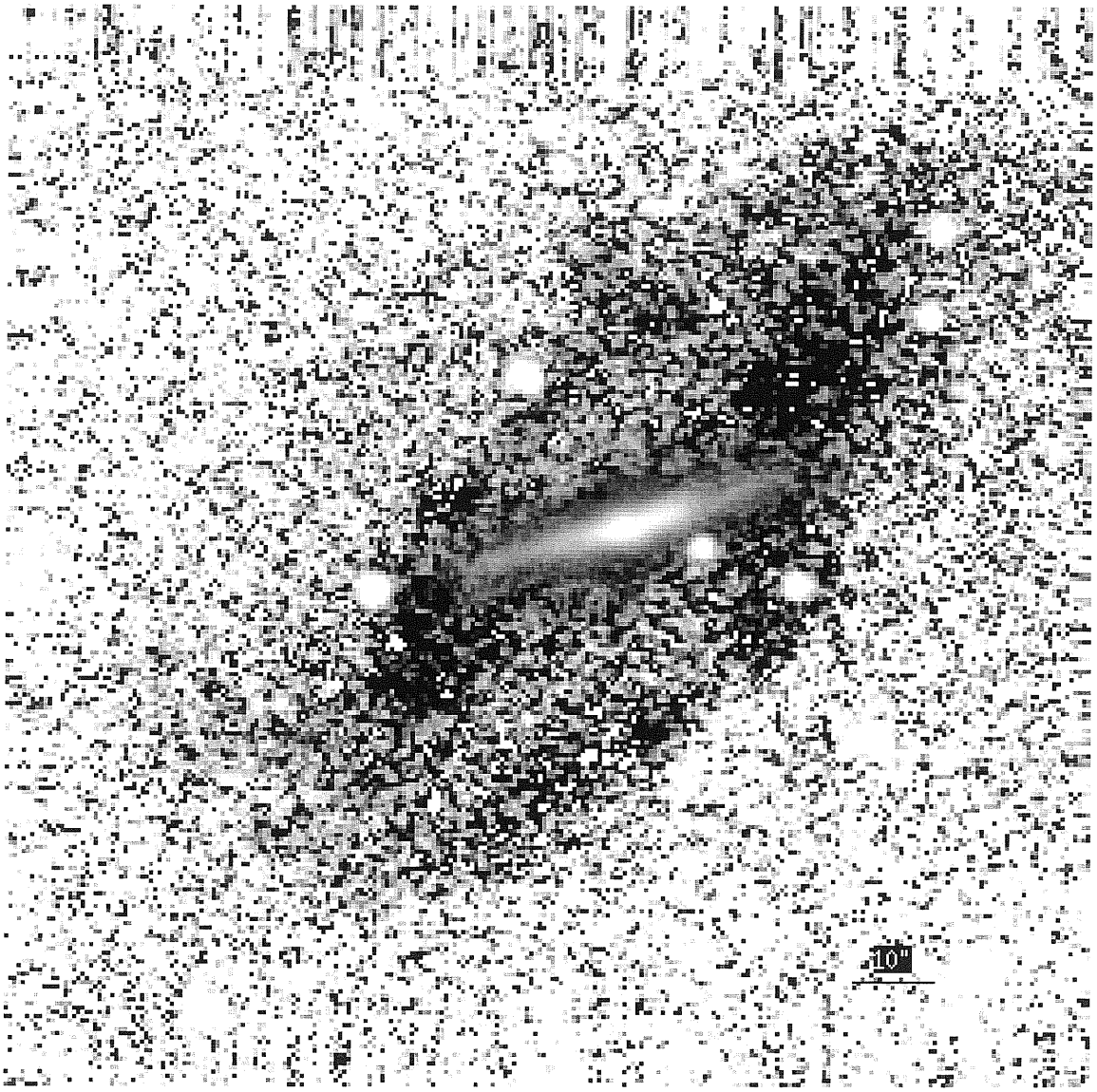

Figure 4.8: B-K color map for ESO 235-G58. Darker regions correspond to bluer colors and lighter regions correspond to redder colors. North is at the top and East is to the left.

lar populations. Furthermore, there is an additional color difference between the two regions of the ring: the NW side of the this component has a redder V-I color with respect to the SE side, which cannot be accounted for by the reddening vector. This "behavior" resembles what has already been observed for the NIR colors of polar rings (see Sec.3.1): this may be caused by different properties of scattering due to the dust and the different distribution of the dust in the ring.

4.4.2 NIR colors

The study of the colors in the NIR concerns the central galaxy, since the ring is hardly detected in these bands (see Sec.4.2) and it is quite hard to define any area where magnitudes and colors can be reliable estimated. Five polygons[2], with same center and larger areas, where defined starting from the galaxy contour in the Kn band. The largest polygon is determined from the outer isophote in the Kn band associated with the galaxy (Fig.4.11). The integrated magnitudes and colors for the ring component were estimated from the difference between fluxes in the two polygons. This choice is suggested by the excess blue light around the central galaxy in the NIR color maps (Fig.4.7). The five polygons are used both for J and H bands and for the optical bands, after the images were registered and scaled to the Kn image. The integrated magnitudes and colors, correspondent to each area, are listed in Tab.4.3. In Fig.4.12 are plotted the J-H vs. H-K (left panel) and B-V vs. V-I (right panel) color diagrams: both in the NIR and in the optical, colors become bluer as areas increases. In both color diagrams, on average, the central galaxy has colors very similar to those of spiral galaxies; the nuclear regions of this component are characterized by the reddest colors. Furthermore, in the optical bands, the central galaxy seems to be redder than the ringed barred galaxies. The inner regions of the ring are much bluer than the central galaxy, as already found for the colors of the non-scaled optical images (in the previous section). In the NIR, on the contrary, the central galaxy and ring seems to have similar colors: since the ring component is very faint in these bands (as also suggested by the constant values of the colors in the last three areas, in Tab.4.3), the correspondent colors may be influenced by background fluctuations.

How do the NIR colors of ESO 235-G58 compare with those of Polar Ring Galaxies (see Tab.2.5)? A common characteristic in ESO 235-G58 and PRGs is the very red nucleus respect to the outer regions of the host galaxy.

[2]These polygons are different from those defined for the optical images, described in Sec.4.4.1.

Table 4.1: Absorption coefficients for the Galactic extinction in ESO 235-G58.

Band	A_λ (mag)
B	0.167
V	0.128
I	0.075
J	0.035
H	0.022
Kn	0.014

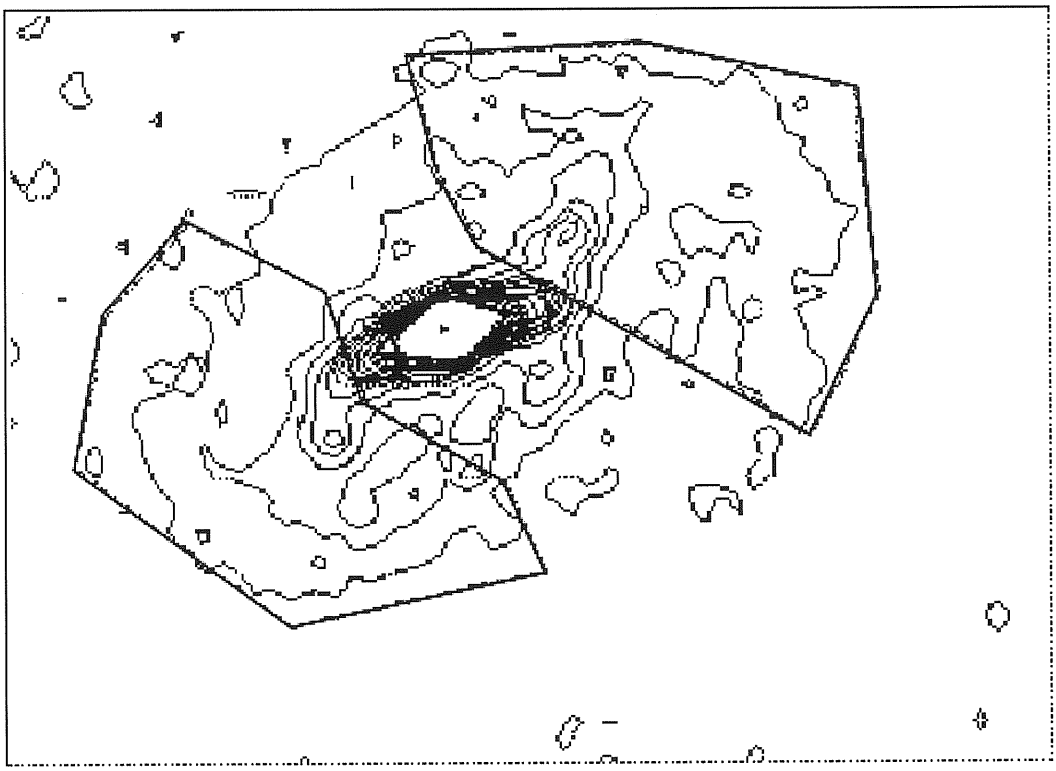

Figure 4.9: ESO 235-G58 contour plot in B band (continuous line) plus the 3 polygons (dashed lines) limiting the different areas where the integrated magnitudes are computed. North is at the top and East is to the left.

Table 4.2: Integrated magnitudes and colors, in the optical bands, for the central galaxy and ring in ESO 235-G58.

Component	m_B	M_B	B-V	V-I
GALAXY	16.27	-17.6	0.98	1.37
RING (NW)	16.73	-17.2	0.32	0.81
RING (SE)	16.93	-17.0	0.39	0.51

Table 4.3: Integrated magnitudes and colors of different regions in ESO 235-G58. In the second column are listed the largest distances from the center (in arcsec) reached by each area.

Region	a (arcsec)	m_B (mag)	m_J (mag)	B-V	V-I	B-H	J-K	J-H	H-K
A1	2.7	18.51	14.72	1.18	1.65	4.78	1.36	0.99	0.36
A2	10	16.85	13.59	1.08	1.45	4.16	1.19	0.90	0.29
A3	18.2	16.22	13.23	0.99	1.36	3.84	1.12	0.85	0.26
A4	22.7	16.01	13.13	0.95	1.32	3.72	1.10	0.84	0.26
A5	40	15.7	13.05	0.85	1.24	3.49	1.10	0.84	0.26
RING		17.19	15.97	0.48	0.78	2.06	1.16	0.84	0.32

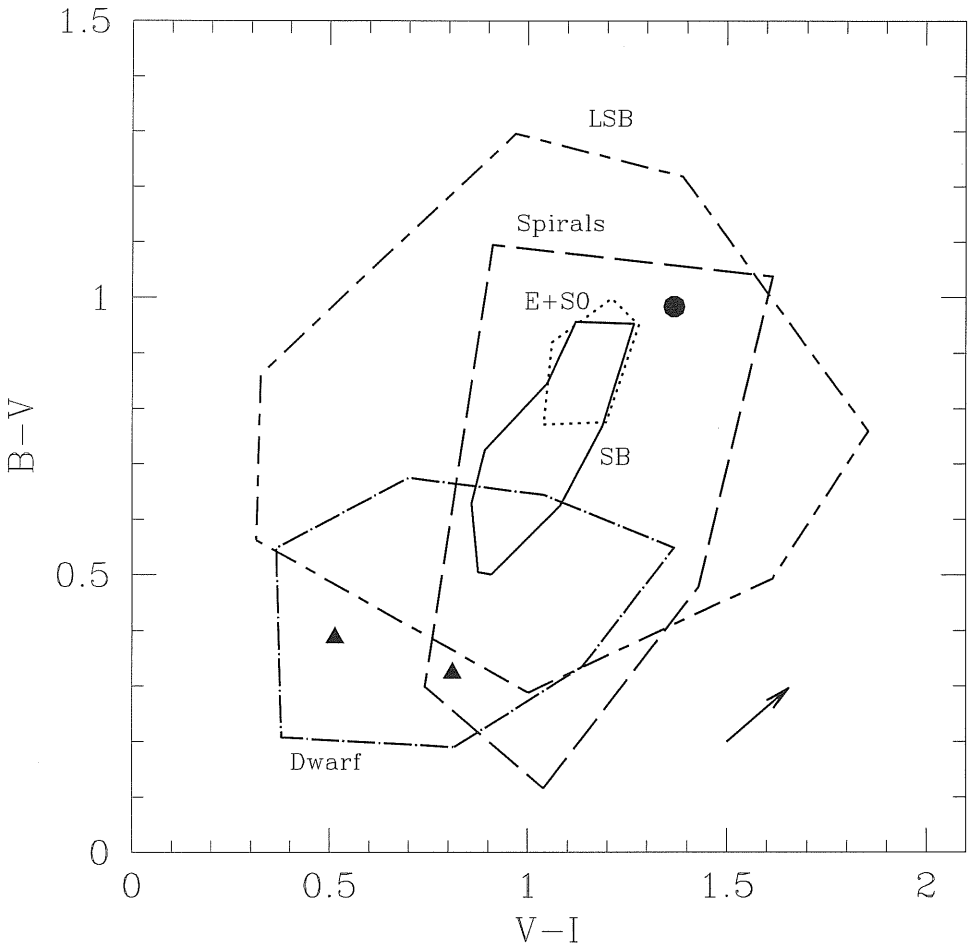

Figure 4.10: B-V vs. V-I color diagram for the central galaxy (filled circle) and ring (filled triangles) in ESO 235-G58. The dotted contour limits the region where the Es and S0s integrated colors are found; the long-dashed contour limits the integrated colors of spirals; the dashed-dotted contour identifies the integrated colors of the dwarf galaxies, the long dashed - short dashed contour identifies the integrated colors of LSB galaxies and the continuous contour limits the integrated colors of barred galaxies with outer rings. The arrow, in the lower right corner, indicates the reddening vector for galactic dust and the screen model approximation.

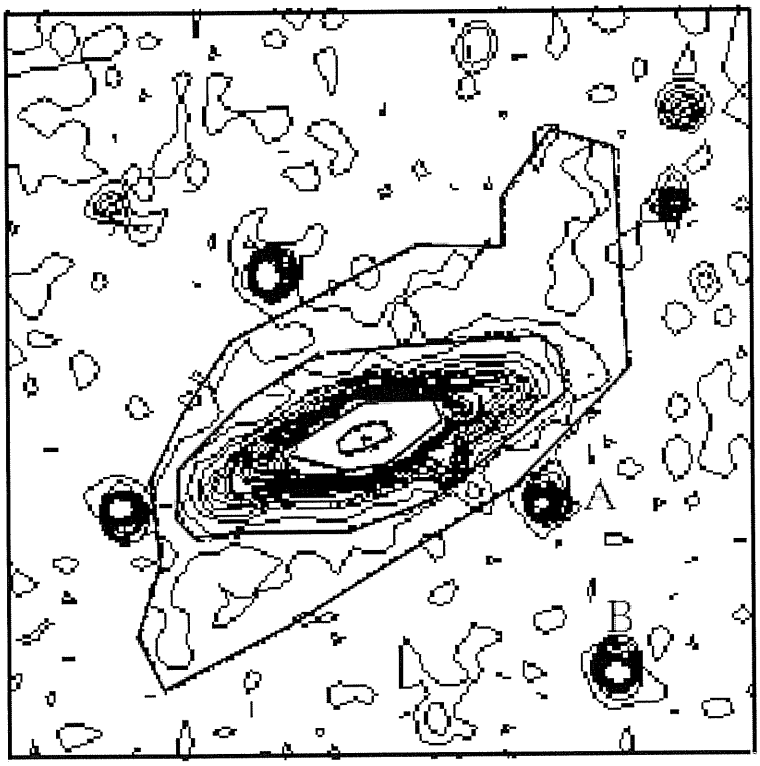

Figure 4.11: ESO 235-G58 contour plot in Kn band (continuous line) plus the concentric five polygons (heavier lines) limiting the areas where the integrated magnitudes are computed. The distance between the two stars (A and B) is about 20″. North is at the top and East is to the left.

4.5 Age estimate in ESO 235-G58

The stellar population synthesis model by Bruzual & Charlot (1993), described in Sec.3.3, were used to reproduce the integrated colors of different regions (see Sec.4.4) in ESO 235-G58. The main goals are to derive an estimate of the stellar population ages in the central galaxy and in the outer ring, and to compare them with the typical ages obtained for the host galaxy and polar ring in PRGs (see Sec.3.3). The morphology of ESO 235-G58 in the NIR, where the perturbations due to the dust are less significant, is very similar to an Sa galaxy, as emphasized in Sec.4.2, even if it shows redder colors (Sec.4.4). So, for this component, could be reasonably adopt a star formation history with an exponentially decreasing rate, $SFR(t) = \frac{1}{\tau} \exp(-t/\tau)$, with a very small time-scale τ, in order to approximate a single burst of star formation. The

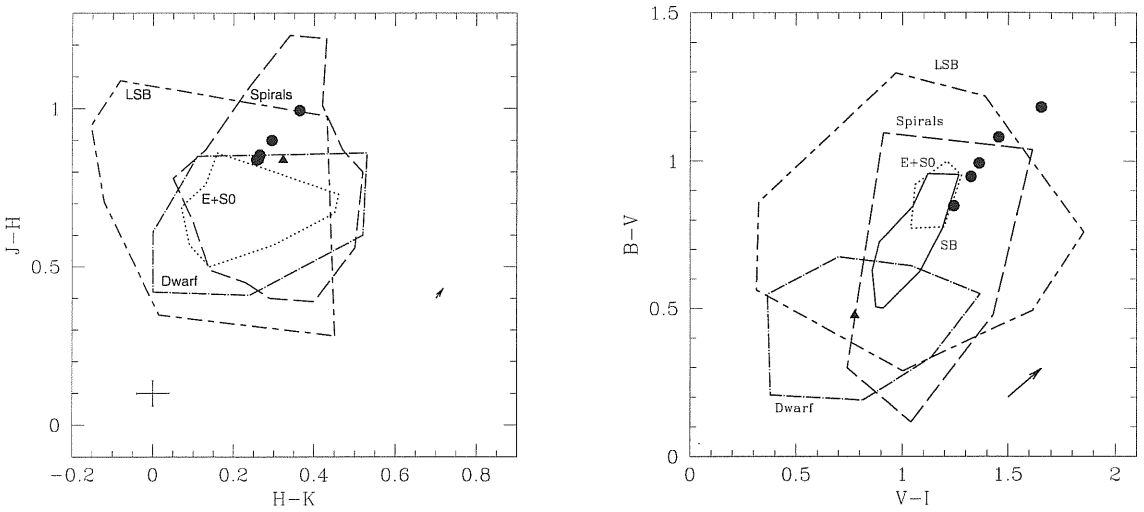

Figure 4.12: J-H vs. H-K (left panel) and B-V vs. V-I (right panel) color diagram for the central galaxy (filled circles) and ring (filled triangles) in ESO 235-G58. The dotted contour limits the region where the Es and S0s integrated colors are found; the long-dashed contour limits the integrated colors of spirals; the dashed-dotted contour identifies the integrated colors of the dwarf galaxies and the long dashed - short dashed contour identifies the integrated colors of LSB galaxies and the continuous contour limits the integrated colors of barred galaxies with outer rings. The arrow, in the lower right corners, indicates the reddening vector for galactic dust and the screen model approximation.

adopted values for the time scale parameter is $\tau = 1$ Gyr. The evolutionary tracks correspondent for this model were derived for different metallicities ($Z = 0.0004$, $Z = 0.008$, $Z = 0.02$, $Z = 0.05$, $Z = 0.1$), which were assumed constant with age, and they are plotted in Fig.4.13, for the B-H and J-K colors, for the central galaxy. The evolutionary tracks relative to the ring model are plotted for the B-V and V-I colors, because the NIR colors derived for this component are too uncertain and could not give a realistic age estimate. As stressed in Sec.3.3, the B-H vs. J-K color diagram is used to break the age-metallicity degeneracy for the central object. The lines of constant age were computed from the evolutionary tracks: for the central galaxy in ESO 235-G58 they suggest an age between 1 to 3 Gyr.

For the ring structure a constant star formation rate was adopted: this choice was mainly suggested by the active star formation regions observed in the B and V bands (see Fig.4.1 and Fig.B.6). This component seems to be much younger than the central galaxy and it is not older than 10^8 yr. Unfortunately, the age estimate for this component is very uncertain, since it is very faint in the NIR (see Sec.4.4.2), so this value must be considered as an upper limit.

The age for the central galaxy in ESO 235-G58 falls in the same range of values derived for the host galaxy in PRGs; the ring component, on the contrary, seems to be younger than polar rings (Sec.3.3).

4.6 Study of the light distribution in the central galaxy of ESO 235-G58

The study of the light distribution in the central galaxy of ESO 235-G58 should provides new hints in order to understand whether this object may really belong to the class of PRGs, or it is more similar to a spiral barred galaxy. To this aim, the 2D model of the central galaxy light distribution is done in the Kn band, where the perturbations due to the dust absorption are weaker. The 2D model[3] is given by a spheroidal central component, whose projected light follows the generalized de Vaucouleurs law (Eq.3.1), and an exponential disk (Eq.3.2). The regions affected by foreground stars and the ring light, which mainly perturbs the outer regions of the central galaxy along its major axis (Fig.4.11), are accurately masked, before the fit is performed. The structural parameters for bulge and disk components are listed in Tab.4.4. As discussed

[3]This is the same fitting model adopted to study the host galaxy light distribution in PRGs, and a detailed description is given in Sec.3.3.

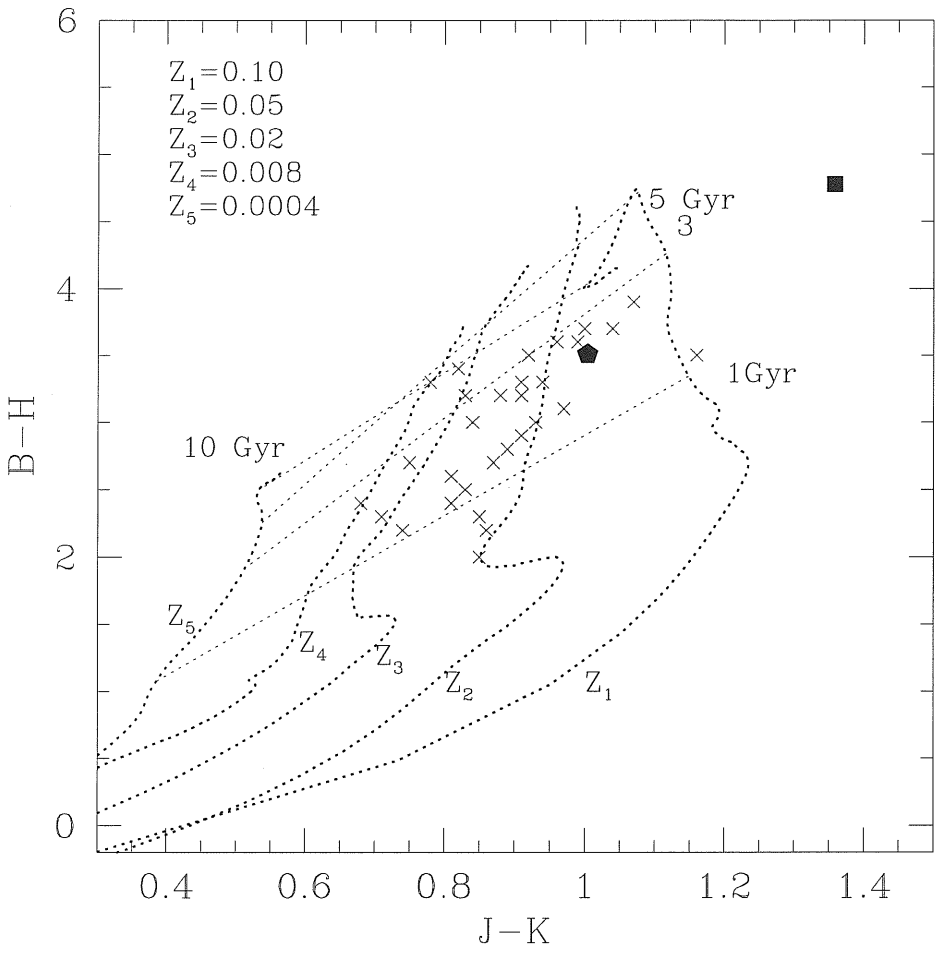

Figure 4.13: B-H vs. J-K diagram of the evolutionary tracks for the stellar synthesis models optimized for the central galaxy in ESO 235-G58. The heavier dotted lines correspond to models with a characteristic timescale $\tau = 1Gyr$. Models are computed for different metallicities as shown on this figure. Light dotted lines indicate loci of constant age for the different models; different ages are reported on the plot. The filled square and pentagon correspond respectively to the nucleus and the outer regions of the central galaxy in ESO 235-G58; crosses are for a sample of spiral galaxies (Bothun et al., 1984).

previously in Sec.4.2, a dust lane is observed along the major axis of the central galaxy, which becomes dominant towards bluer colors (see Fig.4.7 and Fig.4.8). Since the model computes an average 2D light distribution, one would expect an over-estimation at the dust lane position and an under-estimation elsewhere. This is in agreement with the comparison between the observed and calculated light profiles, shown in Fig.4.14. In the central regions ($r \leq 5''$) the light distribution derived by the fit is brighter than the galaxy light ($\Delta\mu \leq 0.6$ mag): this could reasonably be due to the dust lane, which tends to obscure the galaxy light.

Along the minor axis, in the SW direction, the light distribution derived by the fit is brighter than the galaxy light ($\Delta\mu \leq 0.4$ mag), wheras, along the NE directions galaxy light is more luminous than the model ($\Delta\mu \leq 0.4$ mag). Also these differences are easily explained by dust absorption.

As pointed out in Sec.4.3, the light profiles along the major axis deviates from the exponential decrease (at about $R \sim 10''$): the differences between the observed and calculated light profiles, at $R \geq 10''$ are just due to this shape of the surface brightness distribution.

The 2D model, for the central galaxy, in the J and H bands, and in the B, V, I bands, is simply a scaled version of the Kn band model, based on the average colors derived for this component (given in Tab.4.3). Fig.4.15 shows the ratio between the whole image for ESO 235-G58 (i.e. including the outer ring) and the 2D model for the central galaxy, in the H band. The faint structure related to the ring stands out very clear in this "residual image": these features are found around the central galaxy and they are elongated toward the NW and SE directions, at the edge of this component, along the major axis.

Fig.4.16 (right panel) shows the residual image in the B band: the light distribution of the whole ring and spiral arms stands out very clear. In Fig.4.17 the same residual image (in the B band) is shown, but it is displayed with an inverted color map, in order to show better the regions where the dust absorption is strongly significant. Inside about $15''$ from the center, along the major axis, the model is 2 times brighter than the galaxy.

4.6.1 Analysis of the structural parameters

The structural parameters, which characterized the light distribution of the central galaxy in ESO 235-G58, are compared with the values derived for PRGs (Sec.3.3.3 - Sec.3.3.5), with those typical of early-type and spiral galaxies. The chosen sample of early-type galaxies has been studied by Bothun and

Table 4.4: Structural parameters for the central galaxy, in the Kn band, for ESO 235-G58. The effective surface brightness μ_e and the central surface brightness μ_0 are in $mag/arcsec^2$, and μ_0^c is corrected for the inclination. r_e and r_h are respectively the effective radius and disk scalelength derived in arcsec, the corresponding values expressed in kpc are derived by using $H_0 = 70$ km s^{-1} Mpc^{-1}.

Parameter	value
μ_e	15.52 ± 0.08
r_e (arcsec)	1.84 ± 0.08
r_e (kpc)	0.54 ± 0.02
μ_0	15.00 ± 0.03
μ_0^c	16.56 ± 0.05
r_h (arcsec)	4.71 ± 0.06
r_h (kpc)	1.39 ± 0.02
q_b	0.88 ± 0.02
q_d	0.237 ± 0.004
n	0.95 ± 0.08
B/D	0.7 ± 0.2

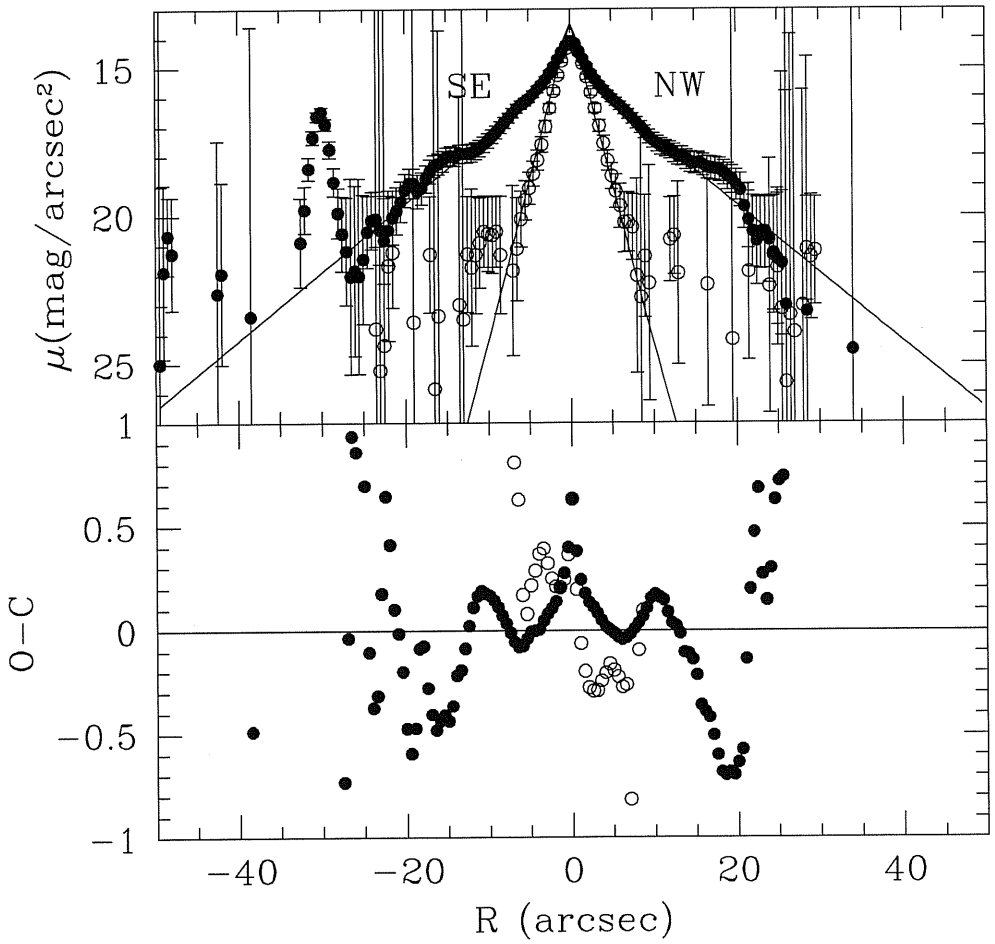

Figure 4.14: 2D fit of the K-band central galaxy light distribution in ESO 235-G58, adopting the two-component model (bulge+disk), described in Sec.3.3.2. The observed light profiles along the major (filled dots), $P.A. = 106^o$, and minor axis (open dots), $P.A. = 196^o$, are compared with those derived by the fit (continuous line), which was performed in the Kn band. The orientation, reported on the plot, refers to the major axis.

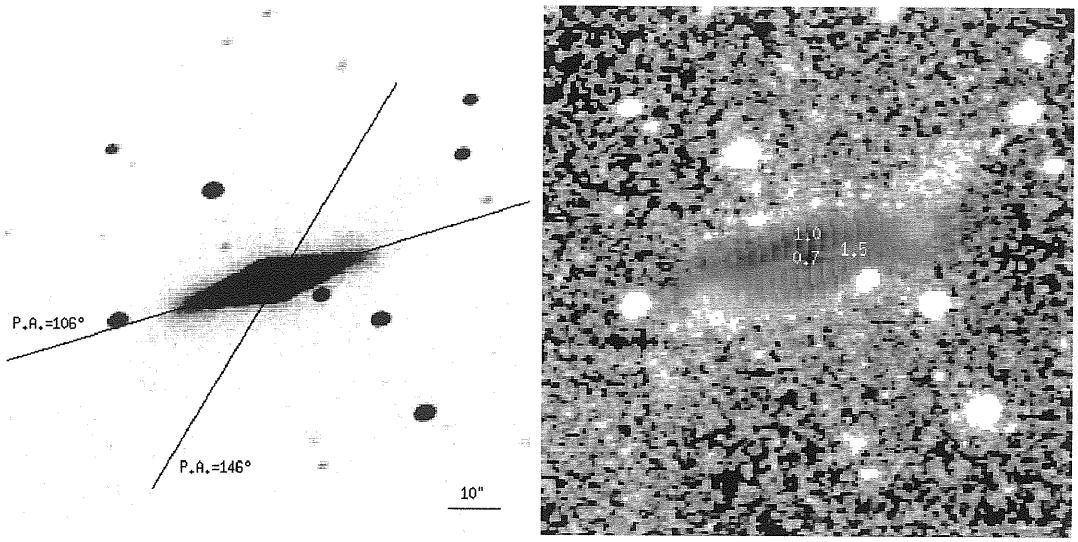

Figure 4.15: Left panel - H band image of ESO 235-G58. Right panel - Residual image obtained as the ratio between the whole image of ESO 235-G58 and the 2D model for the central galaxy in the H band. Units are intensity; whiter colors correspond to those regions where the galaxy is brighter than the model, darker colors corresponds to those regions where the galaxy is fainter than the model. North is up and East is to the left.

Gregg[4] (in 1990). The structural parameters for a sample of spiral galaxies has been derived by de Jong (in 1996), in B and K bands, by modeling the light distribution of the bulge and disk component with an exponential law.

Fig.4.18 (left panel) plots the location of the bulge of ESO 235-G58 in the plane of effective parameters μ_e and r_e: this object falls in the region of smaller and brighter bulges, where also PRGs and half of the spiral galaxies of the sample are found. Fig.4.18 (right panel) shows the comparison of the scale parameters, n and r_e, for the bulge component in ESO 235-G58, in PRGs, for a sample of early-type galaxies in the Virgo cluster (Caon et al., 1993) and for a sample of LSB galaxies in Fornax cluster (Davies et al., 1988). Also in this plane, ESO 235-G58 is located in the same regions where PRGs are found: this object, as PRGs, seems to be characterized by an exponential bulge ($n = 0.95$,

[4]The structural parameters for these objects were obtained, in the B band, by fitting the light distribution with the super-position of a de Vaucouleurs' law ($n = 4$) and an exponential disk, for the bulge and disk component respectively. The surface brightness parameters in the K band are derived by taking into account the average B-K color of these objects.

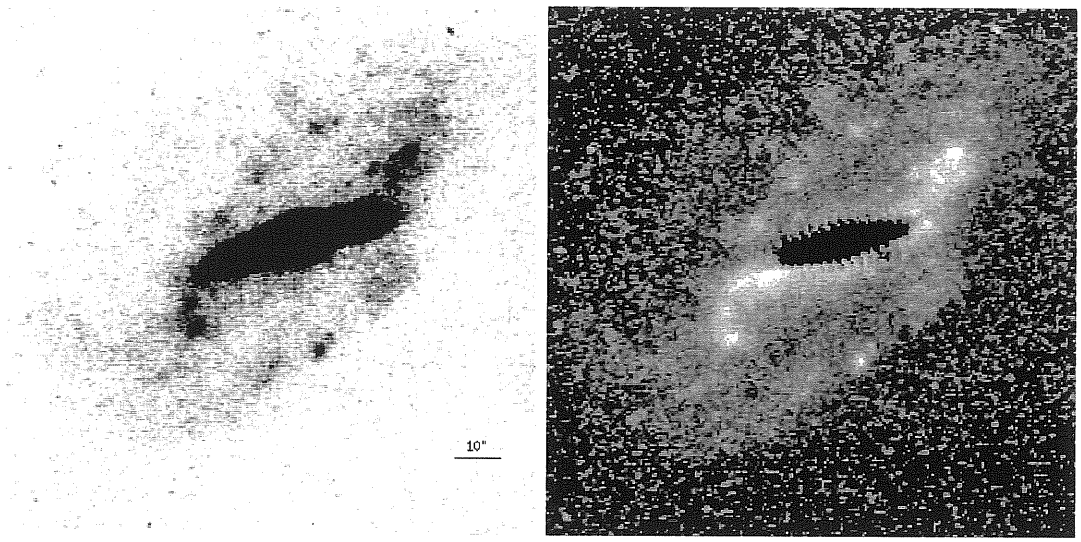

Figure 4.16: Left panel - B band image of ESO 235-G58. Right panel - Residual image obtained as the ratio between the whole image of ESO 235-G58 and the 2D model for the central galaxy in the B band. Units are intensity; whiter colors correspond to those regions where the galaxy is brighter than the model, darker colors corresponds to those regions where the galaxy is fainter or equal to the model. This figure was displayed in shuch a way to enhanced the ring structures, so the darker central area includes also the regions where this image ratio is about 1. North is up and East is to the left.

Tab.4.4), which make all of them (PRGs and ESO 235-G58) more similar to LSB and spiral galaxies rather than to early-type galaxies.

The disk component in the central galaxy of ESO 235-G58 is characterized by higher value for the central surface brightness μ_0^c and a lower value for the scalelength r_h, respect to the average values for these parameters in spiral and early-type galaxies. On the other hand, also the disk component in this object seems to have similar properties to disks in the host galaxy of PRGs (Fig.4.19, left panel). The Bulge-to-Disk ratio obtained for ESO 235-G58 ($B/D = 0.7$) is greater than the typical value for spiral galaxies (Fig.4.19, right panel), which varies in the range $0.019 < B/D < 0.54$, wheras it is very close to the B/D value obtained for the Polar Ring Galaxy ESO 415-G26 (see Tab.3.2).

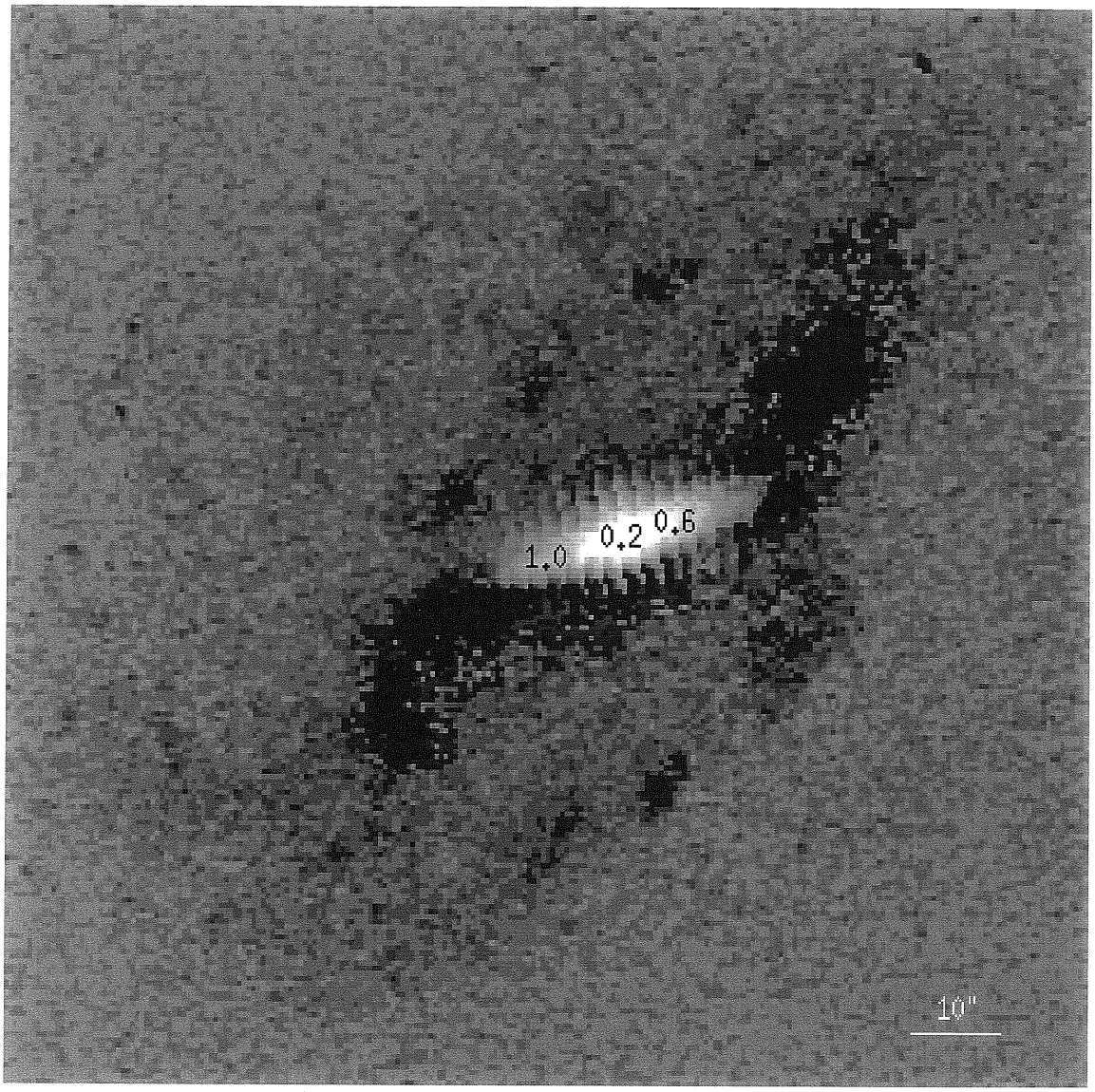

Figure 4.17: Same residual image shown in Fig.4.16, but displayed with an inverted color map, in order to emphasize the regions where the dust absorption is strongly significant. Numbers indicate the value of the ratio at that particular isophote. North is up and East is to the left.

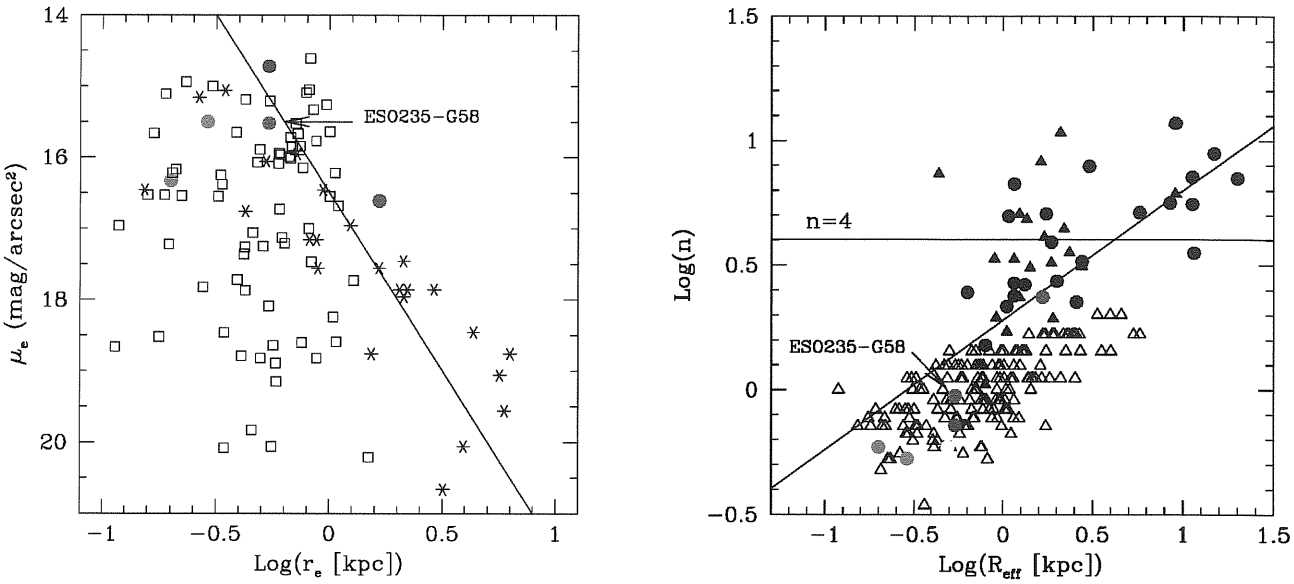

Figure 4.18: Left panel - Relation between the bulge effective parameters (Sec.3.3.1) determined in the Kn band for ESO 235-G58 (blue filled circle). They are compared with values derived, in Sec.3.3.2, for PRGs (filled circles, the color code is defined in Tab.3.1), with typical values for early-type galaxies (asterisks) and for spiral galaxies (open squares). The solid line is a line of constant bulge luminosity derived for $n = 4$ and passing through the point $\mu_e = 18\ mag/arcsec^2$, $r_e = 2$ kpc. Right panel - Relation between the effective radius r_e and the n exponent of the generalized de Vaucouleurs' law (Sec.3.3.1), for the bulge component in ESO 235-G58. They are compared with values derived, in Sec.3.3.2, for PRGs, with the typical values for early-type galaxies, Ellipticals (black circles) and S0s (black triangles) and for LSB galaxies (open triangles). The plotted n exponents values for the early-type galaxies are those derived by Caon et al. (1993) along the minor axis of the system, in order to exclude the contribution from a possible disk component. The solid line is the relation between n and r_e derived by Caon et al. (1993): $\log n = 0.28 + 0.52 \log r_e$.

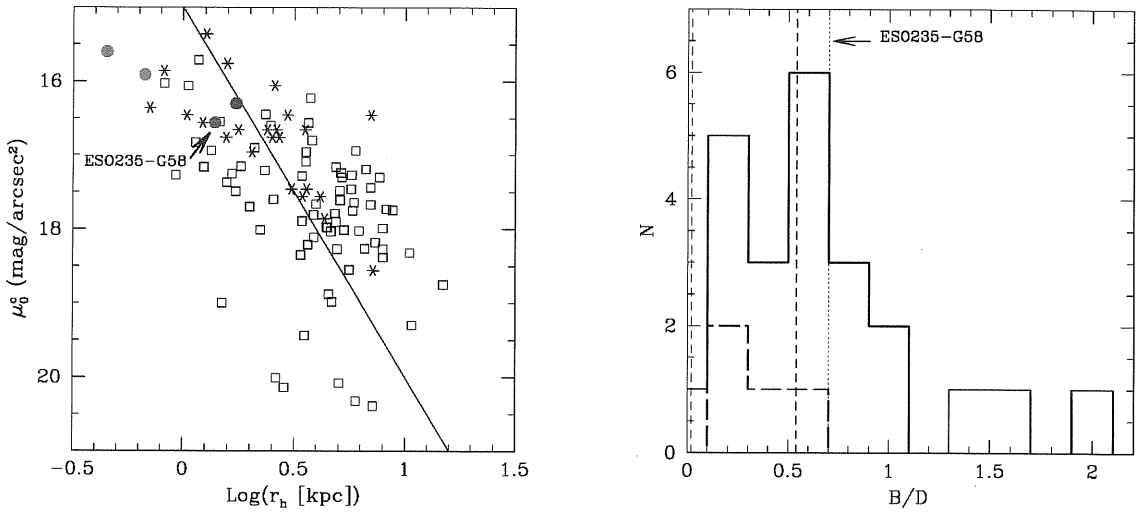

Figure 4.19: Left panel - Relation between the central surface brightness, corrected for the inclination, and the scalelength of the disk component (Sec.3.3.1) in the central galaxy of ESO 235-G58 (blue filled circle). They are compared with values obtained for PRGs (Sec.3.3.2; filled circles whose color code is defined in Tab.3.1); with the typical values for early-type galaxies (asterisks) and for spiral galaxies (open squares). The solid line is a line of constant disk luminosity, derived for $\mu_0^c = 18\ mag/arcsec^2$ and $r_h = 1.6$ kpc. Right panel - B/D distribution for the PRGs (long-dashed line) and for early-type galaxies, by Bothun and Gregg (1990), (continuous line). The dotted line indicates the value of B/D derived for ESO 235-G58 (Tab.4.4); short-dashed lines limits the range of variations for the B/D values for spiral galaxies.

4.7 Study of ring light distribution in the B band

As pointed out in Sec.4.2, the outer ring in ESO 235-G58, which surrounds the central galaxy, is very bright in B and V band, and its luminosity strongly decreases towards the NIR bands. Furthermore, it was also stressed that from the ring edges emerge two asymmetric spiral arms (Fig.4.16). The study of the ring light distribution in the B band, where this component is brighter, may add new details to those derived by the NIR analysis, in order to clarify the nature of ESO 235-G58. The folded light profile in the B band (Fig.4.20) was derived by the surface brightness profiles extracted along the ring major axis in the two main directions (Sec.4.3, Fig.4.6). This light distribution was adopted to derive the $\Delta R/\bar{R}$ ratio, defined in Sec.3.4 (Eq.3.3), starting from $r \geq 3r_e$, in order to exclude the contribution from the central galaxy light. For the ring component in ESO 235-G58, $\Delta R/\bar{R} = 45\%$: this value is close to the lower limit in the range of values derived for a sample of spiral galaxies (de Jong, 1996), which is $45\% \leq \Delta R/\bar{R} \leq 75\%$. On the other hand, it is near to the upper limit in the range of values derived for PRGs (Fig.3.14): it is comparable to the $\Delta R/\bar{R}$ ratio derived for the wide polar ring galaxy A0136-0801 (see Tab.3.3).

By fitting the ring light distribution with an exponential law (Eq.3.2), we derived an estimate of the central surface brightness ($\mu_0 = 25.80 \pm 0.05$ $mag/arcsec^2$) and of the scalelength ($r_h = 23.0 \pm 0.5$ arcsec; $r_h = 6.7 \pm 0.2$ kpc). In Fig.4.21 these parameters are compared with the values for a sample of spiral galaxies (by de Jong, 1996) and for a sample of LSB galaxies (by O'Neil et al. 1997): the scalelength of ring structure in ESO 235-G58 seems to be larger than the typical values for LSB galaxies, whereas it is comparable with the average value observed for spiral galaxies. Unfortunately, only an approximate estimate of the ring inclination is available ($i \sim 86^o - 87^o$), derived by Buta and Crocker (1993), then the corrected values for the central surface brightness is also very uncertain; anyway, ring luminosity seems to be very close to the faintest LSB galaxies.

4.8 Summary

We have discussed the NIR and optical properties of the peculiar galaxy ESO 235-G58: at a first sight, this object resembles a late-type barred spiral with an outer ring (Fig.4.1). An accurate photometric study in the optical

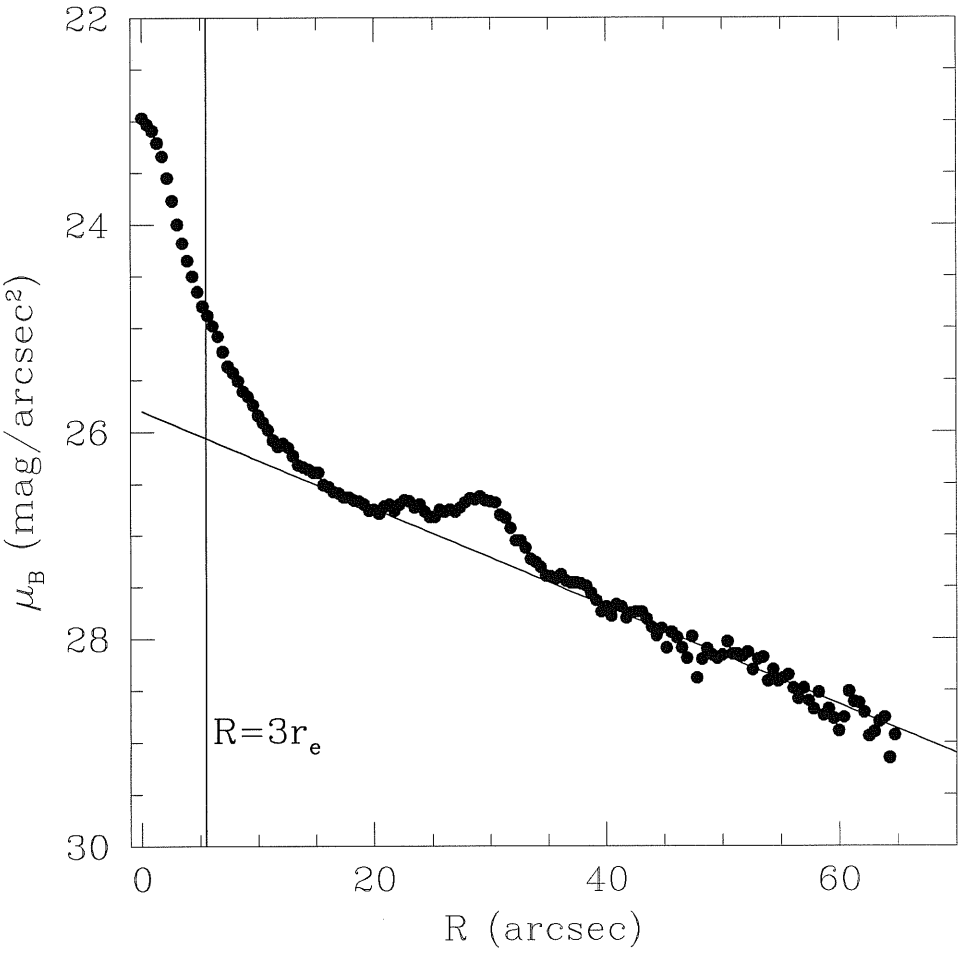

Figure 4.20: B-band average surface brightness profile for the ring structure, in ESO 235-G58. The straight line is the exponential fit to the ring light distribution; the dotted line indicates the starting distance from the center used in the computation of $\Delta R/\bar{R}$ ratio (Eq.3.3).

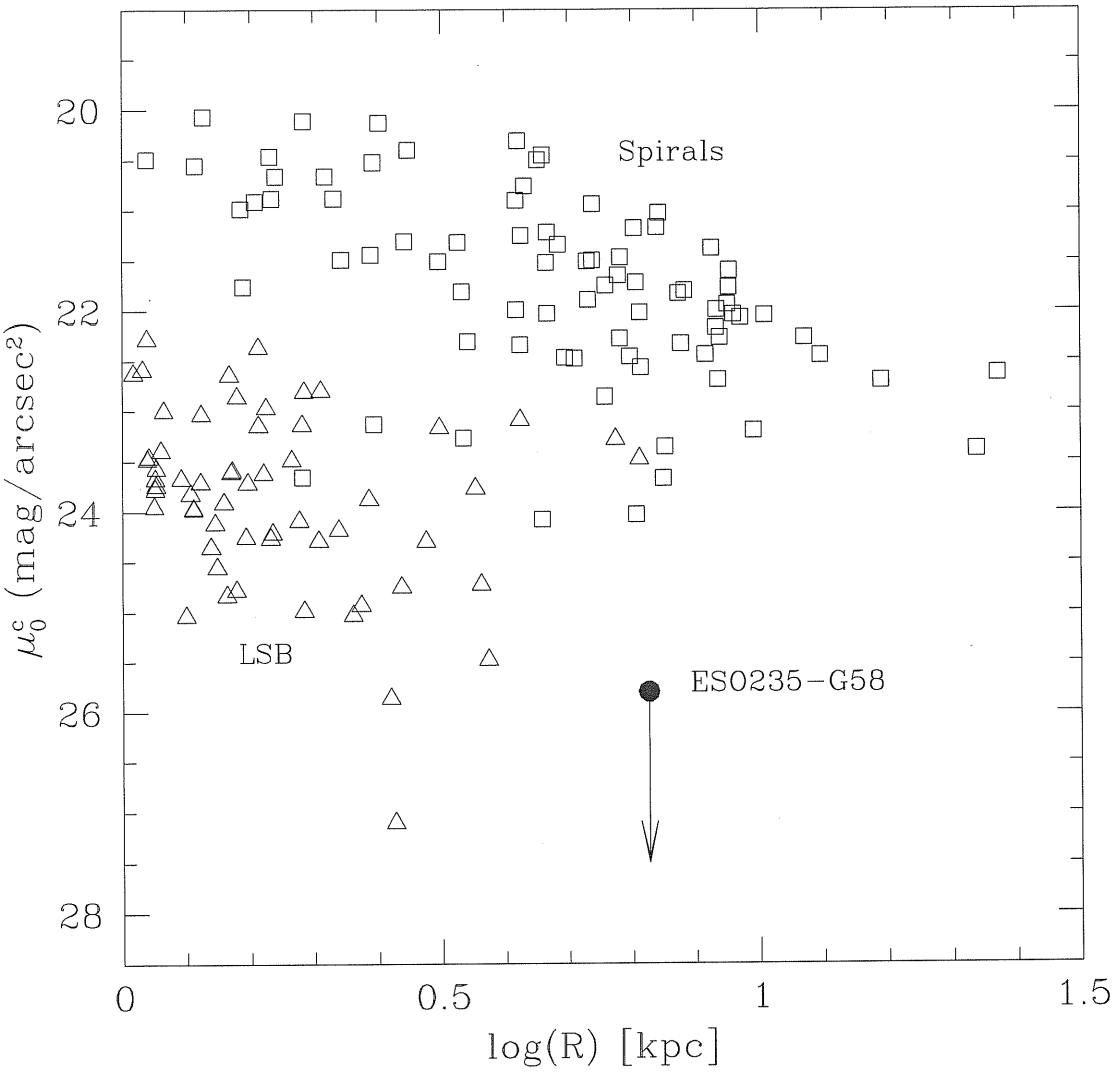

Figure 4.21: Structural parameters (μ_0 and r_h) for the B-band light distribution in the ring structure of ESO 235-G58 (blue filled circle). They are compared with the typical values for spiral galaxies (open squares) and for LSB galaxies (open triangles). The arrow indicates the value of μ_0 corrected for inclination (Sec.4.7).

bands let Buta & Crocker (1993) to classify ESO 235-G58 as an interacting system related to the polar ring galaxies. For this peculiar object, we have analysed the light and color distribution in the NIR and optical bands and we have compared them with the typical properties observed for the PRGs in our sample (described in Chapter 2 and in Chapter 3). As we have found for PRGs, the high-frequency residual images shows that the central galaxy in ESO 235-G58 has an edge-on disk. The analysis of the color and light distribution in this component strongly suggests that ESO 235-G58 cannot be a barred galaxy and that it shows many similarities to the host galaxy in PRGs of our sample. The ring structure is characterized by very blue colors, which are similar to those of dwarf galaxies in the optical bands, as we also found for the polar structure in PRGs of our sample (see Fig.3.1 and Chapter 5). Furthermore, this component is almost undetectable in the NIR bands, as we already noticed for ESO 415-G26 in our sample (see Fig.2.1, top left panel and Fig.2.2, middle left panel). The presence of spiral arms in the ring and the low inclination respect to the equatorial plane of the central galaxy make ESO 235-G58 very similar to other *polar-ring-related* objects, such as *NGC 660* (van Driel et al. 1995). Moreover, this peculiar galaxy is characterized by an high amount of neutral hydrogen, mainly associated to the ring component, as also usually observed in almost all PRGs (see Sec.3.6): the total HI mass is about $3 \times 10^9 M_\odot$ (Buta & Crocker 1993; van Driel et al 2000). The total *baryonic mass* in the ring structure, i.e. stellar plus gas component, is about $9 \times 10^9 M_\odot$, which is about 3 times larger than the total mass of the stellar component in the central galaxy. Also for PRGs in our sample we have found that the ratio between the total baryonic mass in the ring and the stellar mass in the host galaxy is larger than the unity (see Tab.3.4 and Sec.5.4). This is one of the fundamental result which let us to consider the alternative ideas, discussed by Bekki (1998), for the formation of PRGs according to which these systems may be the result of a dissipational merger event, rather than of an accretion event[5]. In particular, also peculiar object in the class of PRGs like ESO 235-G58 and NGC 660 can be the result of a dissipative galaxy merging: as described by Bekki (1998) in Sec.3.2.3, such systems may be the transient morphologies of the ongoing merger during the time in which the intruder galaxy pierces the victim disk. Since the Bekki's model made some predictions also on kinematics of the two components, to derive more definitively conclusions on the nature of ESO 235-G58, we think that these observations need to be completed with high resolution spectroscopic data.

[5]In the accretion scenario (see Chapter1) one would expect the accreted baryonic mass (stellar + gas) to be a fraction of that in the pre-existing galaxy, and not viceversa.

Chapter 5

The puzzle of the Polar Structure in NGC4650A

NGC 4650A, in the Centaurus chain, is considered the prototype of the class of wide polar ring galaxies, because the two components are bright and well-defined (Whitmore 1991); see Fig.5.2. The central host galaxy was classified as an S0 with a blue filament running perpendicular to its major axis (Sèrsic & Agüero 1972): this is the polar ring, which is seen close to edge on. This component has a strong $H\alpha$ emission, implying recent vigorous star formation (Gallagher, Hunter & Tutukov 1984). Kinematic measurements indicate that the ionized gas forms a slightly warped disk with a central hole, in near-circular rotation (Laustsen & West 1980; Whitmore et al. 1987). The inner major axis of the polar ring lies within about 15^o of the apparent host galaxy minor axis, which is a typical characteristic in PRGs (Whitmore et al. 1990). The polar ring contributes about a quarter of the total galaxy's optical light, and the rest comes from the host galaxy (Whitmore et al. 1987; Sackett et al. 1994). The host galaxy is redder than the polar ring (Arnaboldi et al. 1995) and it is gas-poor. Spectroscopic observations (Schechter et al. 1984; Whitmore et al. 1987; Sackett et al. 1994) show that the ratio between the rotation velocity V and the stellar velocity dispersion σ is $V/\sigma \sim 1$, as expected in a rotationally-flattened oblate galaxy (Binney & Tremaine 1987); its $E6$ apparent flattening (Whitmore et al. 1987) is similar to a spiral galaxy bulge or the flattest elliptical galaxies of moderate luminosity (Nieto, Capaccioli and Held 1988).

As in the other polar ring galaxies, the polar structure in NGC 4650A is very rich in cool gas (see e.g. Richter, Sackett and Sparke 1994). For this object, new high-resolution 21-cm observations were carried out by Arnaboldi et al. in 1997 at the Australia Telescope Compact Array: the estimated total

HI mass in this system is 8×10^9 $M_\odot$, which is all associated with the polar component. The HI maps derived by Arnaboldi et al. (1997) barely resolved a central hole in the HI polar structure, which size is probably less than $10''$, and coincident with the host galaxy. These data strongly suggested that the polar material is distributed as a disk structure of considerable radial extent, rather than as a thin annulus. The atomic gas extends much further out than the ionized gas: most of the HI gas lies within $1.5'$ of the center, although filaments stretch $4'$ to the North and South, whereas the $H\alpha$ emission is found only within $1'$ of the central galaxy. In the light of these new results, Arnaboldi et al. (1997) concluded that the HI distribution and kinematics in NGC 4650A is consistent with the one commonly observed for an edge-on spiral disk. The spiral pattern proposed by Arnaboldi et al. (1997) seems to be confirmed by the recent HST image of NGC 4650A, acquired during the Heritage Project (Gallagher et al. 2001). These new data let to estimate the ratio $M(HI)/L_B \approx 5$ for the polar disk alone: this high value is typical of late-type or LSB galaxies (Matthews and Gallagher 1997).

To perform a detailed test of the formation scenarios for PRGs one needs to have data with the highest angular resolution, to resolve the inner central morphology of the polar ring and the central host galaxy, plus the NIR data, to probe the stellar population without the strong absorption caused by dust. Such a data set is now available for NGC 4650A and the aim here is to compare the predictions from different formation scenarios with the observational results from a study of the new NIR and high resolution HST data (Iodice et al. 2001). A distance of 41 Mpc based on $H_0 = 70$ km s^{-1}Mpc^{-1} and an heliocentric radial velocity $V = 2861$ km s^{-1}.

5.1 Observations

Here the near-IR (J, H and Kn bands) and the optical (B, V and I bands) observations obtained for the Polar Ring Galaxy NGC 4650A are presented. The morphology of the two main components, the host galaxy and the ring, are derived and discussed.

5.1.1 NIR observations

The near-infrared J, H and Kn images for NGC 4650A were obtained during two observing runs at the Mt. Stromlo and Siding Spring Observatory 2.3 m telescope with the CASPIR infrared camera (McGregor, 1994), with a field of view of $2'.0 \times 2'.0$ and an angular resolution of 0.5 arcsec per pixel (see

AppendixA). The observing log for these data is given in Tab. 5.1. Images were acquired with the offsetting mode and a cycle was defined containing 5 images on target plus 5 sky frames. Four cycles were obtained for J and H bands, and 8 cycles for Kn band were needed to have a better estimate of the background level. Linearisation, flatfielding, sky-subtraction and bad pixel correction were performed using the REDIMAGE task in the CASPIR package in IRAF. The resulting image for each cycle was derived by registering and combining all sub-frames. The final image in each band was obtained by stacking images from each set of cycles. Several standard stars, from Carter & Meadows (1995), were observed at the beginning, middle, and at the end of each night, in order to transform the magnitudes into the standard J, H and Kn band systems. The zero points that we derived are in good agreement with the indicative values derived for the CASPIR camera (see AppendixA) in each band; the differences in zero points were less than 0.1 mag. The ring in NGC 4650A is too extended to lie inside one single pointing, therefore it was necessary to take two different frames and mosaic them in a single image. The two pointings are reduced independently; before the final mosaic image was produced we checked that the two pointings have similar values of the background level. Fig. 5.1 shows the final Kn band mosaiced image. For the combined images in all bands, several tests were performed on the background noise. Compared with the pixel-to-pixel variation, we found that there is more noise, both within sky regions of moderate size and between such regions, than predicted by a pure counting (Poisson) model. Large scale variations in the background, due to an imperfect flatfield correction, contributed significantly to this "extra noise". For the areas within which we measured magnitudes and colors (see Sec.5.2 below), we derived an estimate of the "total" error of the flux enclosed within the polygons, from the statistics of the sky background in many sky boxes of comparable area. The *standard deviation for each pixel* is the standard deviation of the mean counts per pixel in each measured areas.

5.1.2 Hubble Space Telescope observations

NGC 4650A was observed with WFPC2 on the Hubble Space Telescope (HST) in April 1999, during the Hubble Heritage Project (Gallagher et al. 2001). The filters used are F450W, F606W and F814W, at optical wavelengths. Fig. 5.2 shows the final multicolor image of NGC 4650A from the HST press release. The observing log is listed in Tab. 5.2. Several frames were taken for each filter with different exposure times. During data reduction, different exposures were registered, scaled to the same exposure time and combined to obtain the

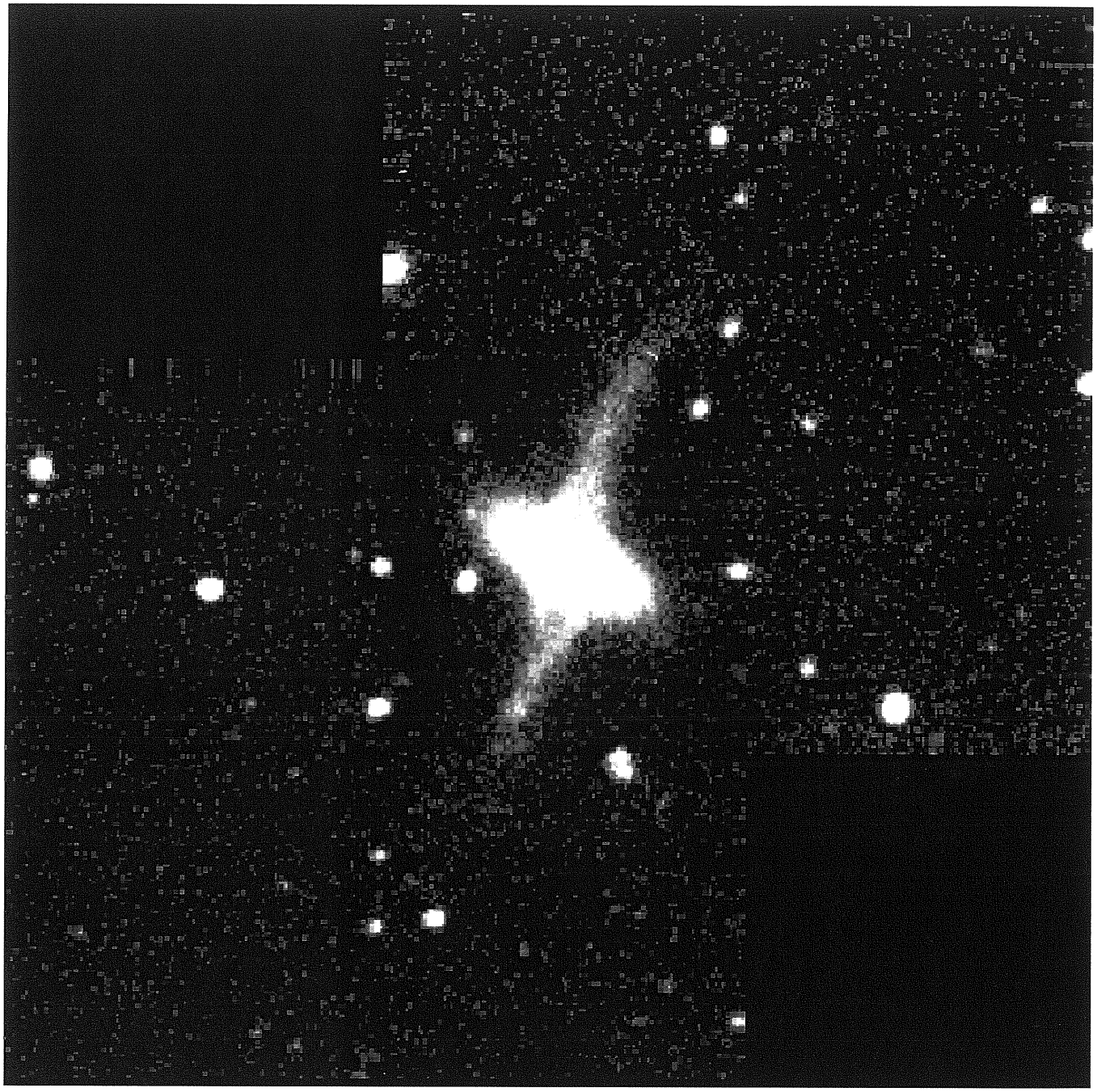

Figure 5.1: NGC 4650A in the Kn band, North is up and East is to the left.
The image size is $3'.1 \times 3'.0$.

Table 5.1: NIR observation log of NGC 4650A .

Filter	Tot. int. (s)	FWHM (")	Image field	Date
J	1200	1.3	1	21/03/1995
J	1200	1.3	2	21/03/1995
H	1200	1.5	1	20/03/1995
H	1200	1.4	2	20-21/03/1995
Kn	2400	1.4	1	20/03/1995
Kn	2400	1.4	2	20/03/1995

Table 5.2: HST observation log of NGC 4650A .

Filter	Tot. int. (s)	FWHM (")	n. exp.	Date
F450W	7500	0.24	8	04/1999
F606W	4900	0.31	6	04/1999
F814W	7600	0.28	8	04/1999

final image frame after cosmic rays removal. The magnitudes for the F450W, F606W, F814W filters were computed following Holtzman et al. (1995b). For each filter i_λ, these are given by

$$m(i_\lambda) = -2.5log(DN/s) + 2.5log(GR) + ZP[m(i_\lambda)] \quad (5.1)$$

where GR is the gain ratio, DN is the data number per second and $ZP[m(i_\lambda)]$ is the filter zero point, from Table 9 of Holtzman et al. (1995b): the observed zero point was adopted for the F814W filter and the synthetic zero point for the F450W and F606W filters. To convert the F450W, F606W, F814W magnitudes into the B,V,I standard system we used the relation derived by Holtzman et al. (1995b) for the F606W filter and in Matthews et al. (1999) for the F450W filter.

5.1.3 Host galaxy and polar ring morphology in the NIR and optical bands

The J, H and Kn images of NGC 4650A show that the host galaxy is the dominant luminous component, and its morphology resembles that of an early-type object, most likely an S0 (see Fig. 5.1). The high angular resolution of

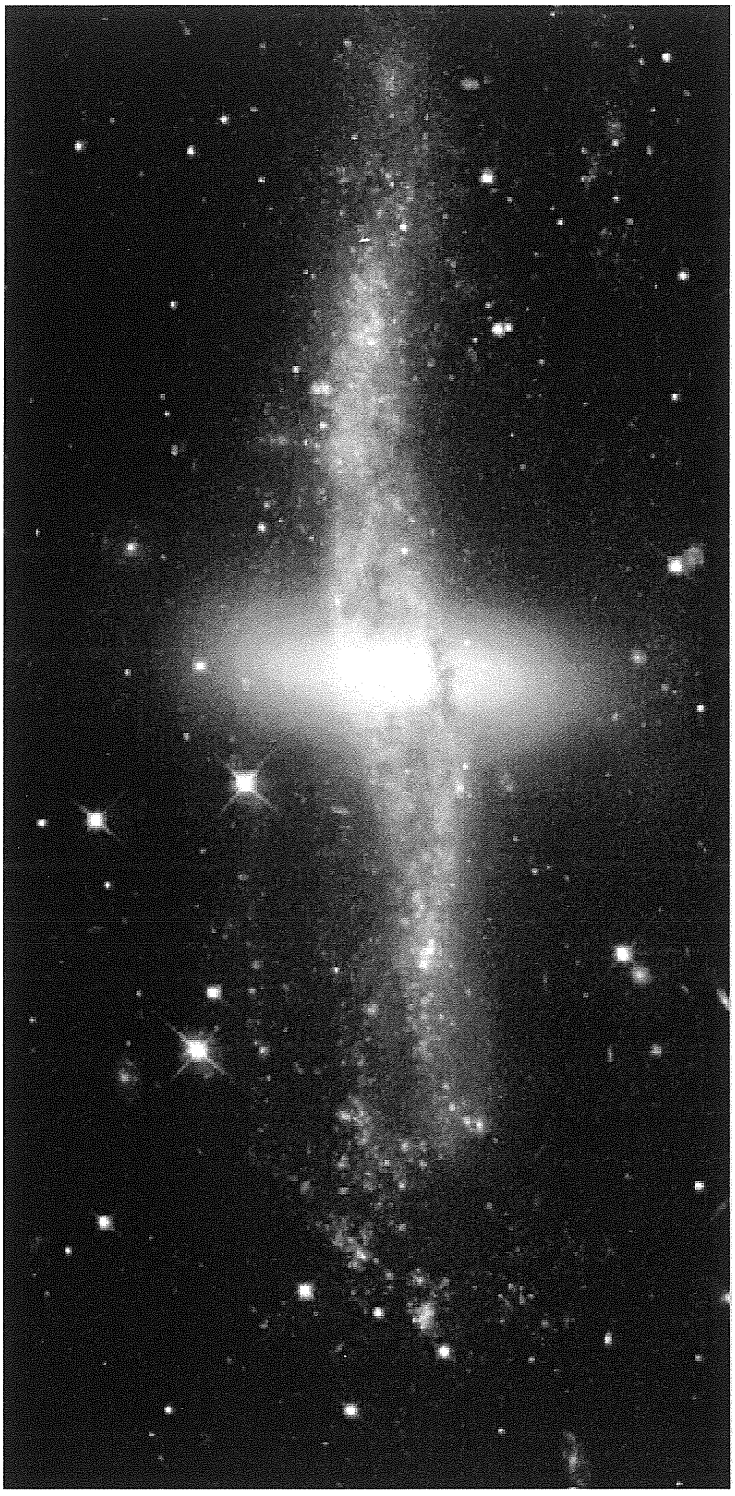

Figure 5.2: Color composite image of NGC 4650A from the HST Heritage program. The image size is $1'.3 \times 2'.7$. North is 20° counter clockwise from the y axis, East is 110° counter clockwise from the same axis, on the left side of the image.

the HST images allow a more detailed study of the inner regions of the polar ring and central spheroid: the main features stands out very clear in the multi-color image made by the Heritage Project and shown in Fig. 5.2. The light distribution associated with the host galaxy shows a very concentrated central component and a shallower, thicker envelope (see Fig. 5.2). The bulge to disk ratio (B/D) for this system will be discussed in detail in the following sections. The polar ring is more extended in the optical (B, V and I bands) than in the NIR, and it appears knotty and dusty. The new HST data (Gallagher et al. 2001) reveal the presence of young blue star clusters describing arches out of the main polar ring plane, along the SE and NW directions of the main light distribution, and outline the two spiral arms noted by Arnaboldi et al. (1997), see (Fig. 5.2. The un-sharp masked version of the final combined image is produced for all NIR and optical bands to identify the inner features of the central component and those related to the polar ring. The un-sharp masked images are obtained as ratios between the final galaxy frame and its median filtered image (computed with the FMEDIAN package in IRAF): this ratio represents the "high-frequency residual image". In the NIR median filtered images, each original pixel value is replaced with the median value in a sliding rectangular window. The window size (7×7 pixels) was chosen to provide the optimum enhancement of the S0 inner structures. The left panel of Fig. 5.3 shows the high-frequency residual image in the H band. An edge-on disk is readily identified by comparing its thickness with the average FWHM of foreground stars. Furthermore the high-frequency residual images reveal an 'S'-shaped filamentary structure which connects the outer parts of the polar ring and runs across the nucleus of the system, along the NW and SE directions. This luminous structure becomes more evident in the H (Fig. 5.3) and Kn bands than at visible wavelengths: in the optical bands the light is strongly affected by dust absorption in this region. As the stellar disk is seen nearly edge-on, this structure cannot be a bar in the S0 plane. Since the resolution of the HST data is higher (1 pixel = 0.1 arcsec) than in the NIR, the filtered images in the optical bands are computed using a larger window (35×35 pixels). The right panel of Fig. 5.3 shows the V band high-frequency residual image. This image shows an edge-on disk, which becomes warped in the outer parts, and the dark clouds associated with the polar ring extend right to the center of the system; there is no central hole which is totally empty. The NIR and optical HST data are so far consistent with the central component being a *puffy* stellar disk, seen edge-on and slightly warped in the outer parts, and there is no central hole in the polar ring dust and/or light distribution at small radii.

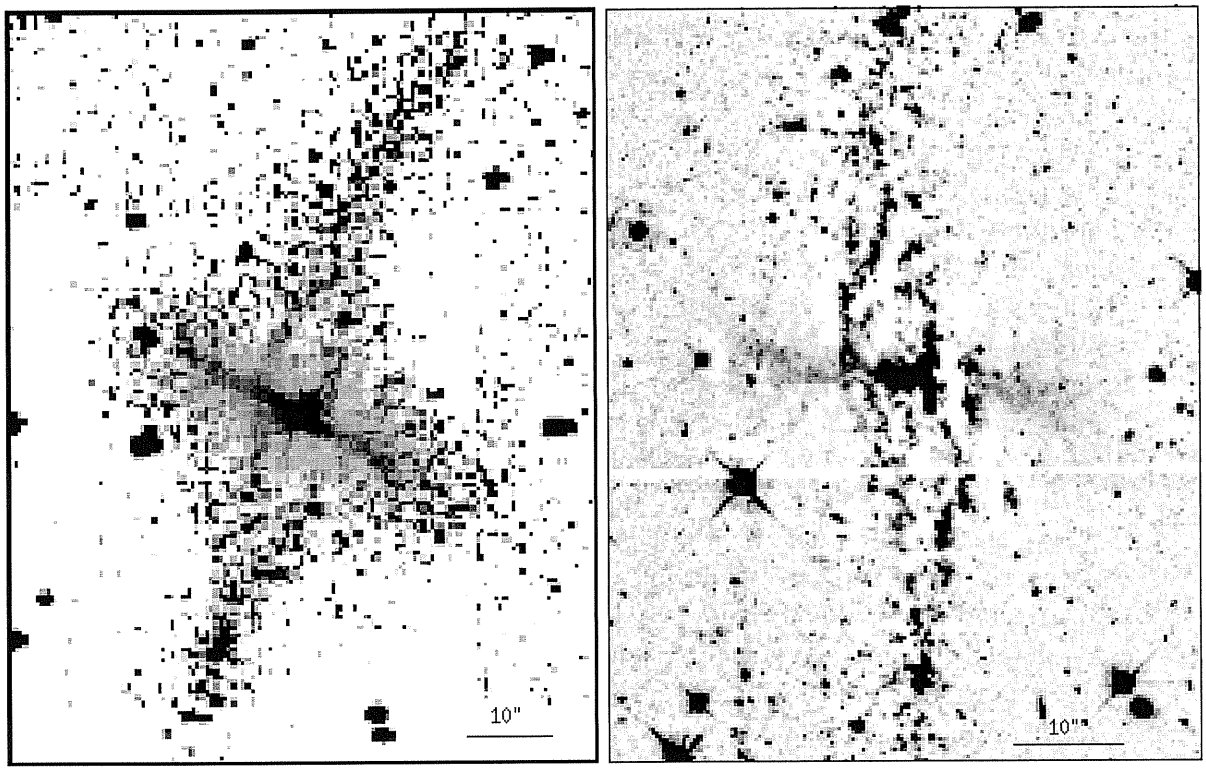

Figure 5.3: Morphology of the Polar Ring structure: high-frequency residual image in the ground-based H band (left panel) and in the HST V band (right panel). Units are intensity; in the H band image North is up and East is to the left, in V band image North is 20° counter clockwise from the y axis, East is 110° counter clockwise from the same axis, on the left side of the image.

5.2 Photometry

Integrated magnitudes and colors are computed for the two main components of NGC 4650A, host galaxy and ring. The structural parameters are derived from the modeling of the surface brightness distribution.

5.2.1 Total magnitudes

The integrated magnitudes are computed in B,V,I and J,H,Kn for the whole system and in five different areas. These areas are chosen as follows: one is coincident with the nucleus; two areas, SW and NE of the nucleus, are placed within the host galaxy stellar component (outside the nucleus, in regions unperturbed by the polar ring), and two areas for the polar ring, NW and SE of the galaxy center; see Fig. 5.4 for a complete summary. The polygons are determined from the J image (using the IRAF task POLYMARK) and used for all bands, after the images were registered and scaled to the J image. The integrated magnitudes inside each polygon are evaluated using the IRAF task POLYPHOT. The photometric errors take into account both statistics and background fluctuations. In the NIR bands, the error relative to the integrated magnitude in each area is given multiplying the standard deviation per pixel (defined in Sec.5.1.1) by the number of pixels in that area. The average error on integrated magnitudes is about 0.06 mag, which led to a 20% error on colors. In the optical, the error estimate includes also the uncertainties on the transformations to the standard B, V and I bands, and the average error on integrated magnitudes is about 0.04 mag, which led to a 13% error on colors. The integrated magnitudes and colors corresponding to each area are listed in Table 5.3 and they have been corrected for extinction within the Milky Way, using $A_B = 0.485$ from Schlegel et al. (1998).

5.2.2 Light and color distribution

In Fig. 5.5 and Fig. 5.6 the luminosity profiles are plotted for the major axis (left panels) of the S0 and polar structure (right panels), in the NIR (JHK) and optical (BVI) bands. The absorption due to the dust in the polar ring which passes in front of the central galaxy does perturb the J and optical profiles for this component at about 5 arcsec, SW of the galaxy center. The polar ring shows a prominent *S-shape*, quite evident in the NIR (Fig. 5.1): because of this morphology, the polar ring light profiles are the result of an average of several profiles extracted in a cone, centered on the S0 and 10 degree wide ($\pm 5°$ from

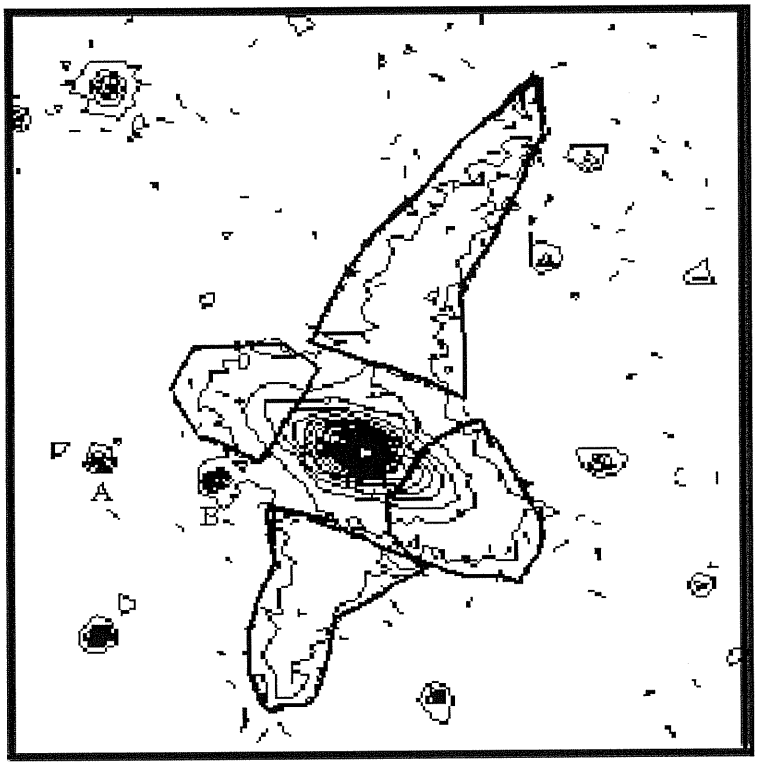

Figure 5.4: NGC 4650A contour plot in the J band plus the 5 polygons limiting the different areas where the integrated magnitudes are computed. The distance between the two stars (A and B) is about 28 arcsec. North is up and East is to the left.

the $P.A. = 162°$ of the ring major axis). The presence of young star clusters, HII regions and dust is responsible for several bumps in the optical profiles (Fig. 5.6), which appear less regular than those in the NIR (Fig. 5.5).

The J-H and H-K color maps are shown in Fig. 5.7. The SW side of the host galaxy is strongly perturbed by the polar ring dust, while the NE side has approximately constant colors. The two sides of the polar ring do not show significant differences in the J-H colors, while the NW side seems to be bluer than the SE side in the H-K color.

Table 5.3: Integrated magnitudes and colors of different regions of S0 and of polar ring.

Region	m_B	M_B	m_J	M_J	B-V	V-I	B-H	J-K	J-H	H-K
PR (SE)	16.38	-16.7	15.46	-17.6	0.29	0.71	1.39	0.79	0.47	0.32
PR (NW)	15.90	-17.2	15.01	-18.0	0.23	0.71	1.37	0.68	0.49	0.20
S0 (SW)	16.72	-16.3	14.73	-18.3	0.87	1.07	2.52	0.76	0.53	0.23
S0 (NE)	17.21	-15.8	15.35	-17.7	0.85	1.06	2.46	0.88	0.60	0.28
center	15.4	-17.6	13.30	-19.8	0.87	1.15	2.80	0.94	0.66	0.28

5.2.3 Two-dimensional model of the S0 light distribution

The 2D model of the S0 light distribution is done in the Kn and in the I band, because the effect of dust absorption is weaker in these bands. In the I band, the dust in the polar ring arm does absorb the S0 light, as we outlined in Sec.5.2.2. The regions affected by this strong absorption are not taken into account in the fitting routine: those symmetric with respect to the galaxy center were used instead. Moreover the regions affected by foreground stars, and by the polar ring light along the S0 minor axis, are accurately masked before performing the fit to the light distribution. The light distribution of the S0 galaxy was modeled[1] through the super-position of a spheroidal central component, which projected light follows the generalized de Vaucouleurs law (Eq.3.1), and an exponential disk (Eq.3.2), as described in Sec.3.3.

Fig. 5.8 shows the comparison between the observed and calculated light profiles in the Kn band (left panel) and in the I band (right panel). The structural parameters are listed in Tab. 5.4. This model is fitted to the light distribution of the S0 in such a way that there are no negative residuals, i.e. this is the "minimum" model of the S0 light in the Kn and in the I bands. The S0 models in the J and H bands, and in the B and V bands, are simply scaled versions of the Kn and I band models respectively, based on the average colors of the stellar component (see Sec.5.2.1). The photometric errors do take into account the photon statistics and background fluctuations (see Sec.5.1.1). Fig. 5.9 shows the ratio between the image for the whole galaxy and the S0

[1]This is the same fitting model adopted to study the host galaxy light distribution in PRGs, and a detailed description is given in Sec.3.3.

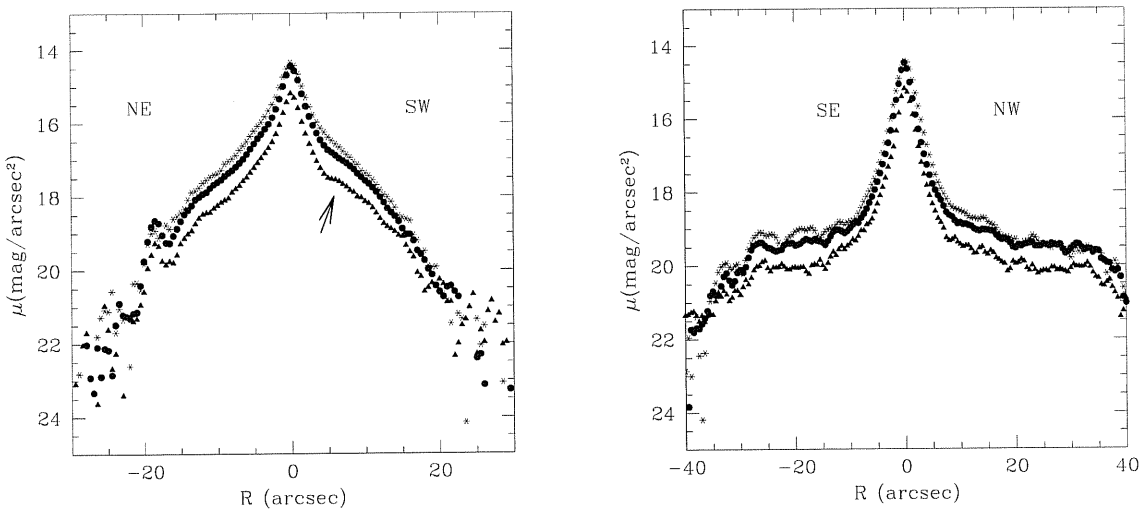

Figure 5.5: Left panel - NIR surface brightness profiles along the S0 major axis, at $P.A. = 62°$. The arrow indicates the absorption dip caused by the polar ring on the central spheroid. Right panel - surface brightness profiles along the polar ring major axis, at $P.A. = 162°$. The code for symbols is: J band full triangles, H band full dots, and Kn band asterisks.

model, which is computed in the H band (left panel) and in the V band (right panel). We see that the central galaxy is a stellar disk which has a warp in the outer parts. The bright features near to the galaxy center connect the outer parts of the polar ring and the nucleus of the system, i.e. the residual from the 2D modeling in the optical and NIR confirm that there is no central empty hole at small radii in the polar ring light distribution. The value for the apparent q_d ratio of the S0 disk is ~ 0.5, which is larger than what one would expect for an edge-on disk. This is caused by the warp present in the S0 disk which makes the isophotes more boxy in the outer parts and therefore produce a larger q_d value.

5.2.4 Scale parameters for the S0

The study of the host galaxy light distribution and its structural parameters will help to understand whether this component is really a standard early-type system. The optical light distribution in the host galaxy central regions

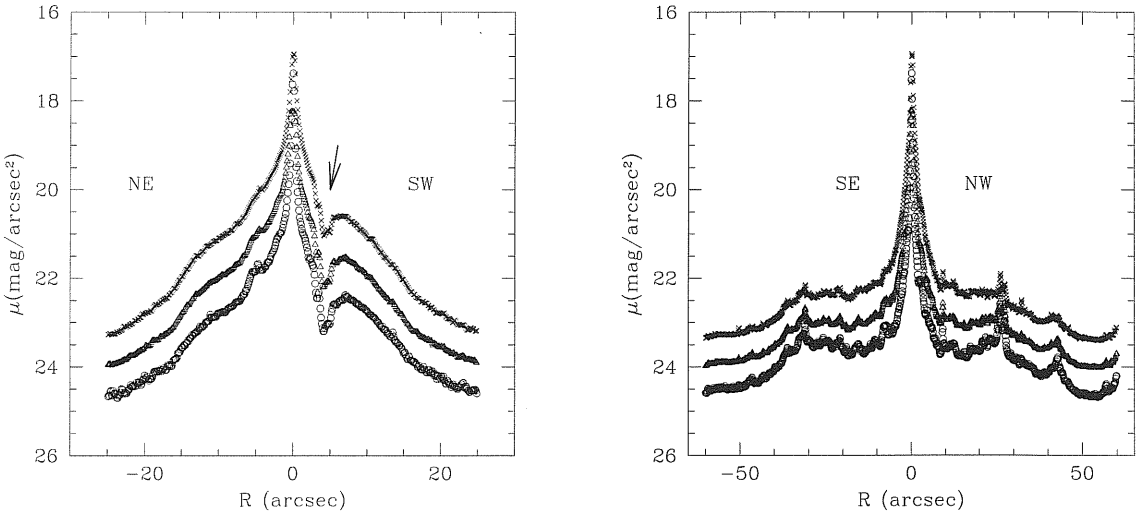

Figure 5.6: Left panel - optical surface brightness profiles along the S0 major axis, at $P.A. = 62°$. The arrow indicates the absorption dip caused by the polar ring on the central spheroid. Right panel - optical surface brightness profiles along the polar ring major axis, at $P.A. = 162°$. The code for symbols is: B band open dots, V band open triangles, and I bands crosses.

has a quasi-exponential behavior: the value of the n exponent, in Eq.3.1, is about 1, and the light is very concentrated toward the center, as the small value of the effective radius suggests. The convolution of this bright nuclear light concentration with the PSF on ground based images may have caused a smoothing of the light profiles toward the center, leading to a spuriously larger value for r_e and a smaller value for the n exponent in the NIR S0 model respect to the I band one. The scale parameters for the central spheroid in NGC 4650A are compared with those obtained by Bothun and Gregg[2] (1990) for a sample of early-type galaxies, and with those obtained for the PRGs (Sec.3.3.2) and for ESO 235-G58 (Sec.4.6). Fig.5.10 (left panel) plots the location of the bulge in the host galaxy of NGC 4650A in the plane of effective parameters μ_e and

[2]The structural parameters for early-type galaxies where obtained, in the B band, by fitting the light distribution with the super-position of a de Vaucouleurs' law ($n = 4$) and an exponential disk, for the bulge and disk component respectively. The surface brightness parameters in the K band are derived by taking into account the average B-K color of these objects (Bothun and Gregg, 1990).

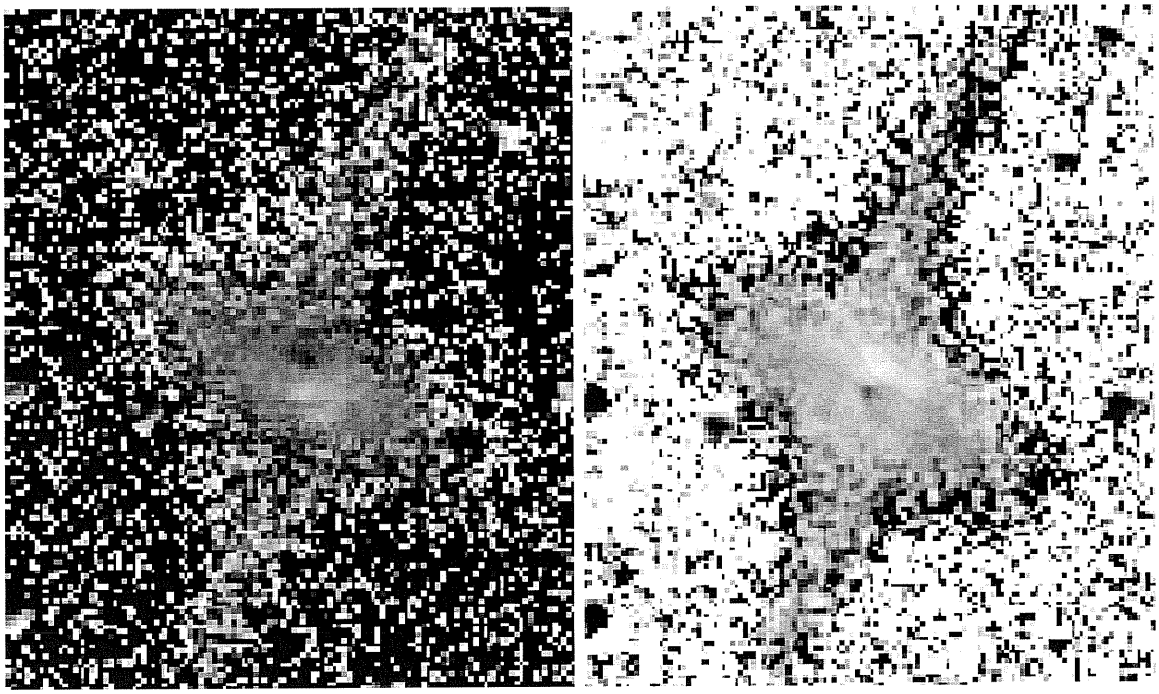

Figure 5.7: J-H (left panel) and H-K (right panel) color maps. North is up and East is to the left. Color code in each map is: darker = bluer, whiter = redder in the color.

r_e: as the other PRGs (but AM2020-504, see Sec.3.3.2), also NGC 4650A is characterized by a very compact bulge. In the $log(n) - log(r_e)$ space (right panel of Fig.5.10), the bulge parameters for NGC 4650A do not fall in the same area occupied by early-type galaxies (by Caon et al., 1993)[3], but it lies in the same range of values derived for PRGs and where dwarf galaxies (by Davies et al. 1988) are also found. The host galaxy in NGC 4650A, as in the other PRGs, is characterized by a very centrally peaked and nearly exponential bulge. Also the host galaxy's disk shows, in the Kn band, similar characteristics to the other PRGs of the selected sample (Sec.3.3.2): this component has an higher central surface brightness and a smaller scalelenght than the average values observed for S0 galaxies (see Fig.5.11, left panel). The disk scalelength in the I band is about 1 arcsec larger than in the Kn band, which may suggest that there could be a difference in the stellar population of the S0 disk as function of radius. The B/D ratios in the I and Kn bands are very small: $B/D = 0.107$

[3]The n exponents derived by Caon et al. (1993) are those along the minor axis of the system, in order to exclude the contribution from a possible disk component.

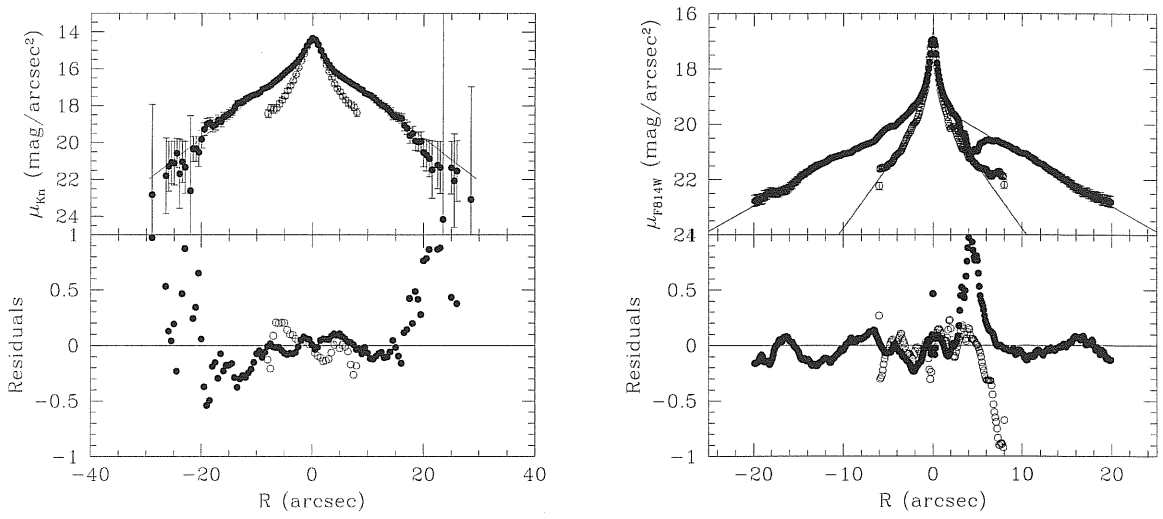

Figure 5.8: Left panel - Fit of the S0 2D model to the light profile in the Kn band to the major (filled dots) and minor axis (open dots). Right panel - Fit of the S0 2D model to the light profile in the I band for the major (filled dots) and minor axis (open dots).

in the I band and $B/D = 0.122$ in the Kn band; as also found for the other PRGs (Sec.3.3.2), the B/D ratio is smaller than the typical values expected for standard S0 galaxies (see Fig.5.11, right panel).

5.2.5 Study of the light distribution in the polar structure

Because of the polar ring morphology in the optical, the luminosity profile along the polar ring major axis is computed as averages of 20 extracted profiles, parallel to P.A. = 162°, and the final profile is obtained as average of the two sides opposite to the nucleus. The polar ring light profiles are well reproduced by an exponential law and the comparison between the observed average profiles and the relative best fit is shown in Fig. 5.12. The polar ring scalelength decreases from the optical to the NIR bands, i.e. the polar ring is more extended in the optical than in the NIR, and may also suggests the presence of different stellar populations: an older inner component and a more extended, younger, one. In Fig. 5.13 the average absolute magnitude and the

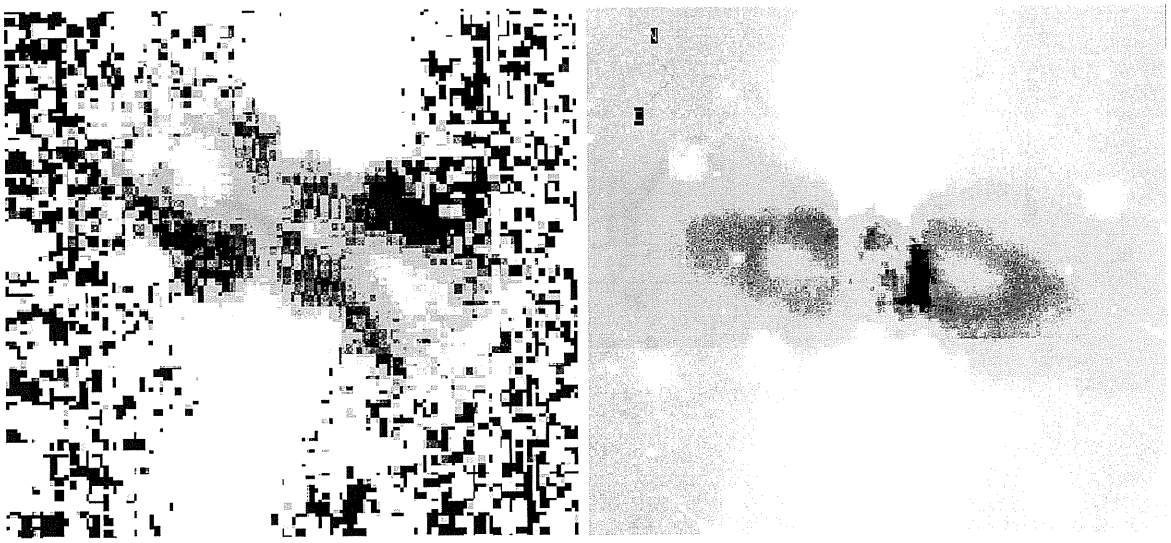

Figure 5.9: Residual image obtained as the ratio between the whole galaxy frame and the 2D model for the S0 in the H band (left panel) and in V band (right panel). Details on image processing and 2D modeling of the light from the central component are discussed in Sec.5.2.3. Units are intensity; whiter colors correspond to those regions where the galaxy is brighter than the model, darker colors corresponds to those regions where the galaxy is fainter than the model. In the H band image North is up and East is to the left, in V band image North is 20° counter clockwise from the y axis, East is 110° counter clockwise from the same axis, on the left side of the image.

scalelenght of the polar structure are compared with the typical values for a sample of spiral galaxies (by de Jong & van der Kruit, 1994), in the Kn band, and with a sample of LSB (by Bergvall et al. 1999), in J band: the polar structure in NGC 4650A seems to have the typical extension of a spiral galaxy, even if it is less luminous. On the other hand, this component seems to be larger and brighter than the LSB galaxies.

An important quantity related to the size of the polar ring is the moment of its radial distribution

$$(\Delta R)^2 = \frac{\int_{r_e}^{\infty}(r-\bar{R})^2 * \mu(r)dr}{\int_{r_e}^{\infty}\mu(r)dr} \tag{5.2}$$

where $\bar{R}$ is the average radius

$$\bar{R} = \frac{\int_{r_e}^{\infty} r * \mu(r)dr}{\int_{r_e}^{\infty}\mu(r)dr} \tag{5.3}$$

Table 5.4: Structural parameters for the host galaxy in NGC 4650A. The effective surface brightness μ_e and the central surface brightness μ_0 are in $mag/arcsec^2$, and μ_0^c is corrected for the inclination. r_e and r_h are respectively the effective radius and disk scalelength derived in arcsec, the corresponding values expressed in kpc are derived by using $H_0 = 70 \mathrm{kms}^{-1}\mathrm{Mpc}^{-1}$. Third and sixth columns list the absolute errors derived by the fit routine.

P	Kn band	δ	kpc	I band	δ	kpc
μ_e	15.89	0.08		18.86	0.05	
r_e	1.41	0.04	0.3	0.71	0.02	0.1
μ_0	15.12	0.04		19.27	0.02	
μ_0^c	15.79	0.06		20.24	0.04	
r_h	4.7	0.1	0.9	5.92	0.07	1.2
q_b	0.99	0.01		0.96	0.01	
q_d	0.54	0.01		0.46	0.01	
n	0.57	0.11		1.22	0.04	
B/D	0.122	0.005		0.107	0.003	

weighted by the surface brightness distribution and r_e is the effective radius of the central component. For a pure exponential disk, the $\Delta R/\bar{R}$ ratio tends to unity when r tends to infinity. For a real object, this value is expected to be less than 1, because of its finite extension. This is confirmed by the $\Delta R/\bar{R}$ values derived for a sample of spiral galaxies (de Jong 1996) in the B band: this quantity varies from 45% to 75% and the average value is $\Delta R/\bar{R} \sim 65\%$. In the B band, the polar structure in NGC 4650A and spiral galaxies in the de Jong sample have similar scalelengths (for spirals $13 \leq r_h(\mathrm{arcsec}) \leq 65$, with an average value of about 25 ± 11 arcsec). The polar ring is less luminous than typical spirals (see Table 5.3,) so the $\Delta R/\bar{R}$ for the polar ring is going to be smaller than the average value obtained for spiral galaxies. This value is computed for the I band (which is less disturbed by dust absorption) and gives $\Delta R/\bar{R} \sim 50\%$. The structural parameters of the light distribution and its extension suggest that the polar structure is more similar to a disk than a to an annular ring.

5.3 Using colors to date the stellar populations of NGC 4650A

One wishes to compare the integrated colors of the main components (host galaxy and polar structure, shown in Table 5.3) with those of standard morphological galaxy types, and check whether differences in colors are related to dust absorption or to different stellar populations.

NIR colors - The NIR colors of the central spheroid and the polar structure are compared with those of (1) standard early-type galaxies in the Fornax and Virgo clusters (Persson et al., 1979), (2) spirals (Giovanardi & Hunt, 1996; Frogel, 1985; de Jong & van der Kruit, 1994), (3) dwarf ellipticals (Thuan, 1985), and (4) low surface brightness galaxies (Bergvall et al. 1999). The J-H vs. H-K plot in Fig. 5.14 (left panel) shows that the nucleus of the central component is redder than its outer regions and falls in the area occupied by early-type galaxies. The other two regions show bluer colors and are close to the area identified by the dwarf galaxies. The color gradient through the host galaxy spheroid may be accounted for by the reddening due to the dust, as indicated by the reddening vector computed for a screen model approximation and $A_V = 0.3$ (Gordon, Calzetti & Witt 1997). On average, the polar ring is bluer than the central galaxy. There is an additional color difference between the two regions of the polar ring: the South side of the polar structure has a redder H-K color with respect to the North side, which cannot be accounted for by the reddening vector alone. It may be caused by a different dust distribution and high scattering in the two regions of the polar ring: the screen model is inadequate to describe it.

Optical colors -The B-V vs. V-I colors for the S0 component and the polar ring (Fig. 5.14, right panel) are compared with those of (1) standard early-type galaxies (Michard & Poulain 2000), (2) spiral galaxies (de Jong & van der Kruit, 1994), (3) dwarf galaxies (Makarova 1999), (4) LSB galaxies (O' Neil et al. 1997; Bell et al. 2000). The optical colors of the host galaxy appear very similar to those of early-type objects. If one accounts for a reddening caused by the dust in the polar ring, in the screen model approximation, the colors of the central spheroid will fall in the region for late-type systems. The reddening due to dust can also account for the color gradient between the center and outer regions along the polar ring major axis. On the other hand, the difference between the integrated colors of the polar structure and those of the central component cannot be accounted for by the reddening vector alone: such a large gradient is more likely due to a difference in stellar populations.

The stellar population synthesis model by Bruzual & Charlot (1993) were

used to reproduce the integrated colors of different regions (see Sec.5.2.1) in the polar ring galaxy NGC 4650A. The goal is to derive an estimate of the stellar population ages in the central spheroid and the polar structure. As a first step, we selected a set of models which were able to reproduce the average integrated colors of galaxies with different morphological types in the local Universe, and then they were optimized to reproduce the colors observed for the two main components of NGC 4650A, in particular the B-H and J-K colors. The B-H vs. J-K diagram is used to break the age-metallicity degeneracy, as suggested by Bothun et al. (1984). The J-K color is a good estimate of the metallicity and it is quite insensitive to the presence of a young stellar population. This is supported by the observed monotonic increase of the mean J-K color in globular clusters with increasing metallicity (Aaronson et al. 1978, Frogel et al. 1983), and the population synthesis models by Bothun (1982) show that J-K is decreased only by 0.05 mag as a result of a starburst, while the B luminosity is increased by 1 mag. On the other hand, the B-H color is sensitive to the combined effect of SFR, metallicity and age (Bothun et al. 1984). Fig. 5.15 shows that the central component is overall bluer in the B-H color than the average values for early-type galaxies, so a younger age is to be expected. The polar structure is significantly bluer than the central galaxy, implying even a younger age for its stellar population.

A star formation history with an exponentially decreasing rate was adopted for the central component. It has the following analytical expression: $SFR(t) = \frac{1}{\tau}\exp(-t/\tau)$, where the τ parameter quantifies the "time scale" when the star formation was most efficient. Adopting $\tau = 1$ Gyr and $\tau = 7$ Gyr, the correspondent evolutionary tracks were derived for different metallicities ($Z = 0.0004$, $Z = 0.008$, $Z = 0.02$, $Z = 0.05$, $Z = 0.1$), which were assumed constant with age. As shown in the left panel of Fig. 5.15, these models reproduce the photometric properties of early-type galaxies in the local Universe. A constant star formation model (with metallicities: $Z = 0.0004$, $Z = 0.008$, $Z = 0.02$, $Z = 0.05$, $Z = 0.1$) which reproduces the integrated colors of local spiral galaxies (right panel of Fig. 5.15) was used for the polar structure. In every model it has been assumed that stars form according to the Salpeter (1955) IMF, in the range from 0.1 to $125M_{\odot}$. The lines of constant age were computed from the evolutionary tracks and suggest an age between 1 to 3 Gyr for the central component (left panel of Fig. 5.15), has an overall younger age than the typical ages of an early-type system. The age derived for the polar structure is less than 10^8 yr (see right panel of Fig. 5.15). A cautionary note: our derived colors are all upper limits, since they were not corrected for the absorption caused by the dust in the polar structure and indeed the true

colors of the central stellar component might be even bluer. Furthermore, the age estimates for the central component and the polar structure are uncertain because we lack independent information on the star formation law and metallicity of the stellar population in the central host galaxy and polar structure. The intrinsic uncertainties of the synthesis population models must also be considered, particularly for the age of the central component. By comparing three recent synthesis codes, Charlot, Worthey and Bressan (1996) found that the colors predicted for old populations with an age > 1 Gyr, plus same input age and metallicity, are affected by discrepancies, which are primarily due to the different prescriptions adopted for the stellar evolution theory. Thus, our estimates are only indicative of the relative ages between the central host galaxy and polar structure.

5.4 Constraints on the formation scenario for NGC 4650A

We have presented a detailed photometric study of polar ring galaxy NGC 4650A, based on new NIR observations and high resolution optical imaging acquired with the HST. We now wish to compare our results against the properties predicted for PRGs in different formation scenarios, described in Chapter1 and summarized in the following. Possible scenarios for polar ring formation can be grouped into two main pictures, i.e 1) accretion of a gas-rich dwarf galaxy by an early-type system or gas stripped from a nearby gas-rich object, and 2) a major dissipative merging of two disk galaxies. Accretion in, or gas-stripping by, an oblate/triaxial galaxy can predict the formation of a narrow polar annulus. These annuli can be in a quasi-equilibrium configuration if 1) their ratio $\Delta R/\bar{R}$ is between 10% and 30%, where ΔR is the radial extension of the ring and $\bar{R}$ the average radius (Katz & Rix, 1992; Christodoulou et al. 1992; Reshetnikov & Sotnikova, 1997) and 2) self-gravity is at work (Sparke 1986, Arnaboldi & Sparke 1994). The total amount of accreted gas can be of the order of $10^9 M_\odot$, which is the typical amount of HI in a gas-rich dwarf (Carignan 1999). The process of ring formation through accretion/stripping of a gas-rich companion takes few Gyrs at most. In this scenario the host galaxy is an early-type gas-free system and preserves its structure (luminosity profile, B/D ratio, scale parameters), while some star formation is triggered by the event (Arnaboldi et al. 1993).

The merging scenario of two disks can account for the formation of narrow rings as well as of wide/massive disk-like structures, depending on the initial

mass ratio of the two merging progenitors. According to this scenario, the polar structure represents what remains of the "victim" disk galaxy, while the accreted "intruder" has supplied the S0-like component. Polar rings are more likely to form when the two disks encounter each other on a polar orbit, with a small initial orbital angular momentum (Bekki 1998). This dissipative merger event transforms the intruder's thin stellar disk into a thicker structure. Both intruder's and victim's disk radial mass distribution deviates from the initial exponential profiles as the merger process goes on. When extended polar structures are formed (depending on the intruder/victim mass ratio), they are characterized by the absence of a hole in the central regions, and their HI content can be as large as that of late-type spirals, i.e. up to $10^{10} M_{\odot}$. The predicted evolution time for the whole resulting polar ring galaxy is of about 10^9 yr, and the outwardly propagating gaseous waves, excited by the intruder galaxy, trigger a burst of stellar formation in the polar disk.

What are the observational properties of the polar ring galaxy NGC 4650A? Can they discriminate between the two scenarios? Both in the NIR and HST images, we have found that stellar light and dust lanes connect the outer parts of the polar structure with the inner central nucleus of the system, i.e. this component does not show a completely empty central hole. The light distribution of the polar structure follows an exponential profile and has a $\Delta R/\bar{R} \sim 50\%$. These properties suggest that this structure is more similar to a disk rather than a narrow annulus, as already suggested by Arnaboldi et al. (1997) through the analysis of the HI distribution in the polar structure. Furthermore, the HI observations for NGC 4650A showed that the total HI mass in this component is about $10^{10} M_{\odot}$. The high resolution HST images indicate that the central spheroidal component is not a standard early-type system. It has a small exponential bulge and a disk with an exponential profile, which appears slightly warped in the outer regions. This warp is observed both in the optical and in NIR. The study of the integrated colors of NGC 4650A has shown that polar structure is much bluer than the stellar central component, as it is also visible in the beautiful HST multicolor images. The comparison with the predicted colors from stellar population synthesis codes suggests a very young age (< 0.5 Gyr) for the polar structure. The age of the central component is in the range of 1 to 3 Gyr, which is of a significantly younger age than those typical for early-type galaxies.

Whatever event may have occurred in the past of NGC 4650A, it has strongly changed the properties of the host galaxy, both in the structure and stellar population, so that this component differs from a standard S0 system. Published simulations of the accretion/stripping scenario were not able to re-

produce either these observed properties for the host galaxy in NGC 4650A, or those for the polar structure. In particular, we note the absence of a hole in the center of the polar disk, which has an exponential light distribution and a large amount of HI, which is an order of magnitude larger than what is expected in the accretion models. Furthermore, for reasonable mass-to-light ratios ($M/L \sim 2$ in the NIR, from Matthews, van Driel and Gallagher 1998), the luminous mass (gas plus stars) in the polar structure, of about $12 \times 10^9 M_\odot$, is comparable with or even higher than the total luminous mass in the host galaxy, of about $5 \times 10^9 M_\odot$. In the accretion scenario, one would expect the accreted baryonic mass (stellar + gas) to be a fraction of that in the pre-existing galaxy, and not viceversa, as it is observed for NGC 4650A. Based on these new observational results, we have considered the alternative ideas discussed by Bekki according to which the polar ring galaxies, such as NGC 4650A, may have formed from a dissipational merger event of some kind. The dissipative merger scenario proposed by Bekki (1998) may provide a coherent explanation for the wide and massive polar disk of NGC 4650A and its larger baryonic mass content with respect to the central component, plus the non-standard properties of the light distribution in the central S0-like component. A future test of Bekki's scenario for PRG formation should also include a detailed analysis of the kinematics predicted from the N-body simulations and a comparison with PRG kinematics, and address the question about the stability of those merger configurations which lead to the formation of a massive disk.

5.5 Dark Matter content in NGC4650A

The dynamics of PRGs has been used to put limits on the 3-D shape of dark matter halos and may give further hints on the formation mechanisms of these structures. The question of the dark halo shape is important because cosmological simulations (Navarro, Frenk and White 1996; 1997) predict the distribution of the halo shapes and the universal radial dependence of the matter distribution in the dark halos. In view of these applications, the PRG NGC 4650A becomes a powerful laboratory as the HI distribution samples the potential field as far as 40 kpc from the center of the host galaxy. By deriving the most likely dark halo flattening distribution from the polar ring dynamics, tests can be performed on the likelihood of the different cosmological models.

The first attempts to derive the dark halo shape in polar ring galaxies were made by Schweizer, Whitmore & Rubin (1983) and Whitmore, McElroy & Schweizer (1987). By comparing the ratio between ring and disk speeds at

the same galactocentric radius, they derived a wide range of flattenings for the mass distributions. Among the objects studied, the prototype polar ring galaxy NGC 4650A has been the best investigated. In their work, Whitmore et al. (1987) concluded that the dark matter halo for this object was spherical. On the other hand, the analysis of the S0 and outer polar ring rotation curve, led Sackett & Sparke (1990) to conclude that the observed kinematics was well reproduced by adopting dark halo flattenings in the range E3-E7. Sackett et al. (1994) proposed a dynamical model, based on the observations of the rotation and velocity dispersion of the central disk obtained at the ESO 3.6m telescope, which ruled out the spherical dark halo. Their best fit model was given by a dark halo with an E6 to E7 flattening, whose axis are aligned with those of the S0. In 1996, the observed similarities between the wide polar rings and the late-type spiral disks let Combes & Arnaboldi (1996) to develop a radically different dynamical model for NGC 4650A. By knowing that i) the HI component lies entirely in the polar ring (van Gorkom et al. 1987), ii) their B-R and R-K integrated colours are very similar to those of late-type systems (Arnaboldi et al. 1995), and iii) that there is an empirical relationship between the dark matter and the HI surface density (Bosma 1981; Freeman 1993), F. Combes and M. Arnaboldi proposed a dark component flattened in the plane of the polar ring itself.

The biggest uncertainties in the mass model proposed till 1996 for the dark halo shape were related to the low resolution 21-cm observations available at that time and the velocity dispersion profile along the major axis of the lenticular galaxy. The velocity dispersion measured by Sackett et al. (1994) in the outer parts of the S0 at radii $r \geq 18''$ and $\mu_I \geq 22$ are affected by large error bars (nearly 200% of the value measured): due to these large error in the measurements, the kinematical data can be reproduced by both low (10 km/s, Combes & Arnaboldi 1996 model) as well as high (40 km/s, Sackett et al. model) values for the radial velocity dispersion, and this allows agreement with a large variety of dark halo shape. The S0 velocity dispersion at large radii requires a precise determination to constraint the range of dark halo flattenings, and these data are not available yet. Whereas, new high resolution 21-cm observations were obtained by M. Arnaboldi, T. Oosterloo, K.C. Freeman, F. Combes (1997) with the Australia Telescope Compact Array for a sample of polar ring galaxies, including also NGC 4650A. These were meant to resolve the rotation curve at small radii, where velocities were measured into two planes, the polar ring and the host galaxy equatorial plane, and to reach out at larger distances into the halo. As emphasized in the introduction to this Chapter, by these observation was derived a new value for the total HI

mass, 8×10^9 $M_\odot$, that is two times higher than the total mass of 4.6×10^9 $M_\odot$ measured by the old observations (van Gorkom et al. 1987). Furthermore, they show that the HI distribution and kinematics in NGC 4650A is consistent with the one commonly observed for an edge-on spiral disk, in particular the HI disk is extended right into the center.

In the light of the new results for the PRG NGC 4650A, presented in this Chapter and concerning the NIR and high resolution optical data, a revised dynamical model for the HI, optical structure and kinematics of this object should be done. This is the first future development of this work. As a preliminary study, indicative informations on the dark matter halo, which dominates the outer regions, are now derived.

5.5.1 Mass model

The distribution of HI velocity field, published by Arnaboldi et al. (1997), shows that the rotation curve is flat in the outer regions ($r \sim 36$ kpc) of the polar structure and the measured asymptotic velocity is about 120 km s^{-1}. In the central regions, within 12 kpc from the center, along the polar ring major axis, $H\alpha$ observations (by Whitmore et al. 1987) shows that the rotational curve is rising and the velocity reaches the maximal value of about 120 km s^{-1}. Here we tried to separate the contribution of the dark matter from that of the luminous matter in NGC 4650A, by taking into account the new results on the structure of this object, presented in this Chapter, in order to fit these data. To this aim, we need to assume a given mass density profile ($\rho(r)$) for each component: once the mass-to-light (M/L) ratio is fixed, this profile is simply proportional to the light distribution ($I(r)$) which characterized each component ($\rho(r) = (M/L)I(r)$). Given the mass distribution, the Poisson equation ($\nabla^2\Phi = 4\pi G\rho$) allow us to derive the potential Φ associated to this distribution. The rotational velocity (V_c), at a given distance from the center of the galaxy, is given by $V_c(r) = r(\partial\Phi/\partial r)$.The total gravitational potential in the polar ring galaxy NGC 4650A is given by the contributions from the host galaxy, polar structure and dark halo potential. Thus, the total rotational velocity is given by $V_{tot}^2 = V_{HG}^2 + V_{PR}^2 + V_{DH}^2$. We tried to derive the rotational velocity distribution for each component in order fit the observed total velocity curve.

As described in the previous sections, the central host galaxy in NGC 4650A has a small exponential bulge and a thick, nearly edge-on, disk with an exponential profile, which appears slightly warped in the outer regions. This warp is observed both in the optical and NIR. Since the effective radius of the

bulge is very small ($r_e = 0.1$ kpc in the I band), we neglect this component in the present analysis. So we model the central component as a *thick exponential disk* (Bahcall & Soneira 1980), with a surface brightness profiles given by the equation

$$\mu(R, z) = \mu_0 e^{-R/r_h} e^{-|z|/z_0}, \tag{5.4}$$

where R and z are cylindrical coordinates in the axi-symmetric disk, r_h and z_0 are the scalelenght and the scale height of the disk. These last two scale parameters are related by the expression $z_0/r_h = q_0$, which correspond to the intrinsic flattening of the galaxy. As suggested by Sackett et al. (1994), a good estimate of q_0 for a typical S0 galaxy is about 0.4. Thus, given $r_h = 1.2$ kpc from the 2D model (see Sec.5.2.3), the scale height of the host galaxy disk is $z_0 \sim 0.48$ kpc. In the B band, the central surface brightness of this disk component is $\mu_0 = 22.26$ mag $arcsec^{-2}$, it is derived starting from the value obtained by the 2D model in the I band and taking into account the average B-I color for this component (Tab.5.3).

Within the maximum disk hypothesis, which places as much mass as possible in the S0 disk and in the polar structure, Combes & Arnaboldi (1996) estimate an $M/L \sim 5$ for the polar ring and an $M/L \sim 4$ for the host galaxy. In our analysis we have adopted the same values, and the total mass, including only the stellar component, inside the polar structure is $M_{PR} \sim 4 \times 10^{10} M_\odot$ and inside the thick S0 disk is $M_{HG} \sim 3 \times 10^9 M_\odot$. For both components, host galaxy and polar disk, we derived the rotational velocity curve, for the stellar component alone, given by $V_{HG}^2 + V_{PR}^2$. This is compared, in Fig.5.16, with the observed velocities: the potential associated to the host galaxy and polar disk can account for the observed velocity out to 8 kpc from the center. To fit the observed velocities to larger distances ($R \leq 36$ kpc), we need to add the contribution to the potential of the dark matter halo. We adopted for the dark matter density profile of a *pseudo-isothermal sphere* (see Sackett et al. 1994; Combes & Arnaboldi), whose analytic expression is given by:

$$\rho(R) = \frac{\rho_0 r_c^2}{R^2 + r_c^2} \tag{5.5}$$

with r_c is the *core radius* and ρ_0 is the *central density.* This density profiles yields to the following rotational velocity curve:

$$V^2(R) = 4\pi G \rho_0 r_c^2 [1 - (r_c/R) \arctan(R/r_c)] \tag{5.6}$$

which produce an asymptotic velocity value given by $V_\infty = \sqrt{(4\pi G \rho_0 r_c^2)}$. By

fitting[4] the observed data, we derived an estimate for the core radius and central density values: $\rho_0 \sim 9 \times 10^{-3}\ M_\odot/pc^3$ and $r_c \sim 4.6$ kpc; thus, we obtained an asymptotic velocity for the dark halo $V_{DH} \approx 102$ km s^{-1}. The corresponding total mass inside 36 kpc (this is the largest distance from the center where the HI velocities are measured) is about $9 \times 10^{10} M_\odot$.

[4]This fit is performed by using the **GIPSY** (*Groningen Image Processing System* package).

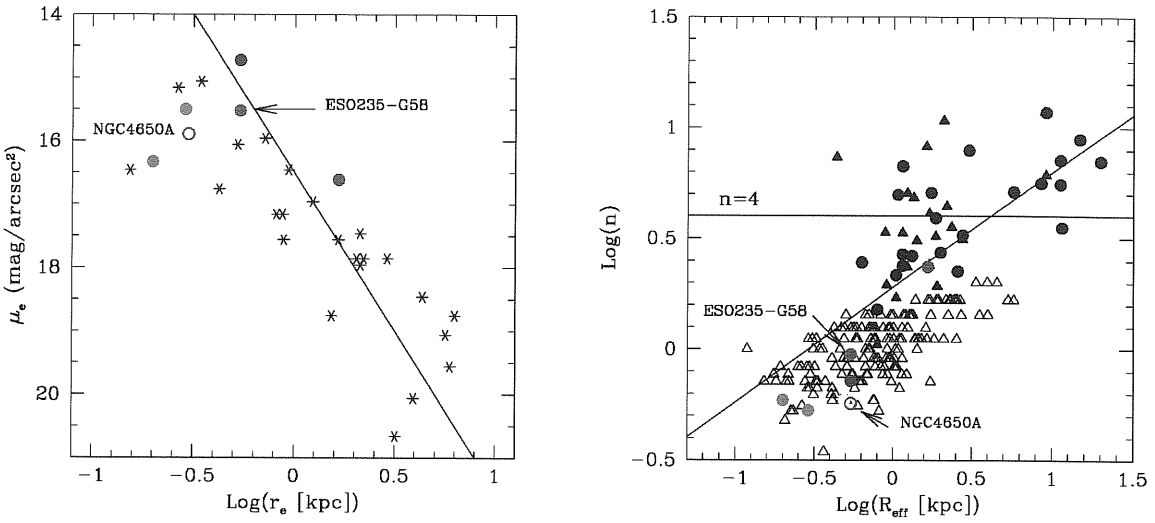

Figure 5.10: Left panel - Relation between the bulge effective parameters, μ_e and r_e, derived in the Kn band (Sec.3.3.1), for NGC 4650A (blue open circle). They are compared with values derived, in Sec.3.3.2, for PRGs (filled circles, the color code is defined in Tab.3.1), with typical values for early-type galaxies (asterisks), by Bothun & Gregg (1990). The solid line is a line of constant bulge luminosity derived for $\mu_e = 18\ mag/arcsec^2$, $r_e = 2$ kpc and $n = 4$. Right panel - Relation between the effective radius r_e and the n exponent of the generalized de Vaucouleurs' law (Sec.3.3.1), for the bulge component in NGC 4650A. They are compared with values derived, in Sec.3.3.2, for PRGs, with the typical values for early-type galaxies, Ellipticals (black circles) and S0s (black triangles) and for LSB galaxies (open triangles), Caon et al. (1993). The solid line is the relation between n and r_e (see Caon et al. 1993): $\log n = 0.28 + 0.52 \log r_e$.

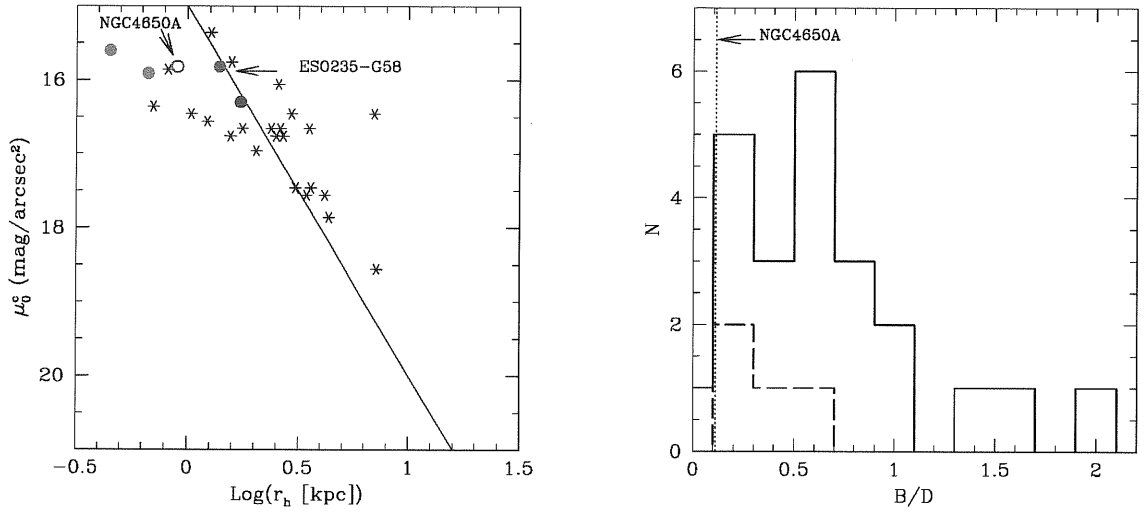

Figure 5.11: Left panel - Relation between the central surface brightness, corrected for the inclination, and the scalelength of the disk component, derived in the Kn band (Sec.3.3.1), in the host galaxy of NGC 4650A (blue open circle). They are compared with values obtained for PRGs (Sec.3.3.2, filled circles, whose color code is defined in Tab.3.1); with the typical values for early-type galaxies (asterisks), by Bothun & Gregg (1990). The solid line is a line of constant disk luminosity, derived for $\mu_0^c = 18\ mag/arcsec^2$ and $r_h = 1.6$ kpc. Right panel - B/D distribution for the PRGs (long-dashed line) and for early-type galaxies, by Bothun and Gregg (1990), (continuous line). The dotted line indicates the value of B/D derived for NGC 4650A (Tab.5.4).

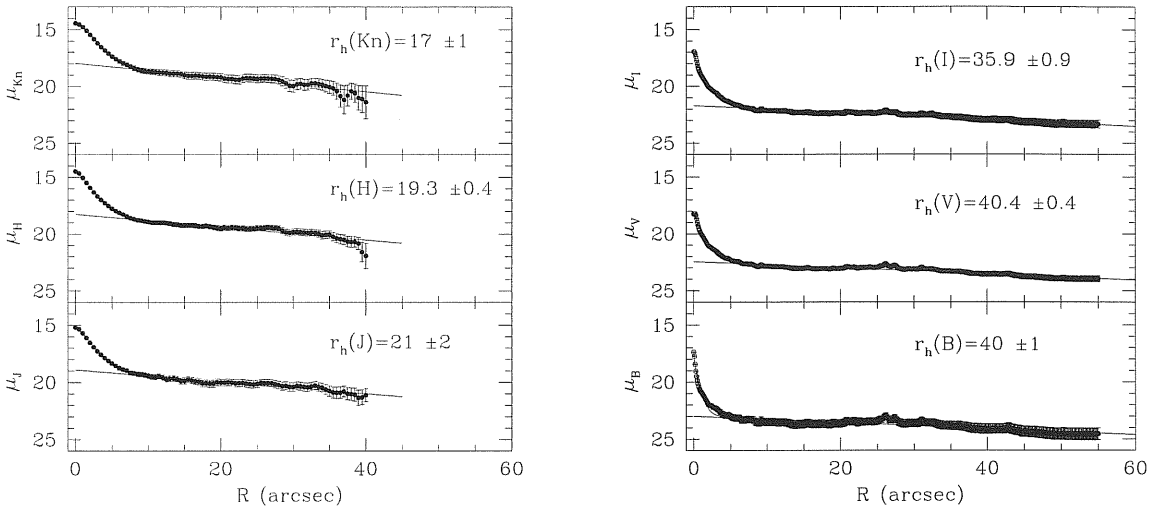

Figure 5.12: Left panels: average luminosity profiles for the polar ring in J (bottom), H (middle) and Kn band (top). Right panels: average luminosity profiles for the polar ring in B (bottom), V (middle) and I band (top). The best fitting exponential is overlaid on the data points in each plot; scalelengths are reported in arcsec.

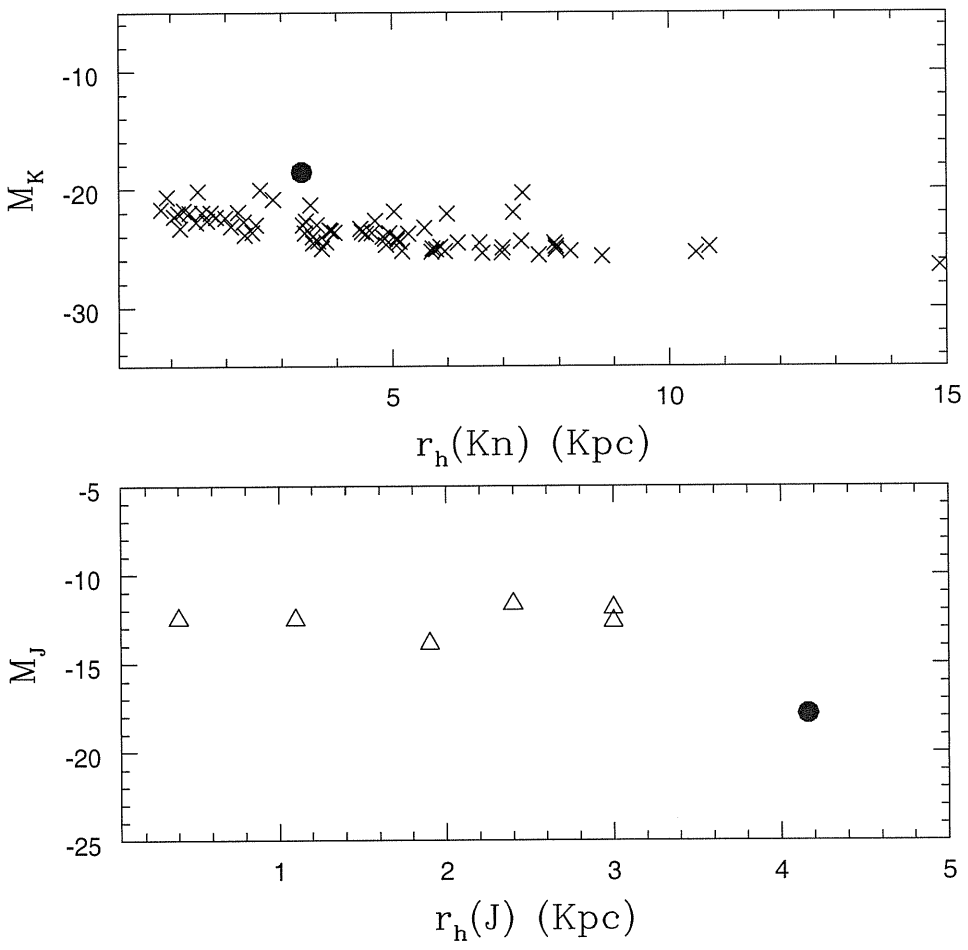

Figure 5.13: Absolute magnitude vs. disk scalelenght for the polar structure in NGC 4650A (blue filled circle) in the Kn band (upper panel) and in J band (lower panel). They are compared with the values derived for a sample of spiral galaxies (crosses) and LSB galaxies (open triangle).

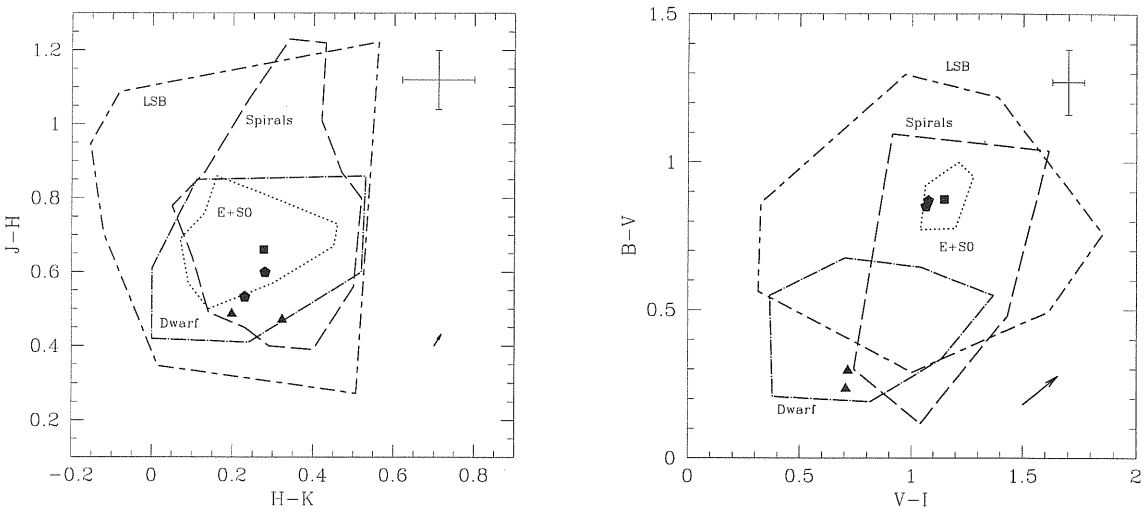

Figure 5.14: J-H vs. H-K (left panel) and B-V vs. V-I (right panel) color diagrams for the five areas of the NGC 4650A: filled square indicates the central region of the host galaxy; filled pentagons indicate the stellar component outside the central region; filled triangles indicate the polar ring regions. The dotted contour limits the region where the Es and S0s integrated colors are found; the long-dashed contour limits the integrated colors of spirals; the dashed-dotted contour identifies the integrated colors of the dwarf galaxies and the long dashed - short dashed contour identifies the integrated colors of LSB galaxies. The arrow, in the lower right corner, indicates the reddening vector for galactic dust and the screen model approximation, quoted in Sec.5.3. The average errors on colors are showed in the top right corner.

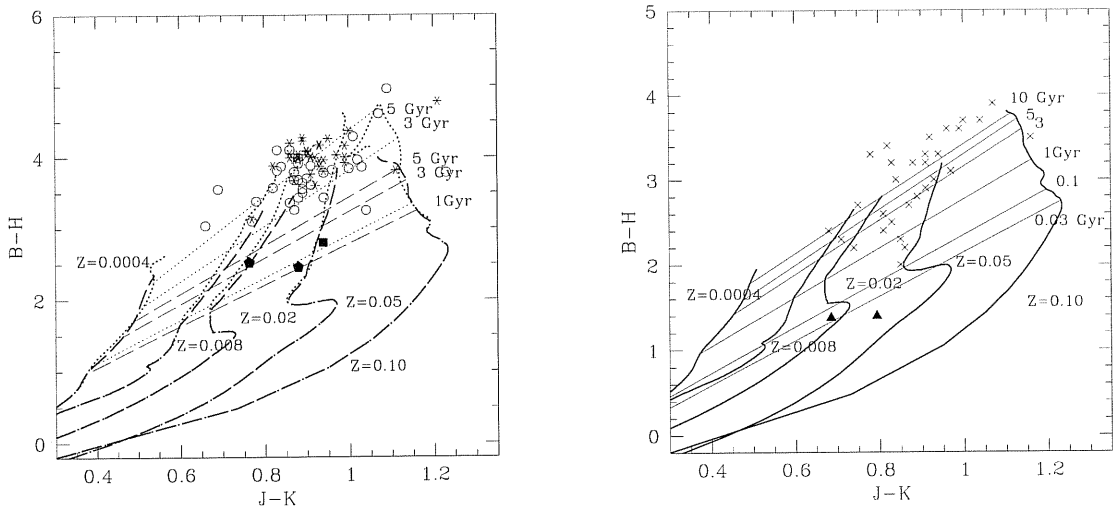

Figure 5.15: B-H vs. J-K diagram of the evolutionary tracks for the stellar synthesis models optimized for the central component (left panel) and the polar-ring component (right panel). Left panel: the heavier dotted lines correspond to models with a characteristic timescale $\tau = 1Gyr$ and heavier dashed lines for models with $\tau = 7Gyr$. Models are computed for different metallicities as shown on this figure. Light dotted and light dashed lines indicate loci of constant age for the different models; different ages are reported on the plot. The filled square and pentagons correspond respectively to the nucleus and the outer regions of the central spheroid in NGC 4650A, open circles and asterisks correspond to bulges and disks from a sample of S0 galaxies (Bothun, 1990). Right panel: heavier lines indicate model with constant SFR computed for different metallicities (as reported on the plot). Light lines are loci of constant age; different ages are quoted on the plot. Filled triangles indicate the polar ring regions; crosses are for a sample of spiral galaxies (Bothun et al., 1984).

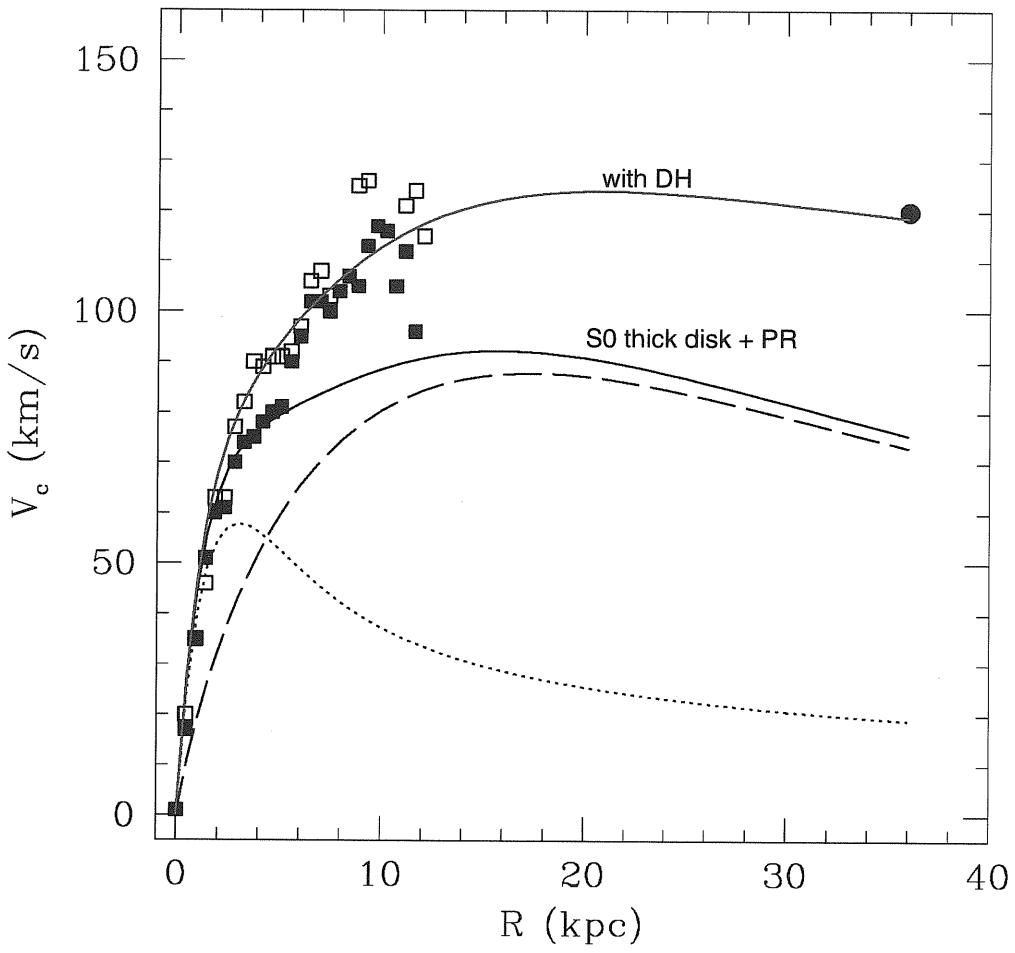

Figure 5.16: Comparison between the observed polar disk velocities and the predictions from the luminous mass model. The polar $H\alpha$ velocities are from Whitmore et al. (1987) (open squares are for approaching south side, and filled square are for receding north side). Filled circle is the value of the asymptotic velocity estimated by the high resolution HI map by Arnaboldi et al. (1997). Dotted line is the circular velocities predicted for the host galaxy thick disk; dashed line is the circular velocities predicted for the exponential polar disk; solid black line is the total velocity profile for these last two components. Solid red line is the rotational velocity which take into account also a spherical dark halo.

Chapter 6

The Tully-Fisher relation for PRGs

From the previous Chapters we have been exploring the connection between PRGs and spiral galaxies. This connection was quite important for the case of NGC 4650A (Chap.5). The whole galaxy sample studied so far have shown trends and correlation which are in agreement with strong dissipative mergers as in Bekki's hydrodynamical simulations.

The most important scaling relation for disks is the *Tully-Fisher law (TF)* (Tully and Fisher, 1977): this is an empirical relationship between the disk rotational velocity (V_{rot}) and its absolute luminosity (L), where $L \propto V_{rot}^4$. This relation has turned out to be a unique tool to explore the universe, the peculiar velocities and the 3D structure of the Universe itself. Furthermore, its implications for the formation of disk galaxies and the conspiracy between Dark Halo (DH) and baryonic contents have shown important insight in the DH - light interplay.

For bright disk galaxies, the TF law follows from the balance between rotational velocity and gravitation when the following assumptions are satisfied:

1. spiral galaxies are thin luminous disks with an exponential surface brightness distribution (Freeman 1970), given by $I(r) = I(0)\exp[-r/r_h]$, and total luminosity given by $L_{tot} \propto I_0 R^2$;

2. the central surface brightness $I(0)$ is assumed to be constant;

3. the stellar mass-to-light ratio is constant with radius in individual galaxies and has a universal value, $M/L = const$;

4. spiral disks are self-gravitating, thus $M \propto V^2 r$, where M is the stellar mass inside the radius r.

By combining the expression for the total luminosity and that for the self-gravitating disk, it is obtained $L \propto V_{rot}^4$. Random departures from conditions 1 to 3 in a given sample of galaxies will produce scatter around the relation, but the slope is preserved. Systematic departures from conditions 1 to 4 may induce a non-linearity in the TF relation which should show up as overall curvature (Persic & Salucci 1991).

The TF is extensively used to estimate extragalactic distances (e.g. Sakai et al. 2000; Tully & Pierce 2000). Furthermore, in the galaxy formation theories, this relation is considered a critical constraint (Dalcanton et al. 1997; McGaugh & de Blok 1998; Mo et al. 1998; Steimnetz & Navarro 1999; van de Bosch 2000). Several studies tried to addressed the origin of the TF relation, but a definitive conclusion is not still found. The debate concerns whether initial cosmological condition have governed the origin of the TF (e.g., Firmani & Avila-Rees 1998a, 1998b), or whether it was due to particular processes in star formation (Silk 1997; Heavens & Jiminez 1999) and/or feedback (Kauffmann, White and Guiderdoni 1993; Cole et al. 1994; Elizondo et al. 1999; van de Bosch, 2000). None of the above theories predict the observed relation.

The PRGs are characterized by a large amount of neutral hydrogen (HI), which is associated with the ring component (van Gorkom et al. 1987; Arnaboldi et al. 1997; van Driel et al. 2000). Given the very efficient use of the TF based on the HI integrated emission profiles in disk galaxies, we wish to explore whether a similar relation would hold for the HI line width and total luminosity of polar rings.

6.1 The Tully-Fisher relation: latest developments

McGaugh and collaborators (2000) have explored the TF relation over a wide range of stellar mass ($10^7 M_\odot < M < 10^{12} M_\odot$) in galaxies with circular velocities from 30 to 300 km s^{-1} . They plotted the stellar mass ($M_\star$) versus the rotation velocity, which becomes the analogous of relation between the total luminosity and V_{rot} , if we assume a constant mass-to-light ratio, $\Upsilon_\star$, and $M_\star = \Upsilon_\star L$ (left panel of Fig.6.1). In this plots the observed data shows a break for faint field galaxies: for $V_{rot} \leq 90$ km s^{-1}, the observed mean luminosity of galaxies is fainter that the one predicted by the extrapolation of

the TF relation determined from galaxies with larger rotation. A common characteristic to all these "underluminous" galaxies is the large gas content. By adding the gas mass to the stellar mass, and computing the total disk mass $M_d = M_\star + M_{gas}$, i.e. *total baryonic mass* of the galaxy, they obtained the following result: the faint galaxies move toward the linear relation between V_{rot} and M_d obtained for brighter disk galaxies (right panel of Fig.6.1). The "baryonic TF relation" is applicable over the entire mass range.

6.1.1 Implications of the TF on the dark halo-baryons conspiracy

Why is the validity of the TF relation so important as to give insight on the DH vs baryonic connection? As we have stated before, for a bright self gravitating disk, the TF relation is trivial. For low luminous disks, accurate mass modeling of the 2D HI velocity maps indicates that there is not enough light to reproduce the observed velocities inside the optical radius of these disks (e.g. de Blok & McGaugh 1997). Therefore the line width in the HI integrated line profile reflects a dynamic which is dominated mainly by the DH. The observed properties of faint disk derived by McGaugh et al. (2000) indicates that the global DH properties are tuned by how many baryons there are (despite the fact that the maximum disk hypothesis is not valid for these systems).

6.2 The Tully-Fisher relation for PRGs

We wish to explore whether the TF holds for PRGs. To this aim we computed the total Kn band magnitude[1] for each polar ring galaxy in our sample. The HI integrated line profile data were obtained from published neutral hydrogen survey of polar ring galaxies, which was carried out by van Driel and collaborators (2000), with the Nançay decimetric radio telescope. The total Kn magnitude and measured line width at 20% of the $21 - cm$ flux peak, for each PRG in our sample are listed in Tab.6.1.

We wish to compare the observed TF relation of PRGs in the NIR with that observed for bright disk galaxies: in Fig.6.2 we show the TF relation for a sample of spiral galaxies studied by Verheijen (1997, 2001). The values of

[1]To do this, a unique polygon, encircling the whole object, was defined (by using the IRAF task POLYMARK) and, inside it, the integrated magnitude was computed, through the IRAF task POLYPHOT.

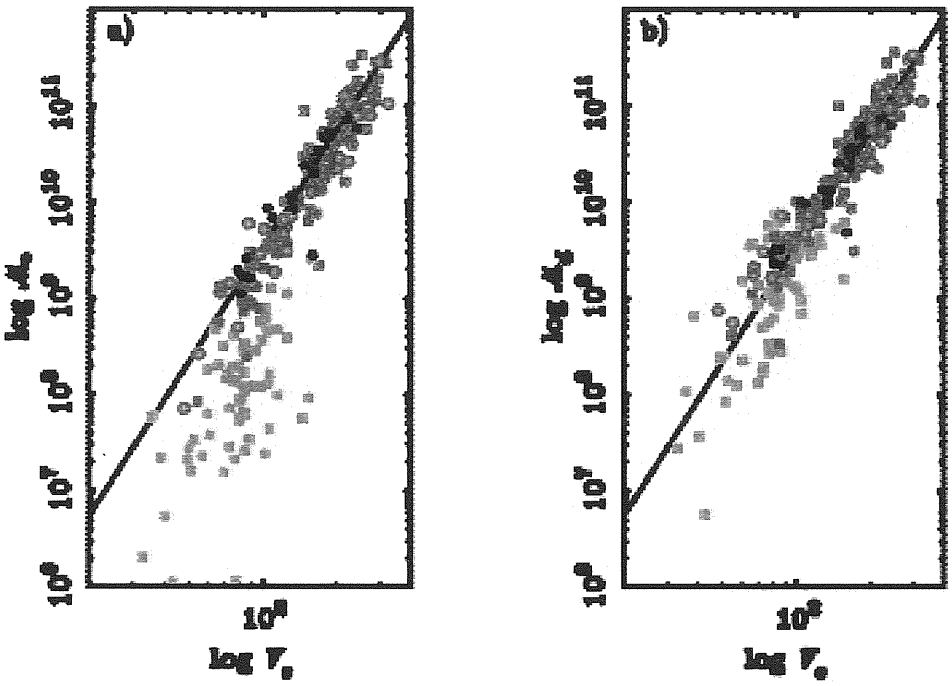

Figure 6.1: Tully-Fisher relation plotted as (a) stellar mass and (b) baryonic disk mass against rotation velocity derived by McGaugh et al. (2000), see Figure 1 of the cited paper for further details. In (a), a clear break is apparent. Galaxies with $V_c \leq 90$ km s^{-1} fall systematically below the Tully-Fisher relation defined by brighter galaxies. In (b), the deficit in mass apparent in (a) has been restored by including the gas mass. The solid line is an unweighted fit to the red-band data in (b) with a correlation coefficient of 0.92 and a slope indistinguishable from 4.

M_{Kn} and $log(\Delta V_{20})$ for PRGs are also shown in this plot and all polar ring galaxies, but AM2020-504, lie on the observed TF relation for spiral galaxies.

This behavior is not expected a priori and we wish to investigate its implications. This is very much work in progress and therefore we apologize if some of the conclusion may not be all complete. In PRG, the work by Sackett & Sparke (1990), Sackett et al. (1994), Reshetnikov & Combes (1994), Combes & Arnaboldi (1996) have shown that the flat rotation curves observed for the HI in the polar ring components cannot be reproduced by the luminous mass in the system with a constant M/L ratio, and a dark halo is needed to reproduce the observed large velocities. The fact that the observed total integrated HI line width, tracing the dynamic in the meridian plane, and the total Kn light for PRG fall on the TF is therefore an independent verification of the dark halo-baryonic conspiracy.

Another implication from the TF relation may involve the shape of the dark halos around PRGs. The recent discussions on dark halo shape following the work of Sackett et al. (1994) imply that the dark halo may be quite flattened, and for some objects its flattening may coincide with that of the luminous light distribution. We have started to explore its implications on the TF relation for PRGs.

We have assumed that in the PRG systems, analysed here, the DH is flattened as the light distribution (assuming a constant flattening given by the average isophotal axial ratio). We have also used the relation derived by Whitmote et al. (1987) to derive the polar velocity by the equatorial one in the case of an isotropic oblate spheroid

$$\frac{b}{a} = -0.215 + 1.2117\frac{V_{pol}}{V_{eq}} \tag{6.1}$$

where, b/a is the flattening of the potential, V_{pol} and V_{eq} are the rotational velocity in the polar plane and in the equatorial plane, respectively. Given that the DH in this model is distributed as the luminous matter, the TF relation should be valid for kinematical quantities obtained along the principal plane of the light distribution. When the HI observed line widths for PRGs are corrected to express quantities along the equatorial plane (these values are listed in the fourth column of Tab.6.1), the observed points in the $M_K, \Delta V$ plane move away from the the TF relation determined for disk galaxies, as shown in Fig.6.3. A first simple interpretation of this behavior is that the DH in polar rings cannot be as flattened as the host galaxy light distribution, i.e. it may be nearly spherical or, as suggested by Combes & Arnaboldi (1996), it may be associated with the polar disks themselves.

Table 6.1: Absolute magnitude in the Kn, M_{Kn}, and the linewidth at 20% of the peak of $21-cm$ flux, ΔV_{20}, for each Polar Ring Galaxy of the selected sample. Furthermore, in the fourth column, are listed the estimated values of the rotational velocities in the equatorial plane at the same distance from the center where the ΔV_{20} is measured. The velocities are expressed in km s^{-1}.

Object name	M_{Kn}	ΔV_{20}	ΔV_{equ}
ESO 415-G28	-22.7	359	561
NGC 4650A	-21.4	240	298
ARP 230	-20.9	242	340
AM 2020-504	-22.6	164	206
ESO 603-G21	-21.6	217	272
ESO 235-G58	-22.0	292	456

Why does AM 2020-504 deviates from TF relation? The observed values of $M_K, \Delta V$ for AM 2020 fall in the region of the diagram where the observed velocities are smaller than what galaxy luminosity would imply. This may be due to the observed HI distribution in this galaxy, which does not extent out to large distance, therefore the velocities do refer to the still rising part of the rotation curve and they do not trace the maximal velocity.

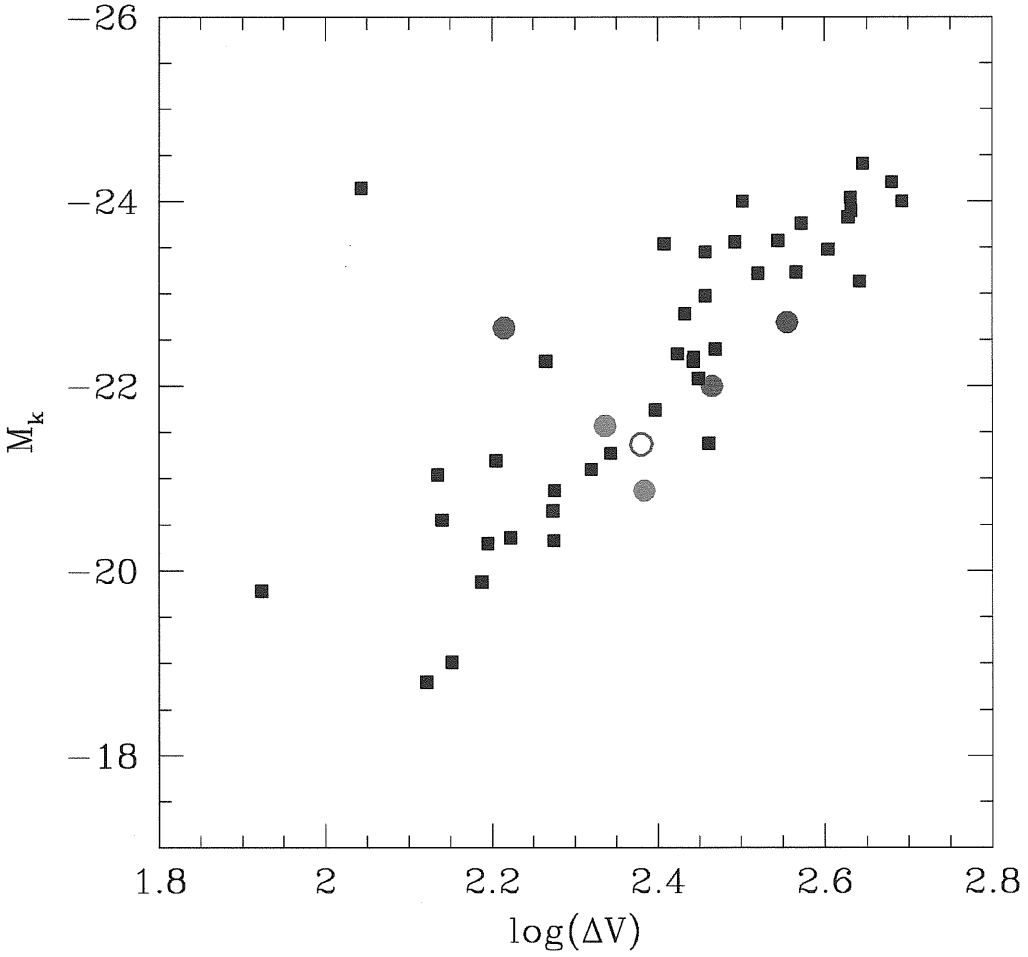

Figure 6.2: Absolute magnitude in the Kn band vs. the measured linewidth at 20% of the peak of $21-cm$ flux (ΔV_{20}), for PRGs of the selected sample (filled and open circles), color code is defined in Tab.3.1. They are compared with a sample of spiral galaxies (filled squares), studied by Verheijen (1997, 2001).

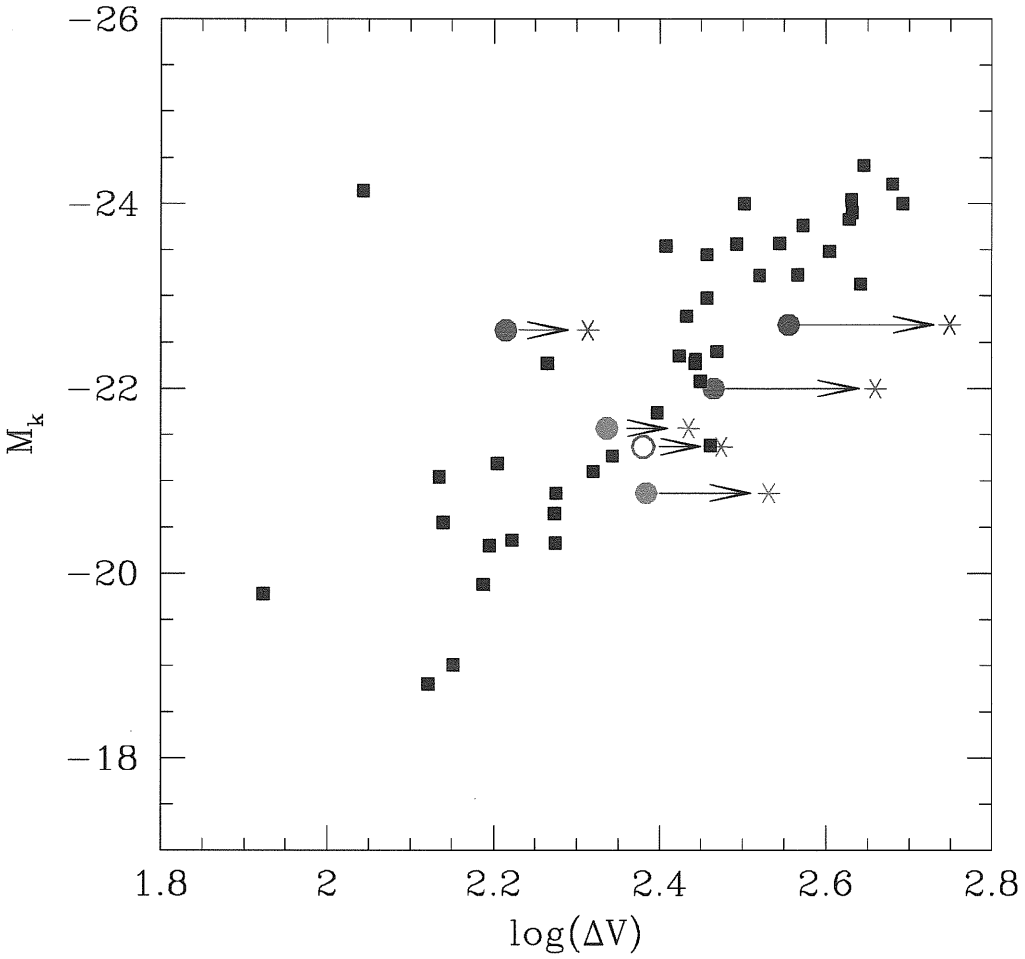

Figure 6.3: Same plot showed in Fig.6.2 where are added the values of the rotational velocities in the equatorial plane (asterisks).

Conclusions

This PhD thesis has been part of an ongoing research project about photometric and kinematic properties of **Polar Ring Galaxies**. In this work we have presented a detailed photometric study for a sample of PRGs, selected from the Polar Ring Catalogue (PRC, Whitmore et al. 1990), based on new NIR observations. We now wish to compare the the properties predicted for PRGs in different formation scenarios against the global properties observed for the polar ring systems studied in this work.

Possible scenarios for polar ring formation can be grouped into two main pictures, i.e 1) accretion of a gas-rich dwarf galaxy by an early-type system or gas stripped from a nearby gas-rich object, and 2) a major dissipative merging of two disk galaxies. In the following, we briefly summarize the main predictions from each scenario.

An accretion event is an encounter between galaxies where the total mass of one of the interacting system is much greater than the other. In this condition, the evolution of the system can be reproduced by considering a perturbation to the potential of the more massive galaxy (Quinn 1984). Accretion in, or gas-stripping by, an oblate/triaxial galaxy can predict the formation of a polar ring. These rings can be in a quasi-equilibrium configuration if 1) their ratio $\Delta R/\bar{R}$ is between 10% and 30%, where ΔR is the radial extension of the ring and $\bar{R}$ the average radius (Katz & Rix, 1992; Christodoulou et al. 1992; Reshetnikov & Sotnikova, 1997) and 2) self-gravity is at work (Sparke 1986, Arnaboldi & Sparke 1994). The total amount of accreted gas can be of the order of $10^9 M_{\odot}$, which is the typical amount of HI in a gas-rich dwarf (Carignan 1999). The process of ring formation through accretion/stripping of a gas-rich companion takes few Gyrs at most. In this scenario the host galaxy is an early-type gas-free system and preserves its structure (luminosity profile, B/D ratio, scale parameters), while some star formation is triggered by the event (Arnaboldi et al. 1993).

The merging scenario of two disks can account for the formation of narrow rings as well as of wide/massive disk-like structures, depending on the initial

mass ratio of the two merging progenitors. According to this scenario, the polar structure is the remnant of the disk of the "victim" galaxy, while the accreted "intruder" has supplied the S0-like component. Polar rings are more likely to form when the two disks are on a polar orbit, with a small initial orbital angular momentum (Bekki 1998). In this scenario the two interacting galaxies can have similar masses and the polar component might even be as massive as the host galaxy. This dissipative merger event transforms the intruder's thin stellar disk into a thicker structure, and both intruder's and victim's disk profiles evolve to become more centrally concentrated with respect to the initial exponential profiles. When extended polar structures are formed (depending on the intruder/victim mass ratio), they are characterized by the absence of a hole in the central regions, and their HI content can be as large as that of late-type spirals, i.e. up to $10^{10} M_{\odot}$. The predicted evolution time for the whole resulting polar ring galaxy is of about 10^9 yr, and the outwardly propagating gaseous waves, excited by the intruder galaxy, trigger a burst of stellar formation in the polar structure.

Now we summarize which are the main observational properties of the PRGs studied in this work: we firstly discuss about the global characteristics of the central host galaxy and then those relative to the polar structure.

The morphology of the host galaxy in all PRGs of our sample, except for AM 2020-504 and ESO 235-G58, resembles that of an S0 galaxy, as the disk-like structure found along its major axis suggests. However, a detailed study of the light and color distributions have shown that this component differs from a "standard" S0 galaxy. In all systems, a color gradient toward bluer colors is observed from the nucleus (which is characterized by the reddest colors of the whole object) to the outer regions. The mean colors of the stellar component outside the nucleus are, on average, bluer than the typical values for elliptical and S0 galaxies: this is found in nearly all objects. We estimated the mean age of the stellar population in this component to be between 1 and 3 Gyrs, which is significantly younger than the typical age for early-type galaxies. The 2D model of the host galaxy light distribution, performed in the Kn band, has shown that this component is composed by a nearly exponential bulge and an outer exponential disk. The analysis of their structural parameters suggests that the host galaxy in PRGs is characterized by a more "compact" bulge respect to that in S0 galaxies and by a brighter and smaller disk than the S0's disks. The resulting B/D ratio is in the range of disk-dominated S0 galaxies.

The extension of the polar structure in all PRGs, except for A0136-0801 and NGC 4650A, is comparable to the host galaxy optical radius; in the case of A0136-0801 and NGC 4650A this component is at least 2 times more extended

than the host galaxy in the NIR bands (while in the optical it is even larger). Furthermore, in NGC 4650A, we found that this component is more similar to a spiral disk rather than a wide annulus (see Chap.5). In all PRGs of our sample the colors of the polar structure fall in the same regions where late-type systems (like dwarf and spiral galaxies) are also found, furthermore they are, on average, bluer than the central host galaxy, implying a younger age for this component. In all PRGs studied in this work, the polar ring seems to be not older than 1 Gyr; polar disk in NGC 4650A seems to be even younger ($\sim 10^8$ yrs) than these last ones. An interesting result was derived by studying the light distribution of the polar structure in all objects of the sample: the ratio between its radial extension (ΔR) and its mean radius ($\bar{R}$) varies in the range from 35% to 50%, in all PRGs of the sample except for AM 2020-504, whose polar ring is characterized by a significantly smaller $\Delta R/\bar{R}$ (about 10%).

Previous studies on PRGs, including also the objects in our sample, have shown that they are characterized by a very high amount of HI gas, always associated to the polar structure (van Gorkom et al. 1987; Arnaboldi et al. 1997; van Driel et al. 2000), especially high if compared with the gas content of normal S0 galaxies, which often have no detectable HI. The HI mass in the polar ring galaxies studied in this work is larger than $10^9 M_\odot$ and reaches the value of about $10^{10} M_\odot$ in NGC 4650A. We found that the total baryonic mass (gas plus stars) in the polar structure for all PRGs, but AM2020-504, is comparable with or even higher than the total luminous mass in the host galaxy, (see Sec.3.6, Sec.4.8 and Sec.5.4).

May these new observational properties help to discriminate between the two formation scenario for PRGs?

For all PRGs of our sample, except for AM 2020-504, the accretion/stripping scenario seems not able to predict 1) the main characteristics in the light and color distribution of the host galaxy, which make this component a non standard S0 system; 2) the large values for the $\Delta R/\bar{R}$ ratio, which is related to the ring extension; 2) the absence of hole in the polar structure of NGC 4650A; 3) the high HI mass, which is larger than the maximal amount of the accreted gas; 4) the high accreted baryonic mass (stellar + gas), which should be a fraction of that in the pre-existing galaxy, and not vice versa, as it is observed for NGC 4650A.

On the other hand, the observed properties for AM 2020-504 (see Sec.3.5) suggest that this polar ring galaxy may be the only object of the sample which may be formed through an accretion or gas-stripping event involving an elliptical galaxy.

Many of the observed properties in the host galaxy and polar structure,

listed above, are predicted by the dissipative merger scenario proposed by Bekki (1998). In this scenario both the central S0-like system and ring component in a polar ring galaxy are simultaneously formed through a dissipative merger between two disk galaxies. The required constraints on the specific orbital configurations and gaseous dissipation in galaxy merging, required in this model for the formation of PRGs, naturally explain the prevalence of S0-like systems among polar ring galaxies (e.g., Whitmore 1991) and the appreciably larger amount of interstellar gas in PRGs (van Gorkom et al. 1987, Arnaboldi et al. 1997, van Driel et al. 2000). Furthermore, the different morphologies observed for polar ring, such as narrow rings (e.g. ESO 415-G26, or in ARP 230) and wide disk-like structures with no central hole (e.g. NGC 4650A), are related to the orbital parameters of galaxy merging and the initial mass ratio of the two interacting galaxies. This scenario does predict peculiar characteristics for the host galaxy, which turns out not to be a standard S0 galaxy: the progenitor galaxy (the intruder) experiences both a heating of the disk (it puffs up) and energy dissipation. The energy dissipation leads to an higher increase of the mass density in the center, with respect to the unperturbed disk, which may develop a central small and nearly exponential bulge: this is very similar to what we have detected in nearly all PRGs of our sample. Moreover, the evolutionary timescales of the merging process, which is about 10^9 yr, is also consistent with the young age, predicted for PRGs in this work, both for the host galaxy (1 to 3 Gyr) and polar structure ($\sim$ 1 Gyr).

An important constraint for the Bekki scenario is the small value of the relative velocities ($V \sim 33$ km s^{-1}) of the two merging galaxies required to form PRGs: such velocities are more likely to occur in high redshift universe rather than in the nearby, where bound group of galaxies are virialized and therefore the relative velocities are larger. For instance, in the Virgo cluster the mean velocity dispersion of galaxies in the cluster is about 800 km s^{-1} (Bingelli et al. 1987). In fact, Reshetnikov (1997) have found an increasing rate of detection for PRGs toward higher redshift: among all galaxy types, in the Hubble Deep Field (Williams et al. 1995) candidate polar ring galaxies are $\sim 0.7\%$, while in the local universe is $\sim 0.05\%$ (Whitmore 1990).

Although uncertainties in the numerical treatment of gas dynamics and star formation still remain in the Bekki's approach, dissipative galaxy merging, with specific initial conditions, seems now a promising scenario be further investigate to explain the formation of Polar Ring Galaxies and some of the most important observational properties of these systems. In the framework where elliptical and S0 galaxies are formed by merging of two disk galaxies (Barnes & Hernquist 1992; Bekki & Shioya 1997), PRGs are products from a

particular case of the more general initial conditions which led to the formation of early-type galaxies. PRGs are formed when the two merging disks have unequal mass, small relative velocities and are on high perpendicular orbit; when these conditions are not in place, the merger remnant is similar to a normal elliptical or S0 galaxy.

A future test of the merging scenario for PRG formation, in particular of the Bekki's models, will also include a detailed analysis of the kinematics predicted from the N-body simulations and a comparison with PRG kinematics, for a large sample of these systems.

Appendix A

CASPIR

The **Cryogenic Array Spectrometer/Imager (CASPIR)**, under development at the ANU 2.3 m telescope at Siding Spring Observatory, uses a Santa Barbara Research Center 256x256 InSb detector array to provide direct imaging and spectroscopic capabilities in the 1-5 micron wavelength range. Two direct imaging focal plane scales of 0.5"/pixel and 0.25"/pixel are available.

The detector Quantum Efficiency (Q.E.) function is plotted in Fig.A.1. The transmission curves for the J, H and Kn filters, as measured by the manufacturer, are shown Fig.A.2.

In Tab.A.1 we compare the typical values of the zero point offsets for each filter estimated for this detector[1], available in the CASPIR user manual, with the values derived in this work.

In Tab.A.2 the CASPIR predicted performance, for the 0.5"/pixel scale, are listed: the readout noise (RN), background level and dark current are derived in 60 seconds of on-source integration in different seeing conditions, for J, H and Kn.

Other useful informations about the CASPIR infrared camera are available at the web site "http://msowww.anu.edu.au/observing/2.3m/CASPIR/".

[1]These values are based on the total ADUs in a sky-subtracted stellar image after correction for airmass effects.

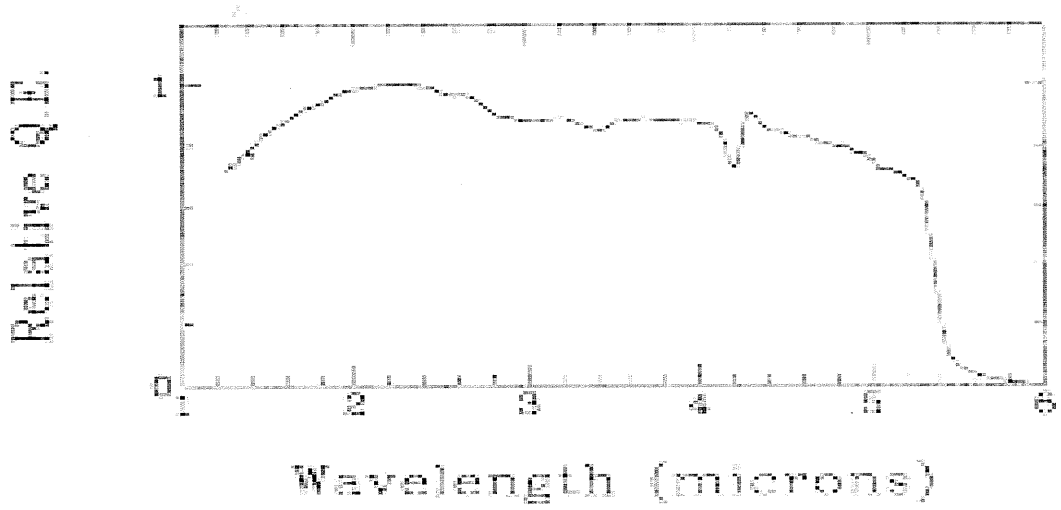

Figure A.1: Relative quantum efficiency for a typical Cincinnati Electronics 0.5 mm diameter InSb detector used at ANU 2.3 m telescope at Siding Spring Observatory

Table A.1: Comparison between predicted zero points, from McGregor (1994) and observed zero points in this work, for each night and for each filter. Values are in $mag/arcsec^2$.

Source	J	H	Kn
McGregor 1994	21.6	21.6	20.5
This work:			
20/03/1995		21.48 ± 0.03	20.59 ± 0.03
21/03/1995	21.59 ± 0.02	21.44 ± 0.01	
18/08/1995	21.65 ± 0.03	21.54 ± 0.02	20.70 ± 0.03
19/08/1995	21.70 ± 0.03	21.56 ± 0.03	20.71 ± 0.01
20/08/1995	21.69 ± 0.03	21.51 ± 0.04	20.68 ± 0.03

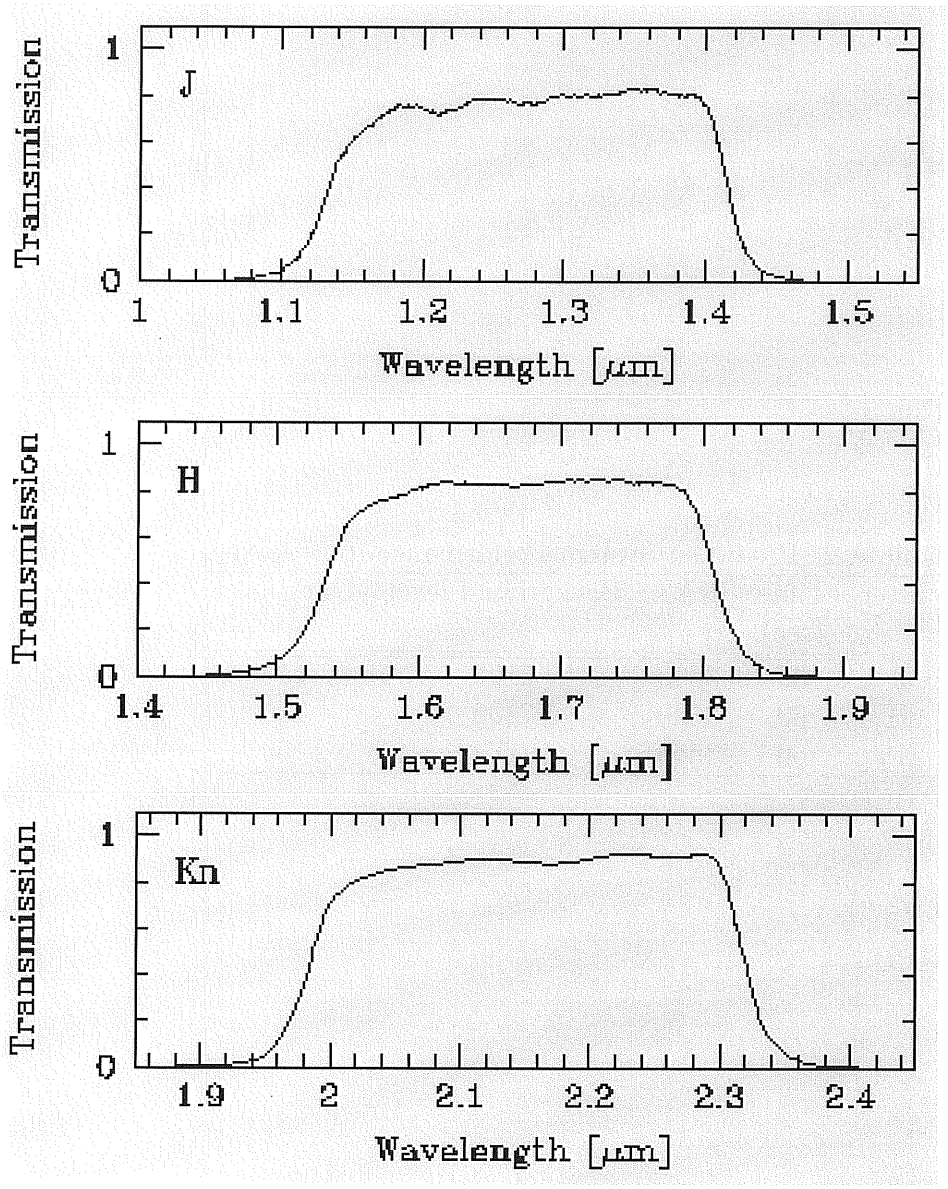

Figure A.2: Transmission curves for the CASPIR J (top panel), H (middle panel) and Kn (bottom panel) filters.

Table A.2: Predicted System Performance (0.5"/pixel).

Filter	Time (sec)	RN^2 $(e^-)^2$	Background level e^-	Dark level e^-
J	60	3600	3100	150
H	60	3600	7100	150
Kn	60	3600	19550	150

Appendix B

NIR images of Polar Ring Galaxies

Here are presented the NIR J and Kn images, and the relative high-frequency residual images (Sec.2.2), of PRGs studied in Chap.2 and Chap.3. Furthermore, the V, I, J and Kn band images, for the peculiar galaxy ESO 235-G58 (Chap.4) and the optical B, V, I HST data and J, H and Kn band images for the polar ring galaxy NGC 4650A (studied in Chap.5), are also shown. Each image is shown in the left panel of the following figures, and the correspondent high-frequency residual images (Sec.2.2) is shown in the right panel. In each figure, units are intensity and North is up and East is to the left, unless it is specified in the caption.

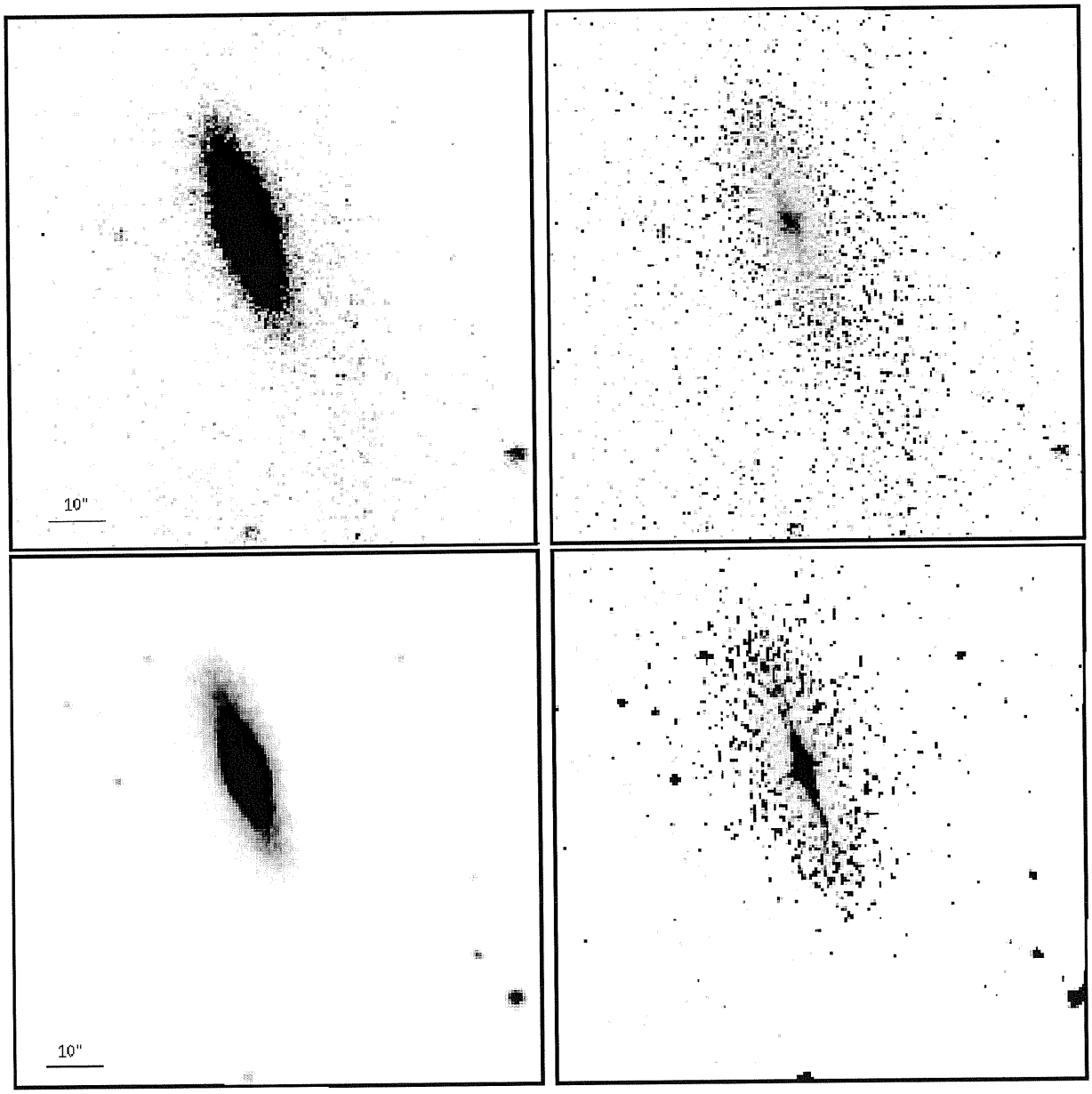

Figure B.1: **ESO415-G26**:J band (top-left panel) and Kn band image (bottom-left panel) and relative high-frequency residual images (top-right panel, in J band) and (bottom-right panel, in Kn band).

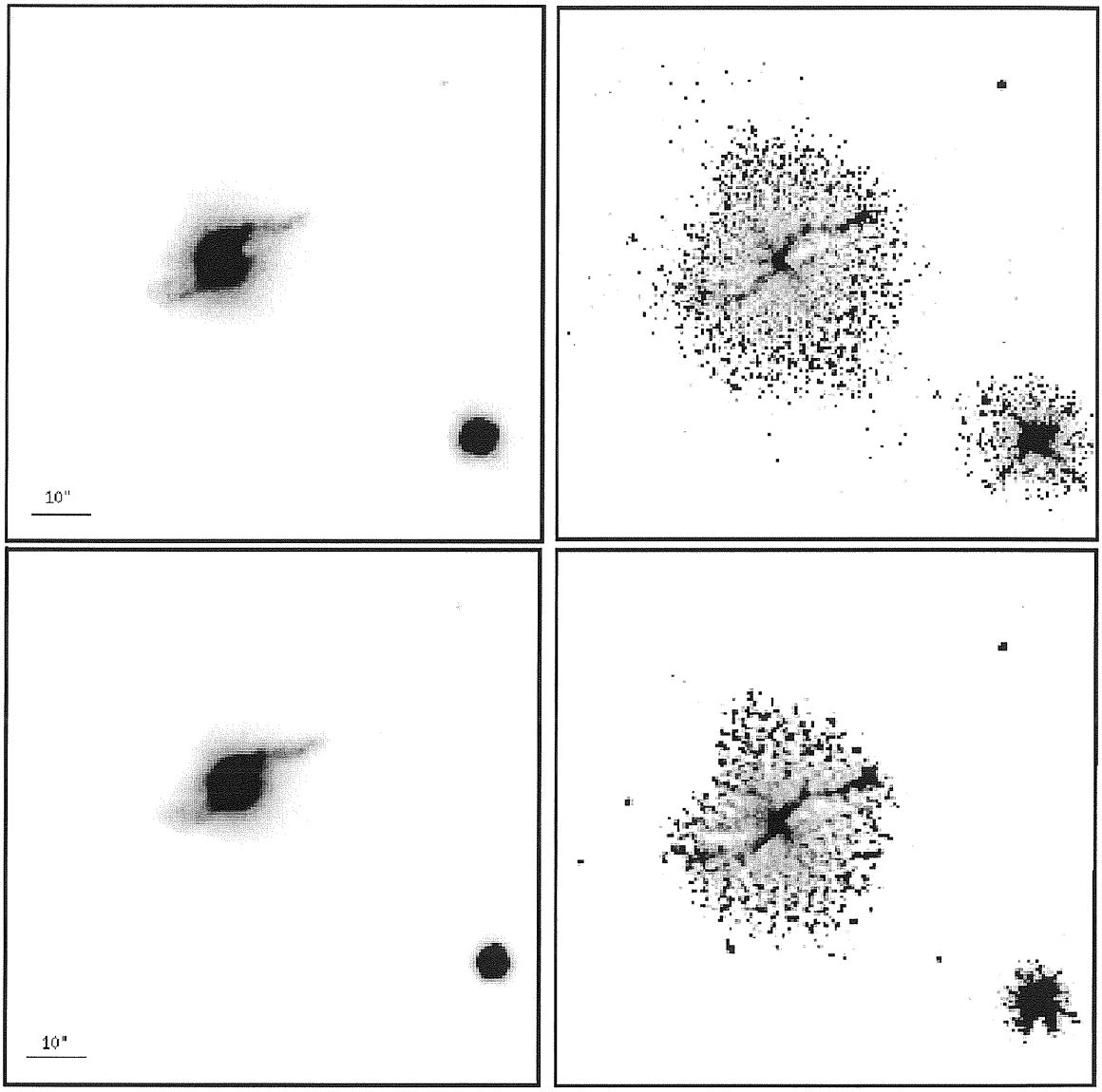

Figure B.2: **ARP230**:J band (top-left panel) and Kn band image (bottom-left panel) and relative high-frequency residual images (top-right panel, in J band) and (bottom-right panel, in Kn band).

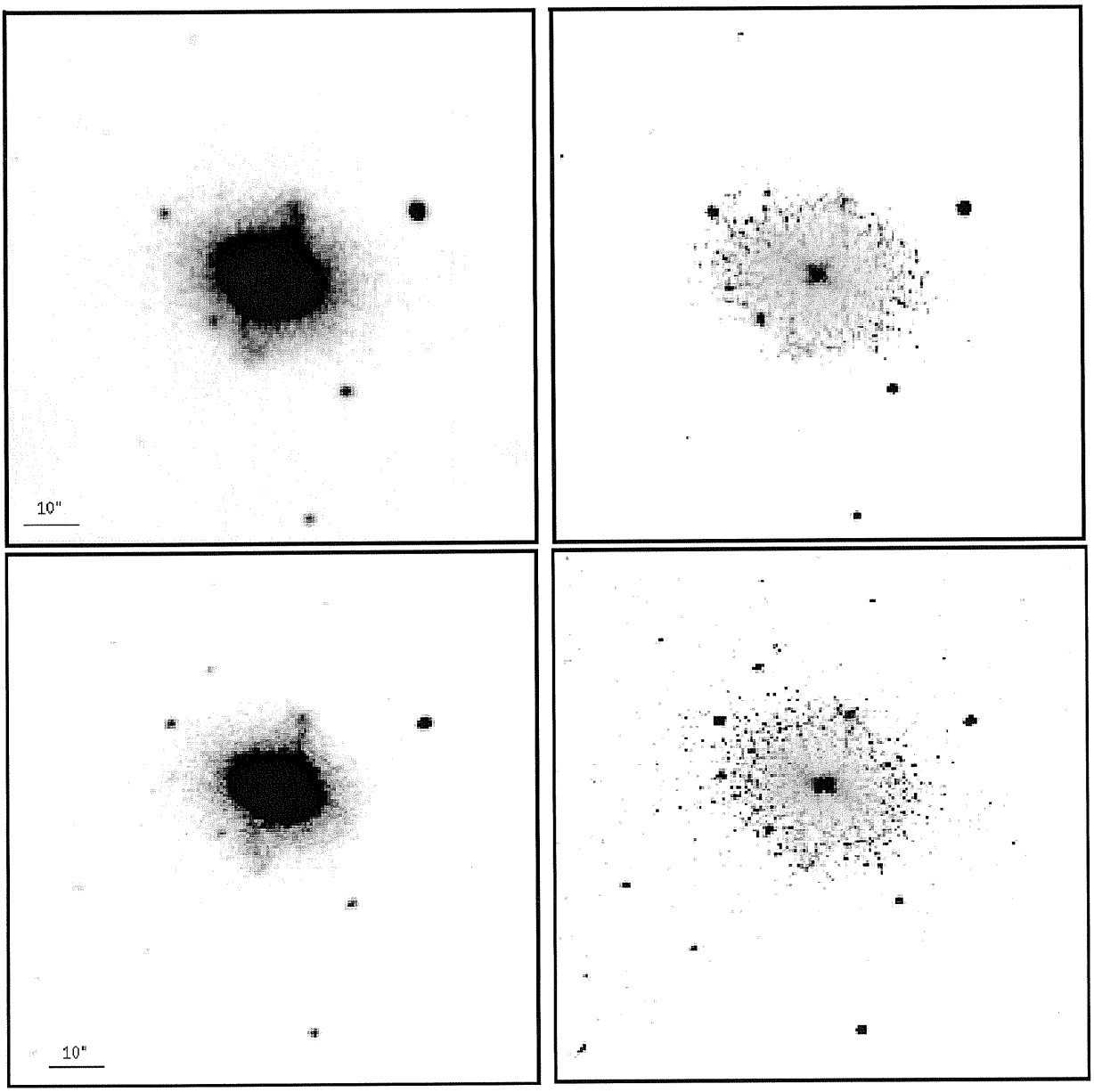

Figure B.3: **AM2020-504**:J band (top-left panel) and Kn band image (bottom-left panel) and relative high-frequency residual images (top-right panel, in J band) and (bottom-right panel, in Kn band).

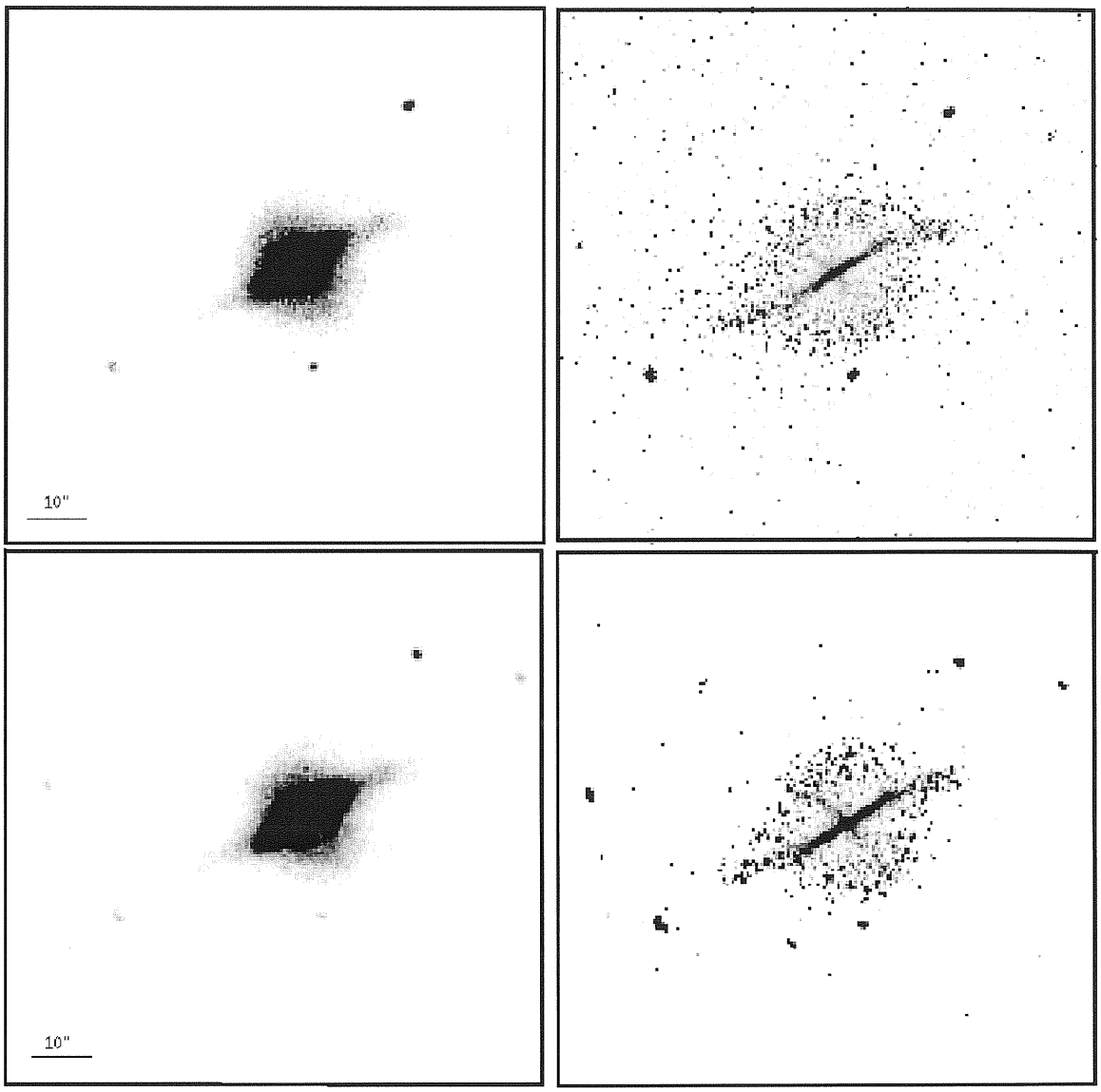

Figure B.4: **ESO603-G21**:J band (top-left panel) and Kn band image (bottom-left panel) and relative high-frequency residual images (top-right panel, in J band) and (bottom-right panel, in Kn band).

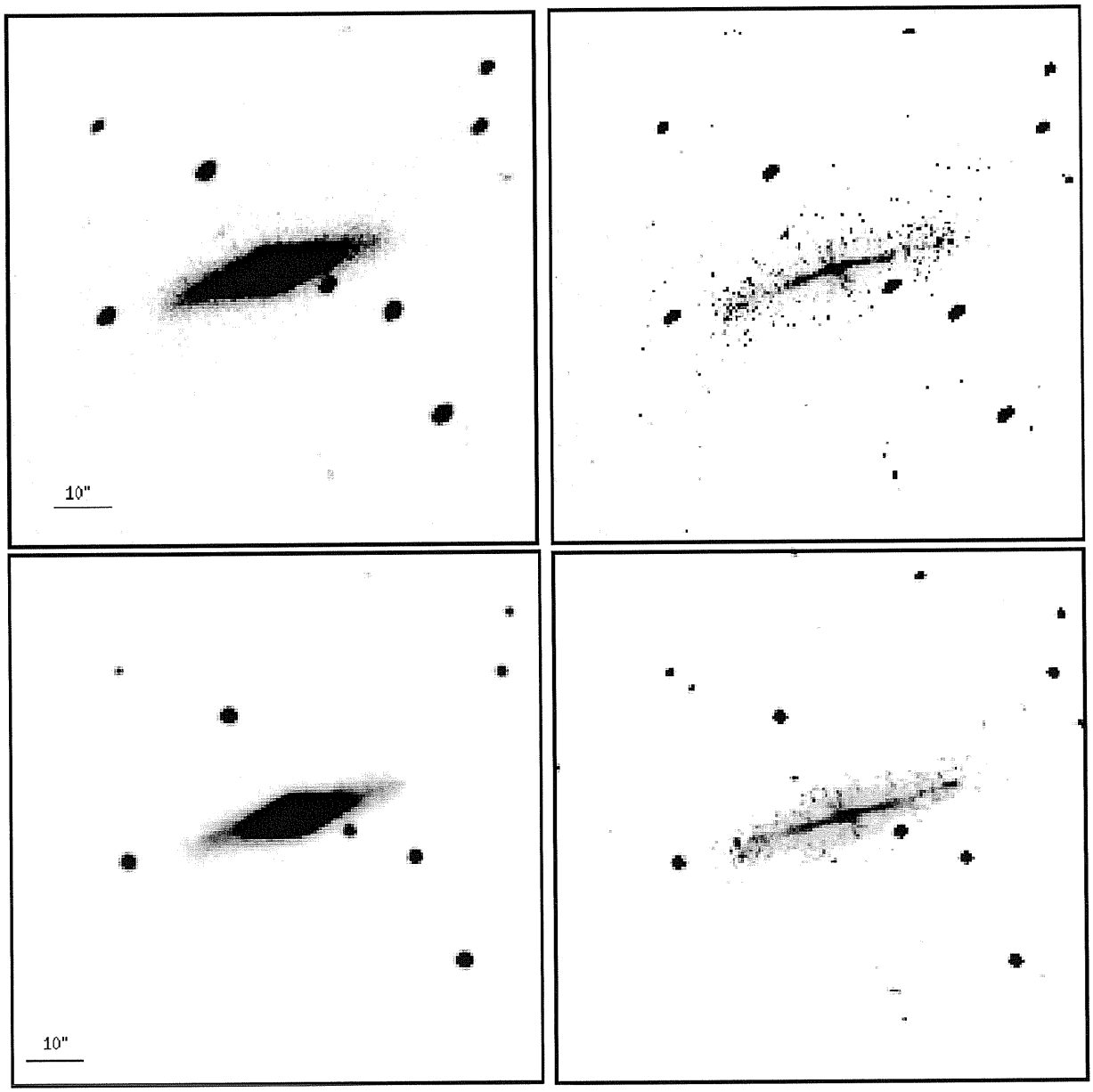

Figure B.5: **ESO235-G58**:J band (top-left panel) and Kn band image (bottom-left panel) and relative high-frequency residual images (top-right panel, in J band) and (bottom-right panel, in Kn band).

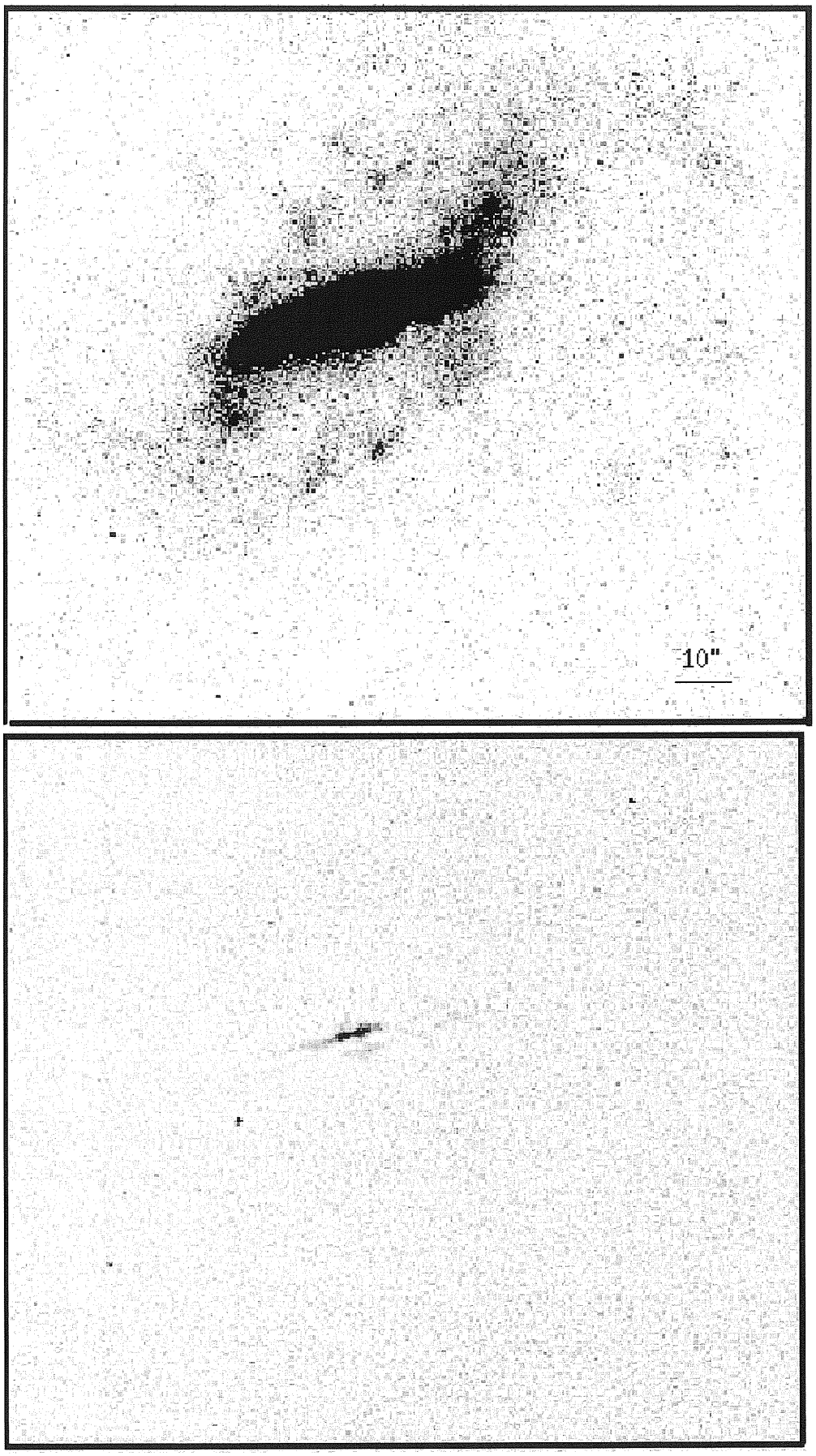

Figure B.6: **ESO235-G58**: V band (top panel) and and relative high-frequency residual images (bottom panel).

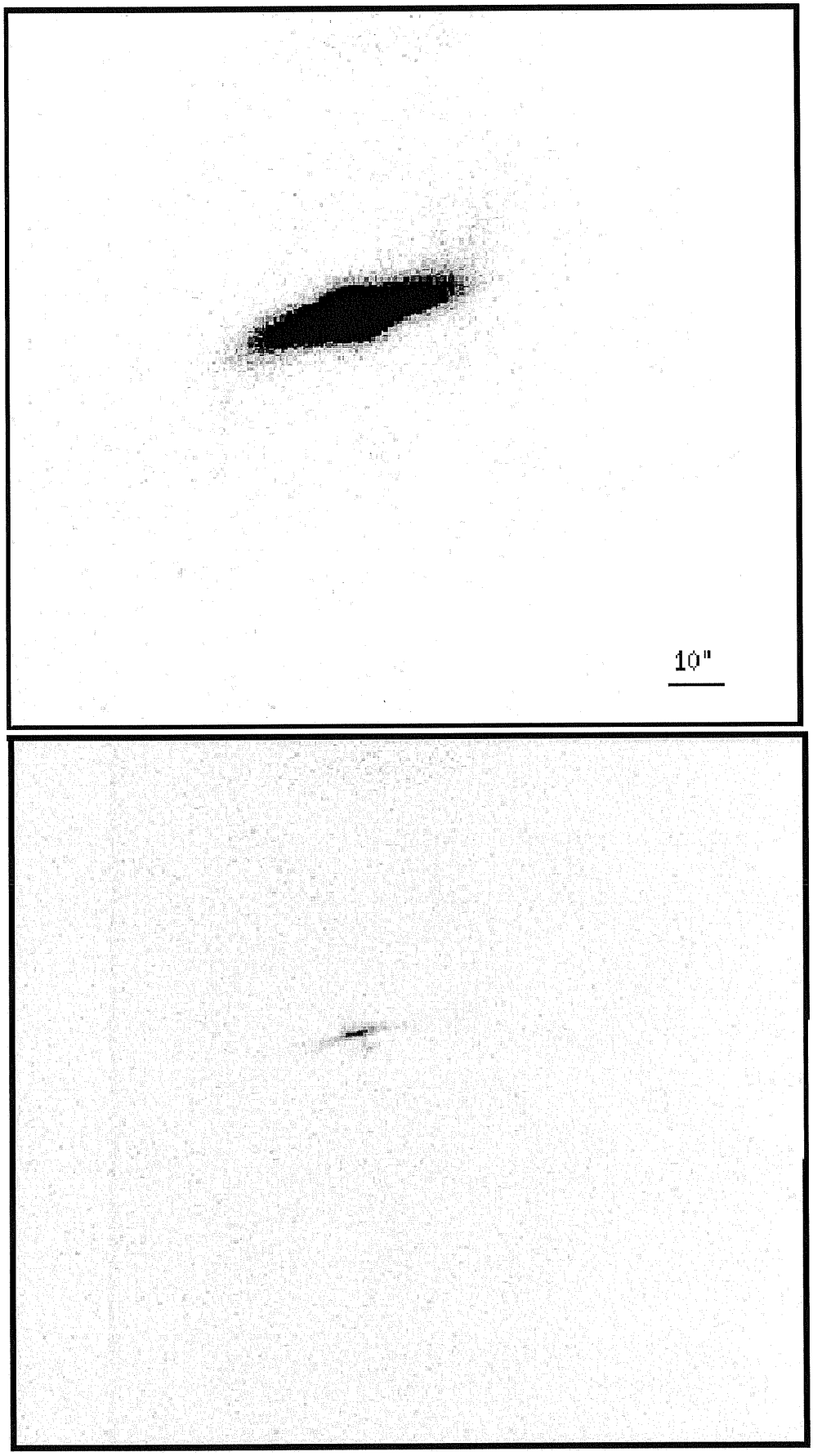

Figure B.7: **ESO235-G58**: I band (top panel) and and relative high-frequency residual images (bottom panel).

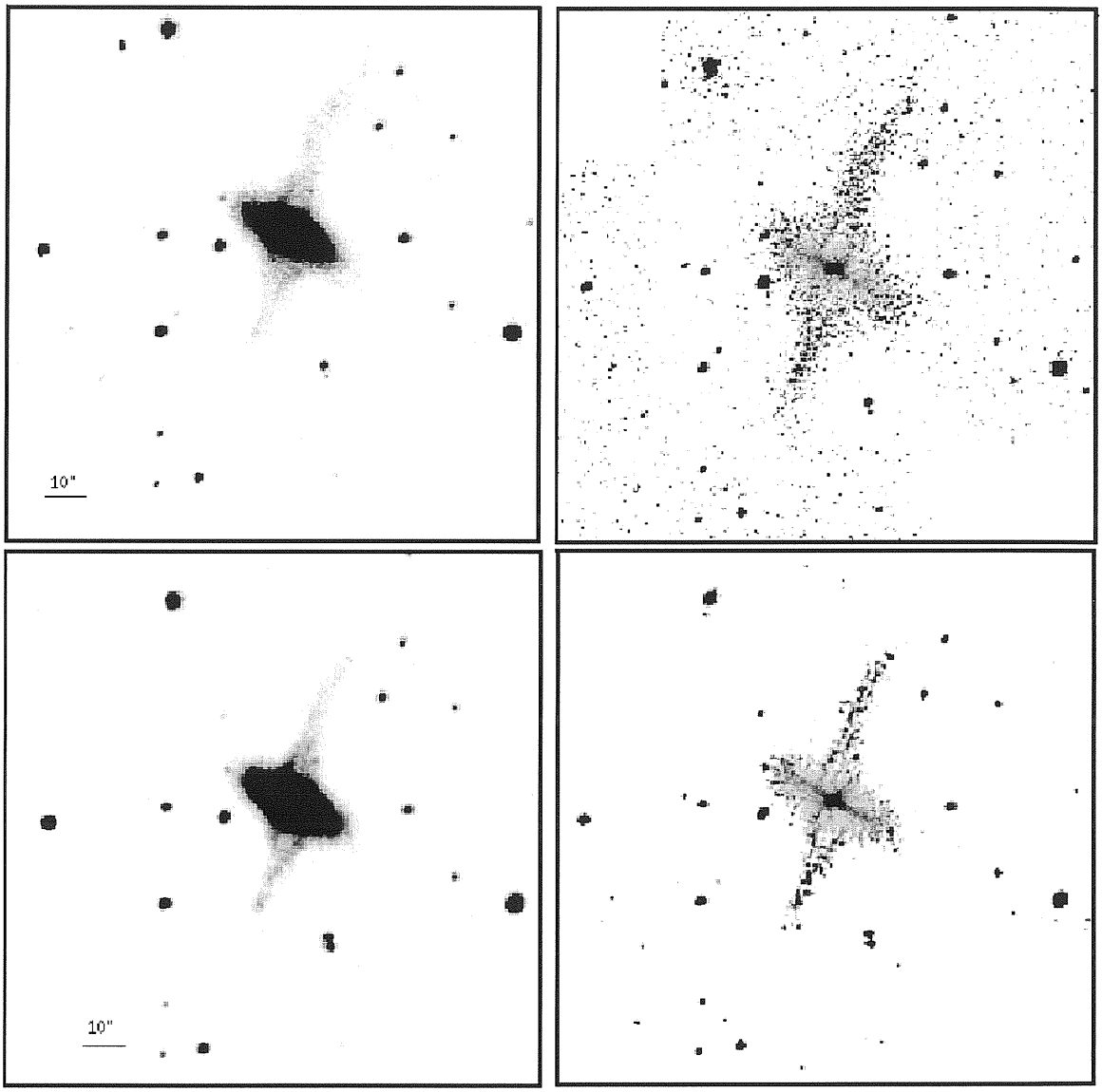

Figure B.8: **NGC4650A**:J band (top-left panel) and Kn band image (bottom-left panel) and relative high-frequency residual images (top-right panel, in J band) and (bottom-right panel, in Kn band).

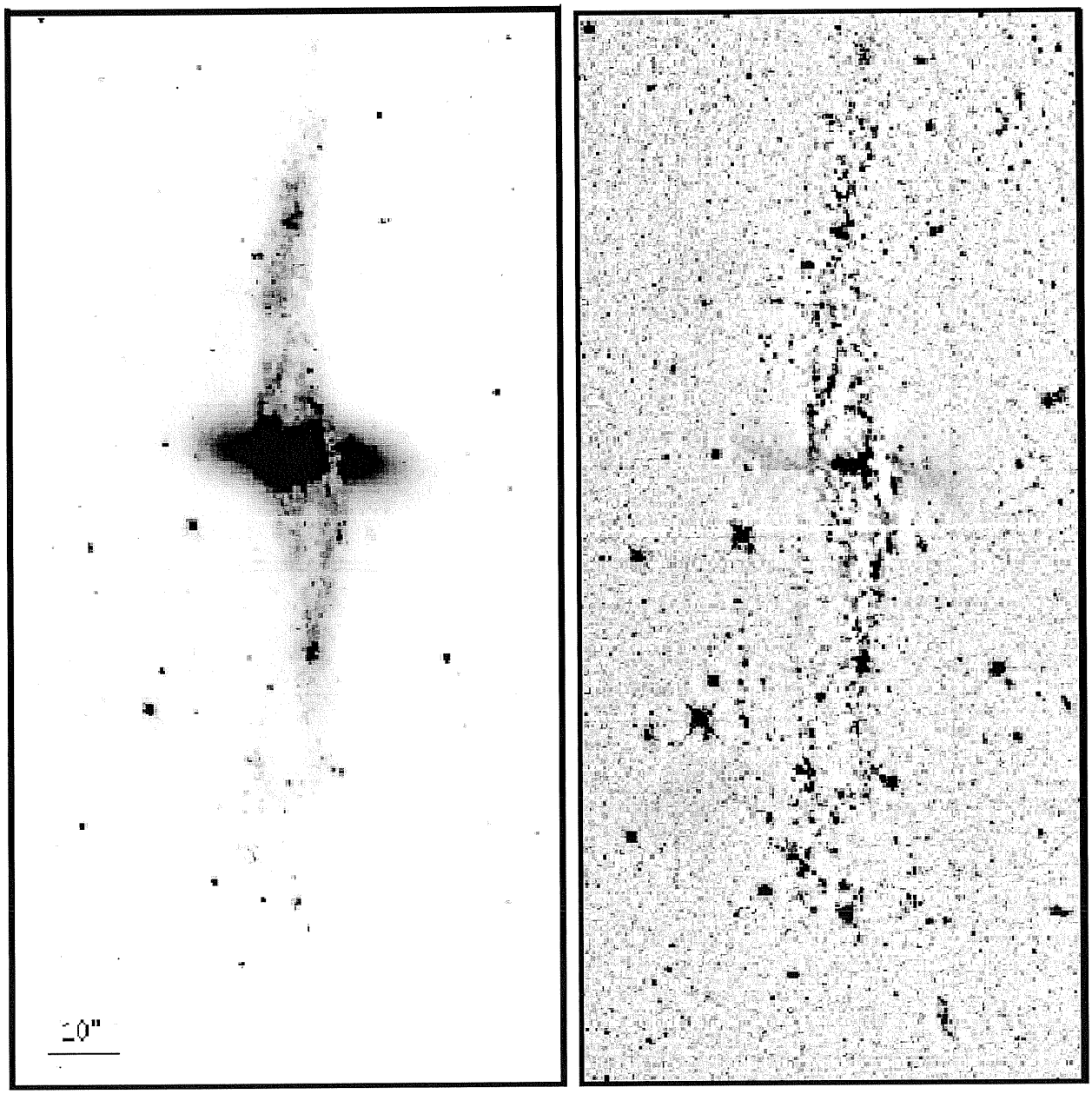

Figure B.9: **NGC4650A**: HST B band (left panel) and and relative high-frequency residual images (right panel). North is 20° counter clockwise from the y axis, East is 110° counter clockwise from the same axis, on the left side of the image.

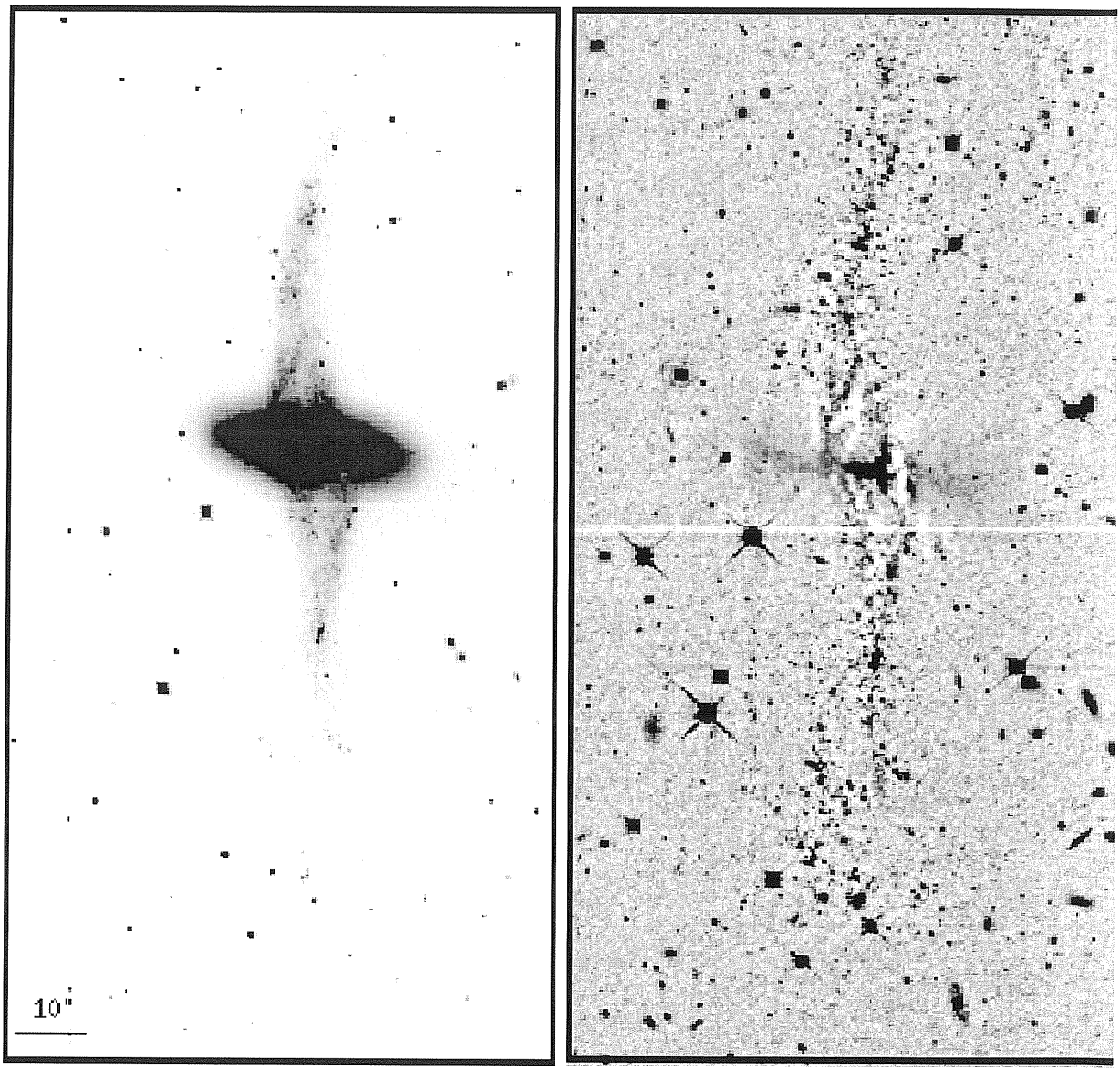

Figure B.10: **NGC4650A**: HST I band (left panel) and and relative high-frequency residual images (right panel). North is 20° counter clockwise from the y axis, East is 110° counter clockwise from the same axis, on the left side of the image.

Bibliography

[Aaronson et al. 1978] Aaronson, M. , Cohen, J. , Mould, J. and Malkan, M. 1978, Astron. J., 223, 824

[Arnaboldi et al. 1993a] Arnaboldi, M. , Capaccioli, M. , Barbaro, G. , Buson, L. , and Longo, G. , 1993, Astron. Astrophys., 268, 103

[Arnaboldi et al. 1993b] Arnaboldi, M. , Capaccioli, M., Barbaro, G., Buson, L., Longo, G., 1993, Astron. Astrophys., 268, 103

[Arnaboldi et al. 1995] Arnaboldi, M. , Freeman, K. C., Sackett, P. D., Sparke, L. S. and Capaccioli, M., 1995, Publ. Astron. Soc. of the Pacific, 43, 1377

[Arnaboldi & Sparke 1994] Arnaboldi, M. and Sparke, L. S. 1994, Astron. J., 107, 958

[Arnaboldi et al. 1997] Arnaboldi, M. , Oosterloo, T. , Combes, F. , Freeman, K. C. and Koribalski, B. 1997, Astron. J., 113, 585

[Athanassoula et al. 1990] Athanassoula, E., Morin, S., Wozniak, H., Puy, D., Pierce, M. J., Lombard, J. and Bosma, A. 1990, Mon. Not. R. astr. Soc., 245, 130

[Bahcall & Soneira 1980] Bahcall, J. N. and Soneira, R. M., 1980, Astrophys. J. Supp., 44, 73

[Barnes & Hernquist 1992] Barnes, J.E. and Hernquist, L., 1992, Ann. Rev. Astr. Ap., 30, 705

[Barnes & Hernquist 1996] Barnes, J. and Hernquist, L., 1996, Astrophys. J., 471, 115

[Bekki 1998a] Bekki, K., 1998, Astrophys. J., 502, 133

[Bekki 1998] Bekki, K. 1998, Astrophys. J., 499, 635

[Bekki & Shioya 1997a] Bekki, K. and Shioya, Y., 1997 Astrophys. J. Letters, 478, L17

[Bekki & Shioya 1997b] Bekki, K. and Shioya, Y., 1997 Astrophys. J., 479, 108

[Bell et al. 2000] Bell, E. F. , Banaby, D. , Bower, R. G. , de Jong, R. S. , Harper, D. A. , Hereld, M. , Loewenstein, R. F. and Rauscher, B. J. 2000, Mon. Not. R. astr. Soc., 312, 470

[Bergvall et al. 1999] Bergvall, N. , Ronnback, J. , Masegosa, J. and Ostlin, G. 1999, Astron. Astrophys., 341, 697

[Bertola et al. 1991] Bertola, F., Bettoni, D., Danziger, J., Sadler, E., Sparke, L. and de Zeeuw, T. 1991, Astrophys. J., 373, 369

[Bingelli et al. 1987] Bingelli, B., Tammann, G. A. and Sandage, A. 1987, Astron. J., 94, 251

[Binney & Tremaine 1987] Binney J. and Tremaine S. 1987, *Galactic dynamics*, Princeton, NJ, Princeton University Press

[Bosma 1981] Bosma, A., 1981, Astron. J., 86, 1825

[Bothun 1982] Bothun, G. D. 1982, Astrophys. J. Supp., 50, 39

[Bothun et al. 1984] Bothun, G. D., Romanishin, W., Strom, S. E. and Strom, K. M. 1984, Astron. J., 89, 1300

[Bothun and Gregg 1990] Bothun, G. D. and Gregg, M. D. 1990, Astrophys. J., 350, 73

[Bruzual & Charlot 1993] Bruzual, G. and Charlot, S. 1993, Astrophys. J., 405, 538

[Buta 1991] Buta, R., 1991, Proceedings of the 146th Symposium of the International Astronomical Union, Edited by F. Combes and Fabienne Casoli. International Astronomical Union. Symposium no. 146, Kluwer Academic Publishers, Dordrecht, 1991., p.251

[Buta and Crocker 1992] Buta, R. and Crocker, D. A., 1992, Astron. J., 103, 1804

[Buta and Crocker 1993] Buta, R. and Crocker, D. A., 1993, Astron. J., 106, 939

[Byun and Freeman 1995] Byun, Y. I. and Freeman, K. C. 1995, Astrophys. J., 448, 563

[Caon, Capaccioli & D'Onofrio 1993] Caon, N., Capaccioli, M. and Capaccioli, M. 1993, Mon. Not. R. astr. Soc., 265, 1013

[Capaccioli et al. 1992] Capaccioli, M., Caon, N. and D'Onofrio, M., 1992, Mon. Not. R. astr. Soc., 259, 323

[Cardelli et al. 1989] Cardelli, J.A., Clayton, G.C. and Mathis, J.S., 1989, Astrophys. J., 345, 245

[Carignan 1999] Carignan, C. 1999, Publication of the Astronomical Society of Australia, 16, 18

[Carter & Meadows 1995] Carter, B. S. and Meadows, V. S. 1995, Mon. Not. R. astr. Soc., 276, 734

[Charlot, Worthey and Bressan 1996] Charlot, S. , Worthey, G. and Bressan, A. 1996, Astrophys. J., 457, 625

[Christodoulou, Katz, Rix and Habe 1992] Christodoulou, D. M., Katz, N., Rix, H. and Habe, A. 1992, Astrophys. J., 395, 113

[Cole et al. 1994] Cole, S., Aragon-Salamanca, A., Frenk, C. S., Navarro, J. F. and Zepf, S. E., 1994, Mon. Not. R. astr. Soc., 271, 781

[Combes and Arnaboldi 1996] Combes, F. and Arnaboldi, M. 1996, Astron. Astrophys., 305, 763

[Cox (1996)] PhD Thesis, Univ. of Wisconsin, Madison, USA

[Dalcanton et al. 1997] Dalcanton, J.J., Spergel, D.N. and Summers, F. J., 1997, Astrophys. J., 482, 659

[Davies et al. 1988] Davies, J. I., Phillipps, S., Cawson, M. G. M., Disney, M. J. and Kibblewhite, E. J., 1988, Mon. Not. R. astr. Soc., 232, 239

[de Block & McGaugh 1997] de Blok, W. J. G. and McGaugh, S. S., 1997, Mon. Not. R. astr. Soc., 290, 533

[de Jong and van der Kruit 1994] de Jong, R. S. and van der Kruit, P. C. 1994, Astron. Astrophys. Suppl. Ser., 106, 451

[de Jong 1996] de Jong, R. S. 1996, Astron. Astrophys. Suppl. Ser., 118, 557

[de Vaucouleurs 1948] de Vaucouleurs, G., 1948, Annales d'Astrophysique, Vol. 11, p. 247

[Driver et al. 1995] Windhorst R.A., Ostrander E.J., Keel W.C., Griffiths R.E. and Ratnatunga K.U., 1995, Astrophys. J. Letters, 449, L23

[Elizondo et al. 1999] Elizondo, D.; Yepes, G.; Kates, R.; Muller, V.; Klypin, A., 1999, Astrophys. J., 515, 525

[Erwin and Sparke 1999] Erwin P. and Sparke L. S. Astrophys. J. Letters, 521, L37

[Firmani & Avila-Rees 1998a] preprint astro-ph/9803090

[Firmani & Avila-Rees 1998b] preprint astro-ph/9810293

[Freeman 1970] Freeman, K. C. 1970, Astrophys. J., 160, 767

[Frogel et al. 1983] Frogel, J., Cohen, J. and Persson, E. 1983, Astron. J., 275, 773

[Frogel 1985] Frogel, J. 1985, Astrophys. J., 298, 528

[Gallagher et al. 2001] Gallagher, J.S., Sparke, L.S., Matthews, L.D., Frattare, L.M., English, J., Kinney, A.L., Iodice, E., Arnaboldi, M. 2001, Astrophys. J., in press.

[Gallagher, Hunter & Tutukov 1984] Gallagher, J.S., Hunter, D. A. and Tutukov, A. V., 1984, Astrophys. J., 284, 544

[Galletta, Sage & Sparke 1997] Galletta, G., Sage, L. J. and Sparke, L. S., 1997, Mon. Not. R. astr. Soc., 284, 773

[Giovanardi & Hunt 1996] Giovanardi, C. and Hunt, L. K. 1996, Astron. J., 111, 1086

[Glass & Moorwood 1985] Glass, I. S. and Moorwood, A.F.M., 1985, Mon. Not. R. astr. Soc., 214, 429

[Gordon, Calzetti & Witt 1997] Gordon, K. D. , Calzetti, D. and Witt, A. N. 1997, Astrophys. J., 487, 625

[Graham 1982] Graham, J. A., 1982, Publ. Astron. Soc. of the Pacific, 94, 244

[Heavens & Jiminez 1999] Heavens, A. F. and Jimenez, R., 1999, Mon. Not. R. astr. Soc., 305, 770

[Heisler, Merritt & Schwarzschild 1982]
Heisler, J. Merritt, D. and Schwarzschild, M. 1982, Astrophys. J., 258, 490

[Hernquist & Weil 1993] Hernquist, L. and Weil, M. L. 1993, Mon. Not. R. astr. Soc., 261, 804

[Hernquist & Quinn 1988] Hernquist, L. and Quinn, P.J., 1988, Astrophys. J., 331, 682

[Hibbard & Yun 1999] Hibbard, J. E. and Yun, Min. S., 1999, Astrophys. J., 522, L93

[Holtzman et al. 1995] Holtzman, J. A. , Burrows, C. J. , Casertano, S. , Hester, J. J. , Trauger, J. T. , Watson, A. M. , and Worthey, G. 1995, Publ. Astron. Soc. of the Pacific, 107, 1065

[Iodice et al. 2001] Iodice, E. , D'Onofrio, M. and Capaccioli, M. 2001, Astrophysics and Space Science, 276, Issue 2/4, 869

[Iodice et al. 2001] Iodice, E., Arnaboldi M., De Lucia, G., Gallagher, J.S., Sparke, L.S. and Freeman, K.C. 2001, Astron. J., in press (astro-ph/0110249).

[Kauffmann, White and Guiderdoni 1993] Kauffmann, G.; White, S. D. M.; Guiderdoni, B., 1993, Mon. Not. R. astr. Soc., 264, 201

[Katz and Rix 1992] Katz, N. and Rix, H. 1992, Astrophys. J. Letters, 389, L55

[Kennicutt 1983] Kennicutt, R. C., Jr., 1983, Astrophys. J., 272, 54

[Kent 1985] Kent, S., 1985, Astrophys. J. Supp., 59, 115

[Kormendy 1979] Kormendy, J., 1979, Astron. J., 227, 714

[Laustsen & West 1980] Lausten, S. and West, R. M., 1980, J. Astrophys. Astron., 1, 177-187

[Li & Seaquist 1994] Li, J.G. and Seaquist, E. R., 1994, Astron. J., 107, 1953

[Lutz 1991] Lutz D., 1991, Astron. Astrophys., 245, 31

[Maia et al. 1989] Maia, M.A.G., da Costa, L.N. and Latham, D.W., 1989, Astrophys. J. Supp., 69, 809

[Makarova 1999] Makarova, L. 1999, Astron. Astrophys. Suppl. Ser., 139, 491

[Matthews & Gallagher 1997] Matthews, L.D. and Gallagher, J.S., 1997, Astron. J., 114, 1899

[Matthews, Gallagher and van Driel 1999] Matthews, L. D. , Gallagher, J. S. and van Driel, W. 1999, Astron. J., 118, 2751

[McGaugh & de Blok 1998] McGaugh, Stacy S.; de Blok, W. J. G., 1998, Astrophys. J., 499, 66

[McGaugh et al. 2000] McGaugh, S. S.; Schombert, J. M.; Bothun, G. D.; de Blok, W. J. G., 2000, Astrophys. J., 533, 99

[McGregor 1994] McGregor, P. J. 1994, Publ. Astron. Soc. of the Pacific, 106, 508

[Michard & Poulain 2000] Michard, R. and Poulain, P. 2000, Astron. Astrophys. Suppl. Ser., 137, 245

[Mihos et al. 1995] Mihos, J.C., Walker, I.R., Hernquist, L., Mendes de Oliveira, C. and Bolte, M., 1995, Astrophys. J. Letters, 447, L87

[Mo et al. 1998] Mo, H. J.; Mao, Shude; White, Simon D. M., 1998, Mon. Not. R. astr. Soc., 295, 319

[Mollenhoff et al. 1992] Moellenhoff, C., Hummel, E. and Bender, R. 1992, Astron. Astrophys., 255, 35

[Moshir et al. 1990] Moshir, M., Kopan, G., Conrow, T., McCallon, H., Hacking, P., Gregorich, D., Rohrbach, G., Melnyk, M., Rice, W., Fullmer, L., White, J. and Chester, T. 1990, Bulletin of the American Astronomical Society, Vol. 22, p. 1325

[Mould et al. 1982] Mould, J., Balick, B., Bothun, G. and Aaronson, M. 1982, Astrophys. J., 260, L37

[Navarro, Frenk and White 1996] Navarro, J. F.; Frenk, C.S. and White, S.D. M., 1996, Astrophys. J., 462, 563;

[Navarro, Frenk and White 1997] Navarro, J. F.; Frenk, C.S. and White, S.D. M., 1996, Astrophys. J., 490, 493;

[Nieto, Capaccioli and Held 1988] Nieto, J.-L.; Capaccioli, M.; Held, E. V., 1988, Astron. Astrophys., 195, 1

[O'Neil et al. 1997] O'Neil, K., Bothun, G. D. , Schombert, J. , Cornell, M. E. and Impey, C. D. 1997, Astron. J., 114, 2448

[Persic & Salucci 1991] Persic M. and Salucci P. 1991, Mon. Not. R. astr. Soc., 248, 325

[Persson et al. 1979] Persson, S. E. , Frogel, J. A. and Aaronson, M. 1979, Astrophys. J. Supp., 39, 61

[Quinn 1984] Quinn, T. 1984, Astrophys. J., 279, 596

[Quinn 1991] Quinn, T. 1991, in Warped Disks and Inclined Rings around Galaxies, ed. S. Casertano, P. Sackett and F. Briggs (New York: Cambridge Univ. Press), 143

[Reshetnikov et al. 1994] Reshetnikov, V. P., Hagen-Thorn, V. A. and Yakovleva, V. A., 1994, Astron. Astrophys., 290, 693

[Reshetnikov et al. 1996] Reshetnikov, V. P., Hagen-Thorn, V. A. and Yakovleva, V. A., 1996, Astron. Astrophys., 314, 729

[Reshetnikov and Sotnikova 1997] Reshetnikov, V. and Sotnikova, N. 1997, Astron. Astrophys., 325, 933

[Reshetnikov 1997] Reshetnikov, V.P. 1997, Astron. Astrophys., 321, 749

[Richter, Sackett & Sparke 1994] Richter, O.-G., Sackett, P. D., Sparke, L. S., 1994, Astron. J., 107, 99

[Roberts & Haynes 1994] Roberts, M. S. and Haynes, M., 1994, Proceedings of an ESO/OHP Workshop on Dwarf galaxies, dited by Georges Meylan and Phillippe Prugniel., p.197

[Sackett, Rix, Jarvis and Freeman 1994] Sackett, P. D., Rix, H., Jarvis, B. J. and Freeman, K. C. 1994, Astrophys. J., 436, 629

[Sackett and Sparke 1990] Sackett, P. D. and Sparke, L. S. 1990, Astrophys. J., 361, 408

[Sackett 1991] Sackett. P., 1991, in Warped Disks and Inclined Rings around Galaxies, ed. S. Casertano, P. Sackett and F. Briggs (New York: Cambridge Univ. Press), p.73

[Salpeter (1955)] Salpeter, E. E. 1955, Astrophys. J., 121, 161

[Schechter et al. 1984a] Schechter, P. L., Sancisi, R., van Woerden, H. and Lynds, C. R., 1984, Mon. Not. R. astr. Soc., 208, 111

[Schechter et al. 1984b] Schechter, P. L., Boksenberg, A.and Ulrich, M.-H., 1984, Astrophys. J., 277, 526

[Schiminovich et al. 1997] Schiminovich, D., van Gorkom, J., van der Hulst, T., Oosterloo, T. and Wilkinson, A. 1997, in *The Nature of Elliptical Galaxies*, 2nd Stromlo Symposium. ASP Conference Series, Vol. 116, p.362, ed. M. Arnaboldi, G. S. Da Costa and P. Saha

[Schlegel et al. 1998] Schlegel, D. J., Finkbeiner, D. P. and Davis, M. 1998, Astrophys. J., 500, 525

[Schombert & Bothun 1987] Schombert, J.M.and Bothun, G.D., 1987, Astron. J., 93, 60

[Schwarz 1981] Schwarz M.P., 1981, Astrophys. J., 247, 77

[Schweizer, Whitmore and Rubin 1983] Schweizer, F., Whitmore, B. C. and Rubin, V. C., 1983, Astron. J., 88, 909

[Schweizer 1999] Schweizer F., 1999, Proceedings of IAU Symposium n.186, edited by J. E. Barnes, and D. B. Sanders, 1999., p.1

[Sersic 1968] Sersic, J. L., 1968, in Atlas de Galaxes Australes

[Sèrsic & Agüero 1972] Sèrsic, J.L. and Agüero, E.L., 1972, Astrophysics and Space Science, 19, 387

[Shane 1980] Shane, W.W., 1980, Astron. Astrophys., 82, 314

[Silk 1997] Silk, J., 1997, Astrophys. J., 481, 703

[Sparke 1986] Sparke, L.S. 1986, Mon. Not. R. astr. Soc., 219, 657

[Sparke 1991] Sparke, L.S., 1991 in Warped Disks and Inclined Rings around Galaxies, ed. S. Casertano, P. Sackett and F. Briggs (New York: Cambridge Univ. Press), p.85

[Sparke and Cox 2000] Sparke, L. S. and Cox, A. L., 2000 in Dynamics of Galaxies: from the Early Universe to the Present, Eds. Francoise Combes, Gary A. Mamon, and Vassilis Charmandaris, ASP Conference Series, Vol. 197, p. 119.

[Steiman-Cameron & Durisen 1982] Steiman-Cameron, T. Y. and Durisen, R. H., 1982, Astrophys. J., 263, 51

[Steiman-Cameron 1991] Steiman-Cameron, T., 1991 in Warped Disks and Inclined Rings around Galaxies, ed. S. Casertano, P. Sackett and F. Briggs (New York: Cambridge Univ. Press), p.131

[Steimnetz & Navarro 1999] Steinmetz, M. and Navarro, J.F., 1999, Astrophys. J., 513, 555

[Thuan 1985] Thuan, T. X. 1985, Astrophys. J., 299, 881

[Toomre & Toomre 1972] Toomre, A. and Toomre, J., 1972, Astrophys. J., 178, 623

[Toomre 1977] Toomre, A., 1977, Ann. Rev. Astr. Ap., 15, 437

[Tully and Fisher 1977] Tully, R. B.; Fisher, J. R., 1977, Astron. Astrophys., 54, 661

[van de Bosch 2000] van de Bosch, F.C., 2000, Astrophys. J., 530, 177

[van Driel et al. 1995] van Driel, W., Combes, F., Casoli, F., Gerin, M., Nakai, N., Miyaji, T., Hamabe, M., Sofue, Y., Ichikawa, T., Yoshida, S., Kobayashi, Y., Geng, F., Minezaki, T., Arimoto, N., Kodama, T., Goudfrooij, P., Mulder, P. S., Wakamatsu, K. and Yanagisawa, K. 1995, Astron. J., 109, 942

[van Driel et al. 2000] van Driel, W., Arnaboldi, M., Combes, F. and Sparke, L. S., 2000, Astron. Astrophys. Suppl. Ser., 141, 385

[van Gorkom et al. 1987] van Gorkom, J. H., Schechter, P.L. and Kristian, J., 1987, Astrophys. J., 314, 457

[van Gorkom & Schiminovich 1997] van Gorkom, J. and Schiminovich, D. in *The Nature of Elliptical Galaxies*, 2nd Stromlo Symposium. ASP Conference Series, Vol. 116 p.310, ed. M. Arnaboldi, G. S. Da Costa and P. Saha

[Verheijen 1997] Verheijen, M. A. W., 1997, Astrophysics and Space Science, 269, 671

[Verheijen 2001] Verheijen, M. A. W., Sancisi, R., 2001, Astron. Astrophys., 370, 765

[Whitmore 1991] Whitmore, B. C. 1991, in Warped Disks and Inclined Rings around Galaxies, ed. S. Casertano, P. Sackett and F. Briggs (New York: Cambridge Univ. Press), 60

[Whitmore et al. 1990] Whitmore, B. C., Lucas, R. A. , McElroy, D. B. , Steiman-Cameron, T. Y. , Sackett, P. D. and Olling, R. P. 1990, Astron. J., 100, 1489

[Whitmore, McElroy and Schweizer 1987] Whitmore, B. C., McElroy, D. B. and Schweizer, F. 1987, Astrophys. J., 314, 439

[Williams et al. 1995] Williams, R., Dickinson, M., Giavalisco, M., Gilliland, R., Ferguson, H., Fruchter, A., McElroy, D., Lucas, R., Petro, L., Postman, M., American Astronomical Society Meeting, 187

[Wilkinson et al. 1987] Wilkinson, A., Browne, I.W.A. and Wolstencroft, R.D. 1987, Mon. Not. R. astr. Soc., 228, 933